Development of a finite element model of the knee using patient specific magnetic resonance imaging data and biomechanical testing of soft tissues

Joanna Yuen Sai Li MEng ACGI

School of Engineering
Cardiff University

A thesis submitted for the degree of
Doctor of Philosophy
2013

Declaration

This work has not been previously accepted in substance for any degree and is not currently in candidature from any degree.

Signed……(candidate) Date……

Statement 1

This thesis is being submitted in partial fulfillment of the requirements for the degree of Doctor of Philosophy.

Signed……(candidate) Date……

Statement 2

This thesis is the result of my own independent work/ investigation, except where otherwise stated. Other sources are acknowledged by explicit references.

Signed……(candidate) Date……

Statement 3

I hereby give consent for my thesis, if accepted, to be available for photocopying and for library loan, and for the title and summary to be made available outside organizations.

Signed……(candidate) Date……

Dedications

To my parents, my beacons of light, George and Shirley, who studied Clinical Biochemistry and Computer Science at the University of Manchester Institute of Science and Technology.

To my wonderful sister, Jennifer, who has always been there for me, believed in me and one I can trust will put a smile on my face without fail, even on the gloomiest days.

To my younger brother, Jonathan, who has kept me company in Cardiff during his school holidays and often sporadically surprises me with some very wise words.

To my fiancé, Phil, who moved half way round the world to be 'closer to me' during my PhD, yet was still one hundred and eighty miles away, for all his endless encouragement, loving support and understanding.

And last but not least, to a very special person, my late Uncle Ernest Low. A fellow engineer who has been my inspiration to do better from the very first moment I decided to be one.

Acknowledgement

Firstly, I would like to thank my supervisory team, Prof. Sam Evans, Dr. Cathy Holt and Dr. Emma Blain for being such tremendous advisors and mentors throughout my doctoral program. I would also like to express my gratefulness to the Connective Tissue Laboratory for all their help and patience in teaching me biological skills and techniques.

I would like to acknowledge the wonderful support I had from our collaborators Simpleware Ltd. who was always helpful and their commitment to 'making things possible' for their customers was simply admirable. I would like to thank Peter Hobden, Daniel Watling and all the undergraduates, for the beautiful MR images of the knee, which I know from personal experience involved many long hours spent in the Cardiff University Brain Research Imaging Centre (CUBRIC). I would also like to acknowledge the undergraduates who worked with me on their projects in constitutive models of meniscus and segmentation of knee ligaments. Furthermore, I would like to thank the engineering IT staff for all their assistance with my computers and software, the Advanced Research Computing at Cardiff (ARCCA) team for their assistance with using the Linux clusters and the Cardiff University Structural Performance (CUSP) laboratory staff for the Digital Image Correlation (DIC) equipment.

I would like to take this opportunity to say a special thank you to all my colleagues from the Arthritis Research UK Biomechanics and Bioengineering Centre (ARUKBBC) and the Institute of Medical Engineering and Medical Physics (IMEMP) for making me feel so welcomed and at home right from the start. I started my PhD at Cardiff having only ever spent two hours in the city in a room interviewing for the position. Without them, the transition to a new university in a new city would not have been so easy. Last but not least, a large proportion of my time was spent in the office and I am glad that I got to share it with a group of enthusiastic like-minded people; Wayne Ayre, Daniel Watling, Dr. Rachel Groves, Dr. Lindsay Stroud, Dr. June Madate and Dr. Gemma Whatling. Not only did they make every minute in the office

enjoyable, they were always ready to help with proof reading, lend a hand with heavy equipment and are great minds to share and discuss ideas with.

Many say ‘doing a PhD can be very lonely’ but mine was far from that and was in fact full of wonderful researchers from around the world, who fervently shared their work, knowledge, skills and passion with me. I would like to thank Ken Short from Dassault Systemes who gave me an amazing three months experience at their headquarters in Rhode Island, USA. The wonderful life science team I worked with, Subham Sett, Cheryl Liu, Jiang Yao, Prabhav Saraswat, Viswanath (Vissu) Chinthapenta, Manoj Chinnakonda and Juan Hurtado. Also, a great thank you to Dr. YongTao Lu who introduced me to the Marie Curie Initial Training Network SpineFX and all those in the network for their warm friendship with a special mention for Dr. Hadi Seyed Hosseini.

A big thank you is also owed to those from outside academia for their encouraging words and continuous support. Sent to me from a great friend were these heartfelt words,

"Opportunity to find deeper powers within ourselves comes when life seems most challenging" - Joseph Campbell

Abstract

This thesis presents the findings of investigations carried out relating to the creation of full joint contact patient specific finite element models for correlation with biological studies in the study of Osteoarthritis (OA) development. To understand the relationship between altered loading and biological changes in articular cartilage (AC), a method for predicting stresses and strains experienced inside the tissues is required.

An in-vitro study was conducted to explore the possibility of correlating finite element (FE) and gene expression study results. FE models were used to predict the stresses and strains inside the AC for explants subjected to different loading conditions. The study demonstrated that the accurate representation of AC surface geometry is crucial and current flat surface axisymmetric cylinder representations used in AC explant modelling introduces significant error in the prediction of tissue mechanical behaviour. Cutting of the AC explant to achieve a flat surface can affect the biological, mechanical and tribology behaviour of the tissue. Thus, a method for creating explant specific finite element models with the use of digital image correlation (DIC) was developed and is presented, allowing for surface layer preservation in AC explants for correlated gene expression and inverse FE.

Reconstruction of tissue geometries from magnetic resonance (MR) imaging scan data of the knee was explored. It was possible to segment both hard and soft tissues from the same set of MR imaging scan data. Meshing of the geometries using a fundamentally voxel based algorithm proved to cause significant error in the segmented volume. An alternative contour based algorithm needs to be explored.

Uncertainties concerning the presence and modelling of meniscotibial ligaments (MTLs) in full joint contact FE models found in literature were addressed. An anatomy study revealed that the MTLs are found in both the medial and lateral side of the joint around the periphery of the anterior, middle and posterior portion of the menisci. With the use of cross polarised light microscopy, it was established

that MTLs consist of Type I collagen orientated in the circumferential direction around the menisci. As a result, the MTLs were modelled as an anisotropic membrane. Using the full joint contact finite element model, the influence of MTLs on knee joint kinematics was investigated. It was found that the MTLs reinforce the function of the meniscal horns and circumferential fibres in the meniscus and help constrain the meniscus. Therefore, it was concluded that the MTLs are mechanically significant in the stabilisation of knee joints and should be included in knee models for accurate prediction of knee joint behaviour.

Table of Contents

List of figures

List of Tables

Abbreviations

AC	Articular cartilage
ACL	Anterior cruciate ligament
AP	Anterior-Posterior
ARCCA	Advanced Research Computing at Cardiff
ARUKBBC	Arthritis Research UK Biomechanics and Bioengineering Centre
CF	Collagen fibre
CT	Computed tomography
CUBRIC	Cardiff University Brain Repair Imaging Centre
DIC	Digital image correlation
dMCL	Deep medial collateral ligament
DOFs	Degrees of freedom
ECM	Extracellular matrix
FCD	Fixed charge density
FE	Finite element
GAGs	Glycoaminoglycans
HBSS	Hank's balanced salt solution
HTO	High tibial osteotomy
IMEMP	Institute of Medical Engineering and Medical Physics
IML	Intermeniscal ligament
LA	Lateral anterior
LCL	Lateral collateral ligament
LP	Lateral posterior
MA	Medial anterior
MP	Medial posterior
MCL	Medial collateral ligament
MFL	Meniscofemoral ligament
ML	Medial-Lateral
MR	Magnetic resonance

MTL	Meniscotibial ligament
NURBS	Non-uniform rational B-Spline
OA	Osteoarthritis
PBS	Phosphate buffer solution
PCL	Posterior cruciate ligament
PCM	Pericellular matrix
PGs	Proteoglycans
RMSE	root mean squared error
SI	Superior-Inferior
SSE	summed squared error
sMCL	Superficial medial collateral ligament
TKR	Total knee replacement

Nomenclature

A	First constant coefficient for the equation of a plane
B	Second constant coefficient for the equation of a plane
C	Third constant coefficient for the equation of a plane
E	Young's modulus
$G_{(t)}$	Time dependent relaxation modulus
G_{∞}	Long term relaxation modulus
H_A	Aggregate modulus
N	Number of data points
P	Contact pressure
R	molar gas constant
T	absolute temperature
T_c	chemical expansion stress
RMSE	Root mean squared error
SSE	Sum of the squared errors
X_o^i	initial position of node i
c	ion concentration
c_β	constant coefficient for thermal expansion stress
e	current void ratio
e_o	initial void ratio
$\hat{e}_o$	initial void ratio at surface of cartilage
e_r	radial strain
e_z	axial strain
e_θ	hoop strain
h	intersection between two surfaces
k	spring stiffness
l_o	initial ligament length
l	deformed ligament length
m	total number of voxels selected

u^i	displacement of node i
z	depth of point in tissue
ΔT	change in temperature
Δu	relative displacement between two nodes
$\Delta \pi$	osmotic pressure gradient
α_e	void ratio coefficient
α_T	coefficient for linear thermal expansion
β	Surface flatness factor
β_o	constant coefficient for thermal expansion stress
ε_l	arbitrary parameter for nonlinear spring behavior
ζ	Arbitrary constant multiplier for the region growing equation
κ	permeability
κ_o	initial reference permeability
ν	poison's ratio
ξ	osmotic coefficient
ψ_i	Greyscale value of voxel i
ψ_{mean}	Mean greyscale value of all voxels selected
$\psi_{s.d.}$	Standard deviation of greyscale values of all voxels selected
ψ^n_{upper}	New upper bound value for greyscale range
ψ^n_{lower}	New lower bound value for greyscale range
π	internal osmotic pressure
π_{ext}	external osmotic pressure
σ_r	radial stress
σ_z	axial stress
σ_θ	hoop stress
τ_i	relaxation time constant

Chapter 1 Introduction

In the UK, 6 million people have been reported to suffer osteoarthritic pain in their knees[1]. It is estimated that osteoarthritis (OA) affects the daily activities of over a third of the population aged over fifty years[2] and is at present the most common cause for claiming Disability Living Allowance[3]. OA can cause a phenomenal negative impact on the economy[4], as well as financial burden for the patients[5]. In the UK, an estimated £5.8 billion is forgone annually due to lost workdays, benefit claims and social services associated with OA[6]. In addition, it is reported to cost the NHS £700 million per year in treating OA patients where over half of the money is spent on hip and knee replacements[7].

During mechanical loading of the knee joint, loads are applied to the connective tissue, Articular cartilage (AC), found between the articulating bones. On a microscopic level, the loads applied to the bulk AC tissue are carried by the extracellular matrix (ECM) and interstitial fluid. Found embedded in the ECM are regulatory cells, which regulate the metabolic activities of the tissues in response to internal and external stimuli, called chondrocytes. Via the ECM and pericellular matrix, mechanical stimuli are transmitted to the chondrocyte cells. Sequentially, the mechanical stimuli trigger a series of cell signalling events that induces various biological responses in the tissue. This mechanobiological process allows AC to continually adapt to changing mechanical demands and regulate matrix turnover. Optimum tissue health is achieved by maintaining a delicate balance between catabolic and anabolic processes. In cases of OA, abnormal loading is believed to be a primary risk factor in initiating altered tissue metabolism and composition resulting in degeneration of AC.

Total knee replacements (TKR)s are widely accepted globally as one of the most effective interventions for OA. However, high tibial osteotomy (HTO) is increasingly being recognised as a good alternative surgical procedure for younger, more active patients who suffer from early stage uni-compartmental OA[8]. Without the need for tissue replacement, this comparatively more conservative treatment promotes tissue longevity, allows better post-operative recovery and mobility and helps postpone the need for a TKR.

Mal-alignment of the knee can be classified as either varus or valgus, and can be corrected using both a closing wedge and an opening wedge osteotomy. The surgical procedure introduces a wedge in the tibia just below the tibial plateau to correct the tibiofemoral alignment. The aim is to remove any abnormal loading on the affected side and improve load distribution across the knee joint.

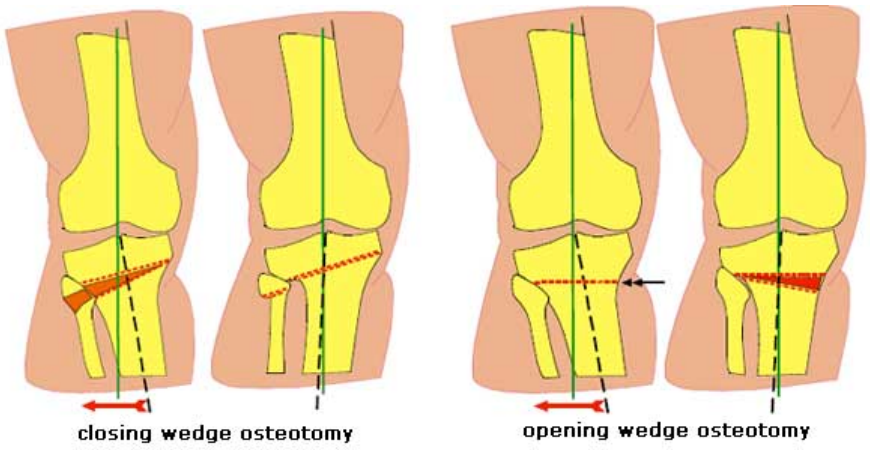

Figure 1.1 Re-alignment of a varus knee using a closing wedge (left) and an opening wedge (right) high tibial osteotomy.[9]

Surgeons in Japan have performed HTO in older patients with severe OA. A ten to twenty years HTO follow up study on 94 patients with an average age of 63 demonstrated only 9.6% of the patients required a TKR surgery eventually, which is classified as HTO surgery failure[10]. However, in other worldwide studies, success

rates ranged between 39% and 67%[11 12]. The question is then, which and what combination of contributing factors determines the failure or success of a HTO?

Similar to the onset of OA, the success of HTO intervention is a complex multi-factorial problem and requires careful examination of both patient specific mechanical and mechano-biological contributing factors. These include mechanical considerations, such as the altered axis alignment, contact areas, load distribution across the joint, gait pattern[13], and biological considerations associated with the altered mechanical factors, such as whether the new stresses experienced in the tissues promote turnover of the cartilage matrix to prevent further degeneration of the tissue[14].

It is therefore, believed that the altered mechanical loading patterns due to surgical intervention introduce changes in the biology of the tissue. And by understanding the relationship between altered loading and biological changes in the AC of HTO patients, it will correspondingly provide a better insight into the relationship between altered loading and cartilage degeneration in OA patients.

The Arthritis Research UK Biomechanics and Bioengineering Centre (ARUKBBC) combines interdisciplinary research across six academic schools at Cardiff University, including the Schools of Bioscience, Dentistry, Engineering, Healthcare Studies, Medicine and Pharmacy; and four research institutes, including the Cardiff Institute of Tissue Engineering Research, Cardiff University Brain Research Centre, Experimental MRI Centre and Wales Research & Diagnostic Positron & Emission Tomography Imaging Centre. Co-supervised by the School of Engineering and Bioscience, this PhD research was run in parallel with other projects to address one of the many centre scientific objectives to achieve the ultimate aim, which is 'To create a step-change in the treatment, diagnosis and rehabilitation of arthritis via interdisciplinary research investigating relationships between mechanical loading, joint function, pain and inflammation.'

Through the collaboration between ARUKBBC and the Cardiff and Vale Orthopeadic Centre, University Hospital Llandough Cardiff, a pipeline has been set up for collecting both mechanical and biological data, pre and post HTO surgery for suitable patients. Utilising non-invasive engineering methods such as motion capture with force plates and musculoskeletal modeling to capture mechanical changes including gait patterns, range of motion and joint forces.

In a HTO, a plate is used to secure the position of the wedge introduced in the tibial plateau. Fixations of these plates require bone tissue to be removed. A second surgery is required 6-12 months after the first operation to remove the plate, during which further bone tissues are excised as part of the normal procedures. These excised bone tissue will be used for investigating biological changes in the joint tissues using gene expression studies.

A method for determining the stresses and strains experienced in the tissues for better correlation of the mechanical and biological data is required. Direct measurement of joint contact forces in an intact joint requires invasive implantation of force gauges and pressure sensing devices[15]. At the current state of technological development, direct measurement in a large cohort of HTO patients will be ethically, economically and practically impossible.

Biological systems are complex in geometry, mechanical and biological behaviour. Decades of research since the 1970s have been dedicated to the development of computational modelling for the study of biomechanics[16]. Musculoskeletal modeling can be used to predict muscle forces and resultant joint loads. However, effects of the soft tissue deformation and displacement are neglected. Finite element (FE) modeling allows detailed simulation of soft tissue biomechanics and a 2D FE foot model has been successfully coupled with a full lower limb musculoskeletal model for simulation of tissue mechanics during gait loading[17] and jumping[18].

Various finite element models of the knee can be found in the literature[19 20 21]. Though the meniscotibial ligaments are believed to play a significant role in the stabilization of the knee, they are rarely included in full joint contact FE knee models. A previous study carried out in the validation of a FE knee models using imaging methods on cadaveric specimens has highlighted the significance of the meniscotibial ligaments for accurate tissue kinematic predictions[22]. Little is known or found in the literature regarding the meniscotibial ligaments. It is believed that improvement in the understanding of the meniscotibial ligaments mechanical behavior will aid FE knee model prediction accuracy.

Full joint contact FE models have also been developed for other musculoskeletal joints including the wrist[23 24], ankle[25], spine[26 27]and shoulder[28]. Although built to investigate different musculoskeletal problems, developments of these models have common challenges. In addition to the inherent issues regarding choice of appropriate FE algorithm, mesh, contact and material definitions associated with any FE model[29], models for biomedical applications need to overcome problems arising from inter- and intra-patient[30] variability, such as real joint loading conditions, tissue geometry, tissue material properties and tissue constraints.

This project aimed to initiate the development of patient specific knee models with the future incorporation of patient specific joint loads calculated from gait analysis and musculoskeletal modeling. Capable of predicting stresses and strains, the FE model will provide a more biologically relevant understanding of the mechanical state inside the tissues of the knee joint. It is believed that if a correlation between FE predictions and results from biological studies could be established, the FE models could form a tool for the ARUKBBC in the future as part of the pipeline for studying the HTO cohort and hence, development of OA.

Validation of the full joint contact FE model of the knee will be required and will be done via the use of dynamic imaging methods. Therefore, the knee model in this

Phd research project has been developed in parallel with another PhD research project looking at the use of dynamic and loaded MRI to measure soft tissue kinematics in vivo.

The correlation of FE predictions and gene expression results is not an established method and require proof of concept. This has been attempted by working in conjunction with one of the other many projects within the ARUKBBC, looking at differences in gene expressions in AC explants subjected to OA and healthy gait patterns. The structure of the HTO project and the intended contribution of this PhD research project in relation to other research projects are summarised in Figure 1.2.

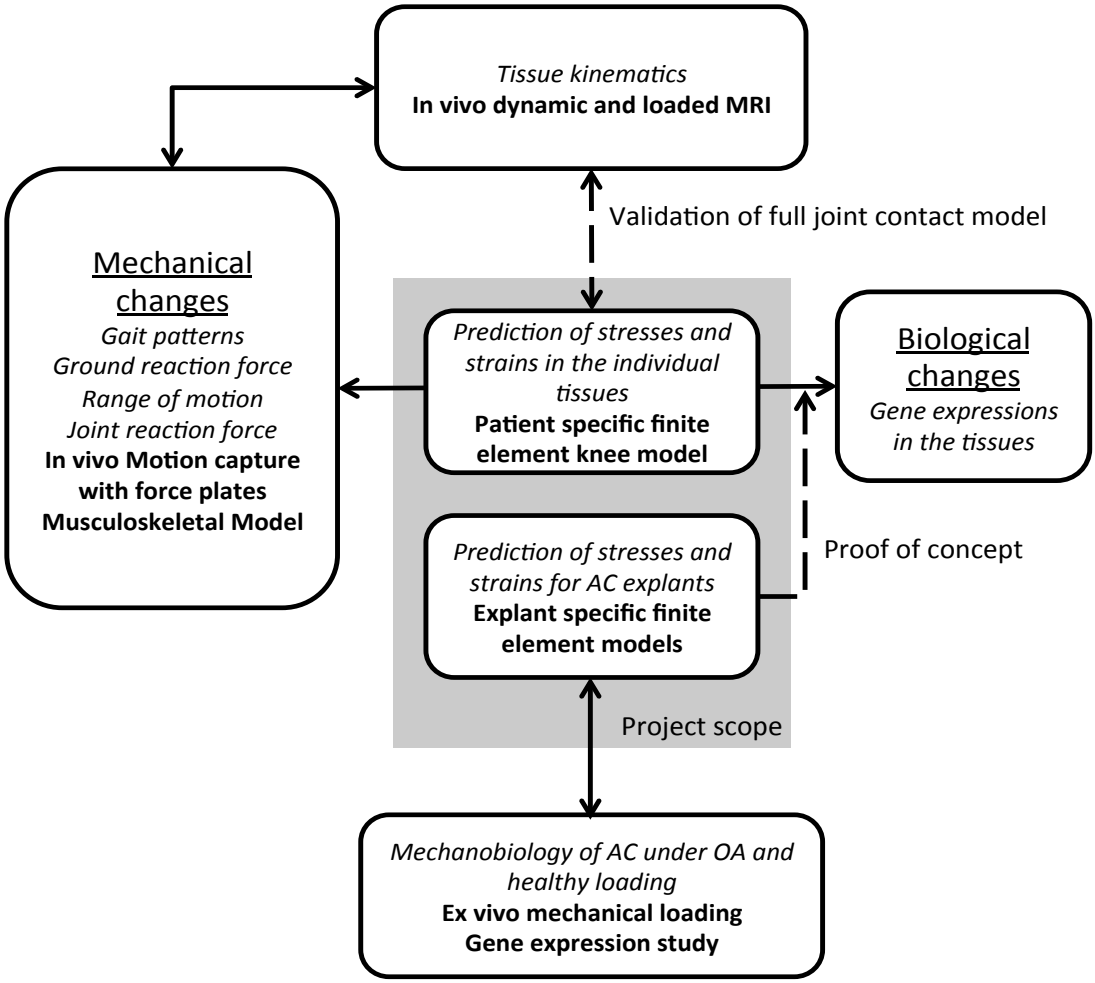

Figure 1.2 Structure and scope of this PhD research

1.1 Aims and Organisation of this thesis

1.1.1 Aims and objectives

Uncertainties relating to the development of patient specific FE knee models for the ARUKBBC in studying the HTO cohort addressed in this research are:

1) Proof of concept for correlation between FE stress and strain predictions with gene expression study results.
    a) The suitability of current AC constitutive models found In the literature
2) Reconstruction of finite element models with patient specific tissue geometries for the volunteers at the ARUKBBC.
    a) Accurate delineation and segmentation of the tissue geometries
    b) Errors in tissue geometry and dimensions arising from the meshing process
3) Better understand the MTLs for inclusion in the FE knee model.
    a) Anatomy and microstructure of the MTLs
    b) Their inclusion in the full joint contact FE knee models

1.1.2 Organisation of this thesis

Four separate studies have been carried out to address the aims listed in Section 1.1.1 and are detailed in Chapter 3-6 of this thesis.

Chapter 2 –Literature Review: This chapter provides background information on the human knee joint and its tissues. The technical background behind the tools and methods used in the studies are also outlined and a review of the current finite element knee models and constitutive models for articular cartilage found in literature are presented.

Chapter 3 –Aim 1: This chapter details a FE study performed in conjunction with a gene expression study investigating the differences in AC under OA and physiological loading. Building on current developments in constitutive models for

modeling the mechanical behavior of AC, a strong emphasis was placed on investigating the issue of non-uniform surface geometry of explants used for gene expression studies. A protocol for generating explant-specific FE models that allows surface preservation of the AC explants is detailed. Conducted on human AC obtained from the morphologically intact condyle of a total knee replacement patient, this study also provides material properties data for intact diseased AC, similar to that expected in HTO patients.

Chapter 4 –Aim 2: The possibility of accurate delineation and segmentation of both hard and soft tissue geometries from MR imaging scan data of a healthy volunteer for segmentation purpose was assessed. The use of the hybrid meshing algorithm in image processing software, Simpleware, Simpleware Ltd. for generation of tetrahedral only meshes for the tissues was also explored.

Chapter 5- Aim 3: Excised human knee joints were collected from TKR surgery for investigating the presence and anatomy of the MTLs. The CF orientation in the microstructure of the MTLs was also examined under cross polarised light microscopy and the results are presented in this chapter.

Chapter 6 –Aim 3: Based on the findings of Chapter 4, which is in contrary to current assumptions of CF arrangement in MTLs. This chapter details the new method proposed for modelling MTLs in full joint contact FE knee models.

Chapter 7 – Conclusion of the thesis and suggested future work

1.2 References

[1] Arthritis Research UK, www.arthritisresearchuk.org/~/media/.../Arthritis%20key%20facts.ashx [Accessed: 30th June 2013]

[2] Thomas E., Peat G., Harris L., Wilkie R. and Croft P.R., 'The prevalence of pain and pain interference in a general population of older adults: cross-sectional findings from the North Staffordshire Osteoarthritis Project', Pain, 110 (1-2): 361-368, 2004

[3] Department for work and pensions, www.dwp.gov.uk [Accessed: 19th January 2011]

[4] R. Bitton, 'The economic burden of osteoarthritis', Am J Manag Care, 15(8):S230-5

[5] S. Gupta, G.A. Hawker, A. Laporte, R. Croxford and P.C. Coyte, 'The economic burden of disabling hip and knee osteoarthritis (OA) from the perspective of individuals living with this condition', Rheumatology, 44(12):1531-1537, 2005

[6] A. Chen, C. Gupte, K. Akhtar, P. Smith and J. Cobb, 'The global economic cost of osteoarthritis: how the UK compares', Arthritis, vol. 2012, Article ID 698709, 6 pages, 2012 doi:10.1155/2012/698709

[7] National Joint Registry, www.njrcentre.org.uk [Accessed: 19th January 2011]

[8] D.B. Slocum, R.L. Larson, S.L. James and R. Grenier, 'High Tibial Osteotomy', Clinical Orthopaedics & Related Research, 104:239-243, 1974

[9] Orthopale, http://www.orthopale.com/tibial-osteotomy.php [Accessed: 9th January 2014]

[10] S. Akizuki, A. Shibakawa, T. Takizawa, I. Yamazaki and H. Horiuchi, 'The long-term outcome of high tibial osteotomy: A ten to twenty year follow up', The Journal of bone and joint surgery (Br), 90(B): 592-596, 2008

[11] W.C. Tang and I.J. Henderson, 'High tibial osteotomy: Long term survival analysis and patients' perspective', Knee, 12: 410-413, 2005

[12] D. Naudie, R.B. Bourne, C.H. Rorabeck and T.J. Bourne, 'Survivorship of the high tibial osteotomy: a 10 to 22 year follow-up study', Clinical Orthopaedics, 367:18-27, 1999

[13] C.C. Prodromos, T.P. Andriacchi and J.O. Galante, 'A relationship between gait and clinical changes following high tibial osteotomy', The Journal of Bone and Joint Surgery, 67(8):1188-1194, 1985

[14] Y. Fujisawa, K. Masuhara and S. Shiomi, 'The effect of high tibial osteotomy on osteoarthritis of the knee. An arthroscopic study of 54 knee joint', The Orthopaedic Clinics of North America, 10(3): 585-608, 1979

[15] T. Fukubayashi and H. Kurosawa, 'The contact area and pressure distribution pattern of the knee: A study of normal and osetoarthrotic knee joints', Acta Orthopaedica, 51(1):871-879

[16] T.W. Lu, H.S. Gill and J.J. O'Connor, 'An interactive graphics-based window interface for geometric and mechanical modelling of the lower limb', Computer Methods in Biomechanics and Biomedical Engineering, London :Gordon & Breach, 497-506, 1997, Print

[17] J.P. Halloran, M. Ackermann, A. Erdemir, A. J. van den Bogert, 'Concurrent musculoskeletal dynamics and finite element analysis predicts altered gait patterns to reduce foot tissue loading', Journal of Biomechanics, 43:2810-2815, 2010

[18] J.P. Halloran, A. Erdemir and A.J. van den Bogert, 'Adaptive surrogate modeling for efficient coupling of musculoskeletal control and tissue deformation models', Journal of Biomechanical Engineering, 131(1):011014, doi:10.1115/1.30053333, 2009

[19] P. Beillas, G. Papaioannou, S. Tashman and K.H. Yang, 'A new method to investigate in vivo knee behaviour using a finite element model of the lower limb', Journal of Biomechanics, 37:1019-1030, 2004

[20] E. Peña, B. Calvo, M.A. Martínez and M.Doblaré, ' A three-dimensional finite element analysis of the combined behaviour of ligaments and menisci in the healthy human knee joint', Journal of Biomechanics, 39: 1686-1701, 2006

[21] T.L. Haut Donahue, M.L. Hull, M.M. Rashid and C.R. Jacobs, 'A finite element model of the human knee joint for the study of tibio-femoral contact', Journal of Biomechanical Engineering, 124:273-280, 2002

[22] J. Yao, J. Snibbe, M. Maloney and A.L. Lerner, 'Stresses and strains in the medial meniscus of an ACL deficient knee under anterior loading: a finite element analysis with image-based experimental validation', Journal of Biomechanical Engineering, 128:135-141, 2006

[23] M.K. Gislason, D.H Nash, A. Nicol, A. Kanellopoulos, M. Bransby-Zachary, T. Hems, B. Condon and B. Stansfield, 'A three-dimensional finite element model of maximal grip loading in the human wrist', Proceedings of the Institute of Mechanical Engineers, Part H: Journal of Engineering in Medicine, 223: 849-861, 2009

[24] S.D. Carrigan, R.A. Whiteside, D.R. Pichora and C.F. Small, 'Development of a three-dimensional finite element model for carpal load transmission in a static neutral posture', Annals of Biomedical Engineering, 31(6), 718-725, 2003

[25] F.A. Bandak, R.E. Tannous, T. Toridis, 'On the development of an osseo-ligamentous finite eleent model of the human knee joint', International Journal of Solids and Structures, 38:1681-1697, 2001

[26] N. Yoganandan, S. Kumaresan, L. Voo and F.A. Pintar, 'Finite element applications in human cervical spine modeling', Spine, 21(15):1824-1834, 1996

[27] F. Ben-Hatira, K. Saidane and A. Mrabet, 'A finite element modelling of the human lumbar unit including the spinal cord', Journal of Biomedical Science and Engineering, 5:146-152, 2012

[28] P. Büchler, N.A. Ramaniraka, L.R. Rakotomanana, J.P. Iannotti and A. Farron, 'A finite element model of the shoulder: application to the comparison of normal and osteoarthritic joints', Clinical Biomechanics, 17(9): 630-639, 2002

[29] R. Huiskes and E.Y.S. Chao, 'A survey of finite element analysis in orthopaedic biomechanics: the first decade', Journal of Biomechanics, 16(6), 385-409, 1983

[30] D.L. Butler, Y. Guan, M.D. Kay, J.F. Cummings, S.M. Feder and M.S. Levy, 'Location-dependent variations in the material properties of the anterior cruciate ligament', Journal of Biomechanics, 25(5): 511-518, 1992

Chapter 2 Literature Review

Owing to an elaborate intricate arrangement of tissues with function specific geometries, material properties and ligament constraints, the knee is a versatile joint capable of motion in all 6 DOFs with high weight bearing abilities. However, due to inter-patient variability and the complexity of the system, the combined and isolated contribution of each tissue to the stabilisation and load carrying function of the knee joint is still not fully understood[1 2].

Although technological advancements has made available computational power capable of solving complex FE models with DOFs on the scale of millions[3], a computational model, which provides an exact description of all the components in the knee joint and their interaction is impossible and simplifications are required[4]. Errors in the description of the mechanical behaviour, geometry and constraint of each tissue can have a profound impact on the accuracy of the model. Therefore, assumptions and simplifications made must be carefully examined and of an informed decision. Parametric studies examining the effects of input variability have given insight into the significance of certain generalisations.

This literature review provides a background on the system being modelled, the human knee joint, and a review of previous published FE knee models. A further discussion on the segmentation and meshing algorithms for reconstruction of tissue geometries from patient specific MR image data is presented.

2.1 The Human Knee Joint

2.1.1 Anatomical and biomechanics terminology

Standard terminology for anatomical planes include sagittal, coronal and transverse plane, and axis are commonly referred to as anterior-posterior (AP), medial-lateral (ML) and superior-inferior (SI) axis; this nomenclature will be used throughout this thesis (Figure 2.1).

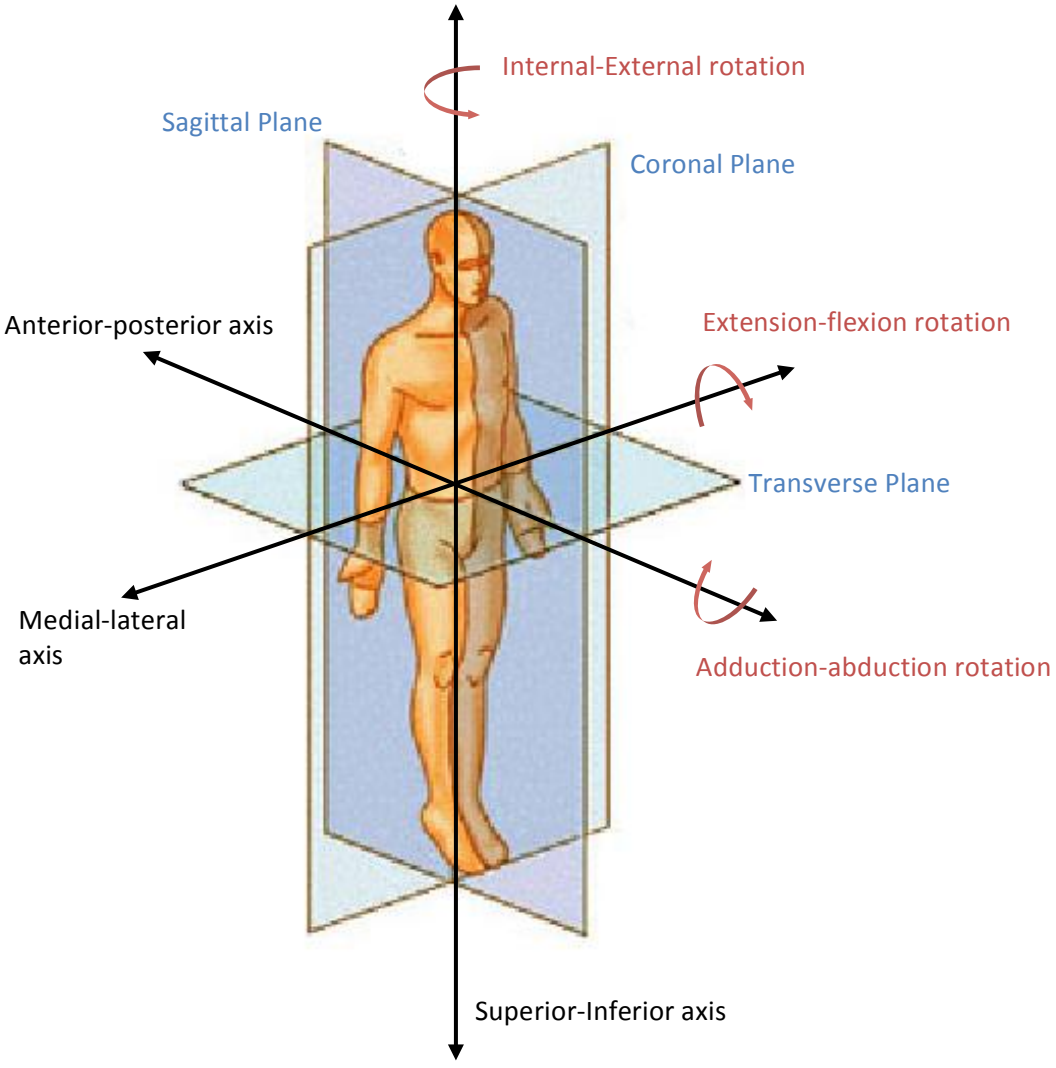

Figure 2.1 Body planes and axis terminology (Image from National Cancer Institute[5]).

Anterior refers to the direction towards the front of the body and posterior to the back; Medial is towards the centre of the body and lateral away from the centre; Superior is towards the upper part of the body, and inferior towards the lower part. The plane formed between the SI and AP axis is the sagittal plane, between the SI-ML axis is the coronal plane and between the AP-ML is the transverse plane.

Following on from the convention for axis classification, the three degrees of translation between the tibiofemoral contact will be referred to as anterior-posterior, medial-lateral and superior-inferior. The three degrees of rotation will be referred to as extension-flexion about the ML axis, adduction-abduction about the AP axis and internal-external about the SI axis[6].

2.1.2 Anatomy of the human knee

The human knee joint comprises of four bones: femur, tibia, patella and fibula (Figure2.2). Articulation of the knee involves tibiofemoral contact between the tibia and femur, and patellofemoral contact between the patella and femur. AC, a thin layer of soft tissue with a low coefficient of friction of approximately 0.001[15], is found on the contact surfaces of each articulating bone.

Between each of the femoral condyles, medial and lateral condyles, and their respective contacting surfaces, the medial and lateral tibial plateaus are two semi-lunar shaped fibrous soft tissues, the medial and lateral menisci. Constraining the motions of the the patello-tibio-femoral joint are five major ligaments; patella ligament, MCL, LCL, ACL and PCL (Figure 2.2).

Linked to the quadriceps tendon, the patella ligament constraints the motion of the patella and helps stabilise flexion and extension of the knee. The ACL and PCL found in the centre of the joint attach the femur to the tibia and help constrain relative anterior-posterior, as well as, ML motion between the two parts. The MCL and ACL connect the femur to the tibia and fibula respectively. Found on either side of the

knee joint, these ligaments help prevent excessive adduction-abduction and internal-external rotation of the knee.

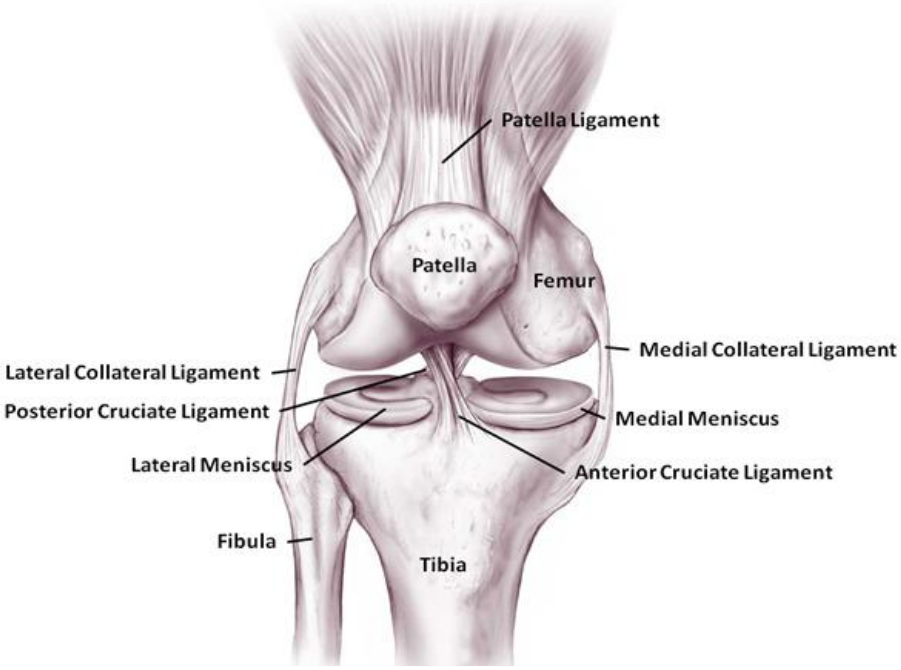

Figure 2.2 Anatomy of the Knee. Bones: Femur, Tibia, Fibula and Patella. Ligaments: Patella ligament, MCL, LCL, ACL and PCL. Medial and lateral menisci are located between the tibiofemoral contact area (Image from HealthPages[7]).

2.1.3 Collagen

Collagen is a naturally occurring protein found in the human body. It is a triple helix of three polypeptide alpha-helix chains twisted together and is approximated to be 300nm long with a diameter of 1.5nm. Collagen can arrange themselves into super molecular aggregates and are categorised into types, namely Type I, II, III and etc. In total, there are 26 types of collagen identified[8], with the majority of collagen found in the human body being of Type I, II and III[9].

Type I collagen, along with Type II and Type III collagen form fibres of diameter ranging from 50nm -200nm. Typically several micrometres in length they can be arranged to align parallel to each other and form collagen fibres with diameters of 1

-12µm[10]. Due to the parallel arrangement of fibrils, Type I collagen exhibit birefringence properties.

In comparison to Type I collagen, Type II collagen is smaller in diameter, approximately 10-300nm. Type II collagen is known to form fibrils that can be arranged to intertwine with each other forming a fibular network[11].

2.1.3.1 Cross polarised light microscopy

Cross polarised light microscopy involves the use of two polarising filters. Light is polarised by the first filter before it is passed through the specimen. When the plane polarised light passes through the birefringent material, the light is separated into two rays vibrating in a plane perpendicular to each other. The two rays travel at different velocities and become out of phase. As the two rays travel through the second filter, they are recombined and the resultant wave of the two interfering waves is observed[12] (Figure 2.3). In the case where the specimen is not birefringent, no light will be transmitted through the second polarising filter.

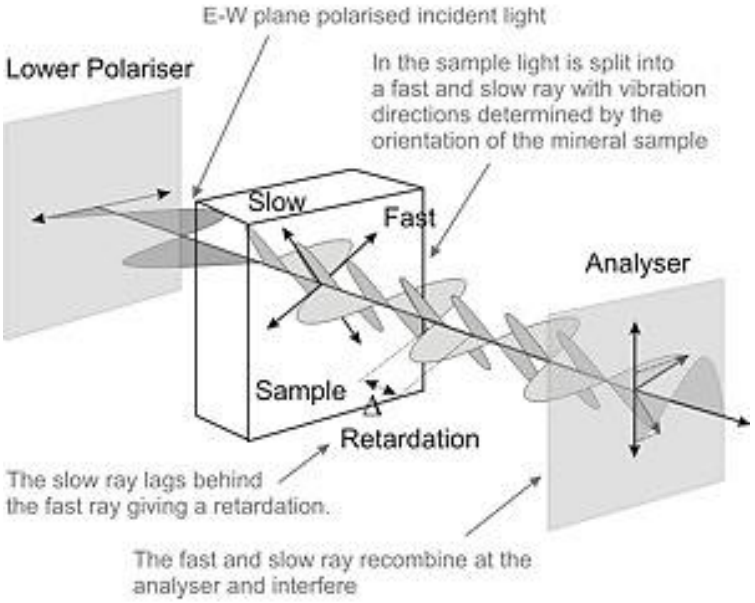

Figure 2.3 Principal of cross polarised light microscopy (Image from Imperial College Rock Library[12])

The optic axis of a material is the orientation in which no birefringence occurs. In collagen fibres, the optic axis lies parallel to the long axis of the fibres. Therefore, when the polarising filter is aligned parallel to the fibre orientation, no light will pass and the material will appear dark in the microscopy image[13 14].

2.1.4 Articular Cartilage

2.1.4.1 Microstructure of articular cartilage

AC has a complex inhomogeneous microstructure, consisting of proteoglycans (PGs), collagen (primarily Type II collagen) and interstitial fluid; interstitial fluid accounts for 70-85% of the wet weight of the tissue and collagen fibrils make up 50-75% of the dry weight[15]. PGs are aggregated branched macromolecules comprising negatively charged sulphated GAGs such as Chondroitin Sulphate and Keratan Sulphate covalently bonded to Hyaluronic Acid core protein, giving rise to a charged ECM with a FCD (Figure 2.4). The negatively charged PGs repel each other and attract the positive ions in the interstitial fluid to maintain electro-neutrality within the tissue. As a result, ion concentration in the tissue is higher than that of the external environment and water is attracted into the matrix causing the tissue to swell. Intertwined within the collagen fibrils that are stiff in tension but weak in compression, the collagen fibrils resist the infinite expansion of the matrix.

Collagen fibril organisation[16] and water content, as well as ECM composition varies throughout the depth of the tissue (Figure 2.5). Therefore, the tissue is typically described as having four distinct zones; superficial or superficial tangential zone, intermediate or middle zone, deep zone and calcified zone.

The superficial zone comprises the uppermost 10-20% of the tissue, where collagen concentration is highest and the fibrils predominately align parallel to the articulating surface. Fibrils are comparatively finer and are strongly cross-linked to

give good resistance to shear forces induced between the two articulating bones. Water content is found to be highest in this zone and decreases with depth.

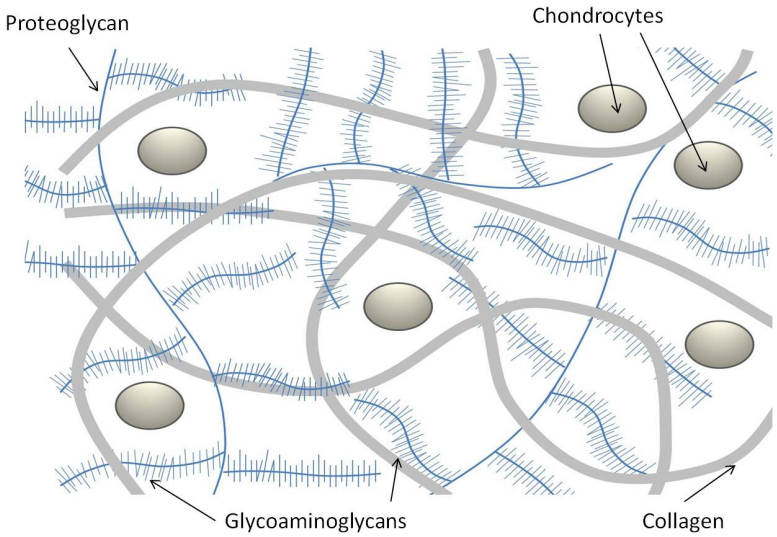

Figure 2.4 Extracellular matrix of articular cartilage

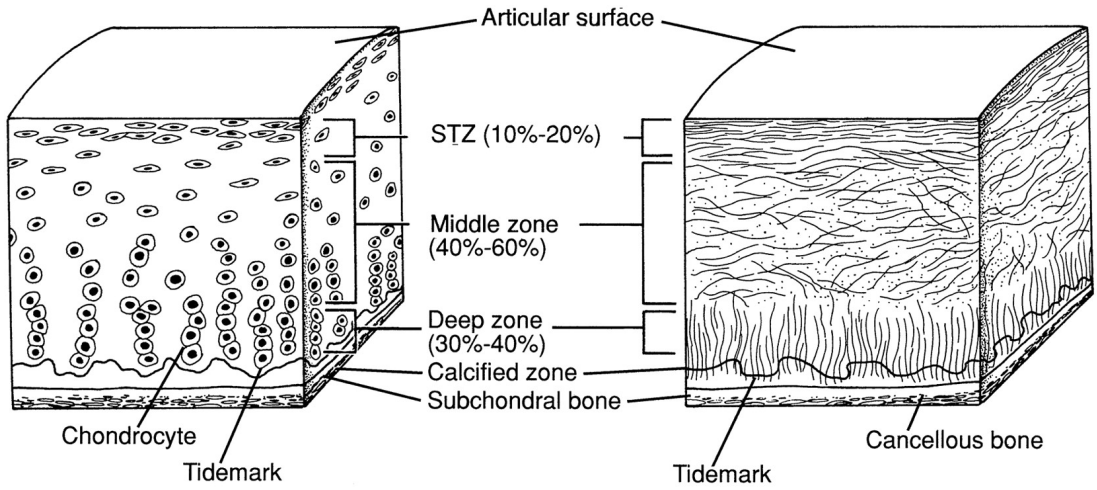

Figure 2.5 Depth dependent microstructure of articular cartilage[17]

Below the superficial zone, and comprising 40-60% of the tissue thickness, is the intermediate zone where the collagen fibrils are randomly orientated. Below this resides the deep zone where collagen fibril density is greatest and fibrils are arranged perpendicular to the articulating surface.

The calcified zone separates the deep zone from the underlying subchondral bone. It is distinguished from the deep zone by an interface called the tidemark. PG content in this layer is lowest and due to calcification, the cartilage is found in the form of crystal calcium salt. Collagen fibrils have larger diameters and are highly orientated perpendicular to the surface of the articulating bones. Fibrils from the deep zone extend into this layer which allows the tissue to fix securely onto the subchondral bone. The rugged contour of the tidemark and the interface between the calcified zone and the subchondral bone prevents slipping of the layers and provides resistance against shear forces[18].

2.1.4.2 Mechanobiology of articular cartilage

Found embedded in the lacunae of the ECM are chondrocytes, the only cell type in AC. During mechanical loading of the bulk tissue, stresses and strains of the ECM are transferred to the chondrocytes via the pericellular matrix (PCM) and interstitial fluid movement.

The PCM is the tissue region immediately surrounding the chondrocytes[19]. The PCM is differentiated from the ECM due to a difference in composition and material properties. Type VI collagen is found in the PCM as opposed to Type II collagen in the ECM. Permeability and Young's modulus of the PCM is lower than that of the ECM by a factor of 25 and 10; where the Young's modulus of the ECM and PCM are in the region of 400kPa and 40kPa for reference. The more compliant nature of the PCM allows larger strains, which can be up to 5 times higher[20], in the tissue surrounding the chondrocytes. Thereby, reducing stresses in the chondrocytes. These effects are termed, local strain amplification and stress shielding. In addition, the less permeable nature of the PCM is believed to help shield the chondrocytes from excessive fluid flow loading[21].

Upon receiving a mechanical stimulus from its surrounding environment, the expressions of different genes in the nuclei of the chondrocytes are triggered.

Genes that have been found to be mechanically sensitive, include those that regulate ECM molecules (such as aggrecan and type II collagen, which encourage anabolic activities), cell cycle growth proteins, cytokines, growth factors, matrix metalloproteinases (molecules encouraging catabolic activities), angiogenic and antiangiogenic factors[22].

Mechanical forces experienced by the chondrocytes can be of 4 types; compression, shear, hydrostatic and osmotic. Previous research has found that regulation of gene expressions are linked to the type and magnitude of mechanical stimulus. Dynamic compression (10-20MPa), shear stress, hydrostatic pressure where found to upregulate gene expressions for aggrecan and type II collagen, favouring anabolic activities. Though, static compression (~3.5MPa) and osmotic pressure were found to encourage catabolic activities. Static compression downregulates gene expressions for aggrecan and type II collagen and osmotic pressure upregulates gene expression of catabolic mRNA.

The cascade of biological events culminates in the synthesis or degradation of ECM, which govern the material properties of the tissue[23 24 25]. This mechanobiological mechanism allows the tissue to undergo necessary adaptation to cope with functional demands and maintain tissue health[26 27]. In cases where the fine metabolic balance is disrupted, the tissue undergoes significant changes in its composition, leading to load-induced tissue degeneration and the development of OA[28].

2.1.4.3 Mechanical behaviour of articular cartilage and OA

During mechanical loading of AC, the load is shared between the ECM and the interstitial fluid. Both the ECM and the interstitial fluid components are incompressible individually. However, as the interstitial fluid is free to flow in and out of the matrix, this interaction gives rise to a material that is compressible. As the material is compressed, interstitial fluid flows out of the matrix and the rate of

interstitial fluid loss varies with time. Constitutively, the material can be said to exhibit time-dependent behaviour and is viscoelastic.

Two mechanisms contribute to the bulk tissue viscoelasticity in AC, namely the flow dependent and flow independent viscoelasticity. Flow independent viscoelasticity arises due to the non-linear viscoelasticity of the collagen fibrils[29]. Flow dependent viscoelasticity arises due to the fluid flow through the ECM, also referred to as poroelasticity and such materials are described as biphasic.

Extension of AC constitutive models to triphasic, allows the effects of electrochemical interactions of the charged ECM and ionic interstitial fluid to be modelled. There are two types of electrochemical interactions, chemical expansion and osmotic pressure. During compression, the charged proteoglycans in the ECM are brought together closer in proximity, thereby, increasing the FCD of the ECM. Consequentially, the increase in FCD attracts the ions in the interstitial fluid and increases the ionic concentration of the interstitial fluid within the ECM. The increased ionic concentration gives rise to an osmotic pressure, which attracts fluid into the ECM.

It is evident that interstitial fluid content is a major determinate of the mechanical behaviour of AC. In OA AC, the collagen network becomes degenerated. As a result, the matrix has a lower resistance in tension and the swelling behaviour is exaggerated[30]. Consequently, water content is higher in OA AC, altering both the instantaneous and time dependent mechanical behaviour.

2.1.4.4 Constitutive models for articular cartilage

Linear biphasic model

Biphasic models are implemented into FE models via the capabilities for poroelasticity. A linear biphasic model would include a young's modulus and

poison's ratio for describing the matrix behaviour and a constant permeability for the flow of the interstitial fluid.

Non-linear biphasic model

The biphasic theory can be extended to include non-linear effects, by implementing the equation for depth dependent void ratio, otherwise referred to as water content, equation 2.1 and the equation for strain dependent permeability, equation 2.2.

$$e_o = \hat{e}_o \left(1 - \alpha_e \left(1 - \frac{z}{h}\right)\right) \quad (2.1)$$

$$k = k_o \left(\frac{1+e}{1+e_o}\right)^m \quad (2.2)$$

where h is the total thickness of the cartilage, z is the vertical distance from the bottom surface, e_o is the initial void ratio at z, $\hat{e}_o$ is the initial void ratio at height h (surface of the cartilage), α_e is the void ratio coefficient, e is the current void ratio, k is the permeability for current void ratio, k_o is the initial reference permeability and m is a constant coefficient.

Non-linear poroviscoelastic model

Further extension to this theory is a poroviscoelastic model[31] where the viscoelasticity of the matrix arising due to the collagen fibrils, i.e. fluid independent viscoelasticity, is implemented using a prony series, equation 2.3.

$$G_{(t)} = G_\infty + \sum_{i=1}^{N} G_i \, exp\left(-\frac{t}{\tau_i}\right) \quad (2.3)$$

Biphasic swelling

Osmotic pressure gradient arises due to a difference in internal and external ion concentration, equation 2.4 and equation 2.5[32].

$$\Delta\pi = \pi - \pi_{ext} \qquad (2.4)$$

$$\pi = \xi RT(c^+ + c^-) \qquad (2.5)$$

Where $\Delta\pi$ is osmotic pressure gradient, π is the internal osmotic pressure, π_{ext} is external osmotic pressure, c^+ and c^- are the mobile cation and anion concentrations, ξ is the osmotic coefficient (for an ideal membrane it is 1), R is the molar gas constant and T is the absolute temperature.

Similarly, the dependency of the chemical expansion stress, T_c, on ion concentration can be expressed using the proposed equation 2.6[33].

$$T_c = \beta_o exp\left(-\frac{c}{c_\beta}\right) \qquad (2.6)$$

Where β_o and c_β are constant coefficients.

Implementation into FE can be done via a user subrountine for the inclusion of the osmotic pressure and chemical expansion stress in the calculation of stresses at each integration point[34].

2.1.5 Menisci

Measuring only a maximum thickness of 7mm [35], the menisci covers approximately 50% of the medial and lateral tibial plateaus[36], providing great stabilisation, load distribution and shock absorption for the tibiofemoral contact. The menisci have wedge-shaped cross sections which help improve congruity of the two articulating surfaces and increase contact area. Similar to AC, meniscal tissue is a fibre-reinforced biphasic material, comprising of 72% water[37] and 22% of collagen. Water content in the posterior portion of menisci is found to be higher compared to the anterior portion[35]. Organisation of the CFs in the meniscus varies with anatomical location[38]. Type I collagen, commonly found in tendons, is the main collagen type found in the tissue[39] whilst type II collagen is found only in the inner portion of the

menisci[40]. The surface layer, approximately 30-120μm thick consists of fibres randomly orientated parallel to the surface of the tissue[41]. In the deep zone, fibres are predominately orientated in the circumferential direction with smaller radial fibres holding the circumferential fibre bundles together[42]. Under compressive axial loading parallel to the SI axis, the load is transformed into a radial expansion force in the transverse plane which is resisted by the circumferential fibre bundles. This mechanism allows the medial and lateral meniscus to absorb 50% and 70%, respectively, of the axial load acting through the joint[43].

2.1.6 Meniscal attachments

The menisci are attached to the intercondylar eminence of the tibial plateau via the MA, MP, LA and LP meniscal horns. Connecting the anterior horns of the medial and lateral meniscus is the IML or transverse ligament (Figure 2.6).

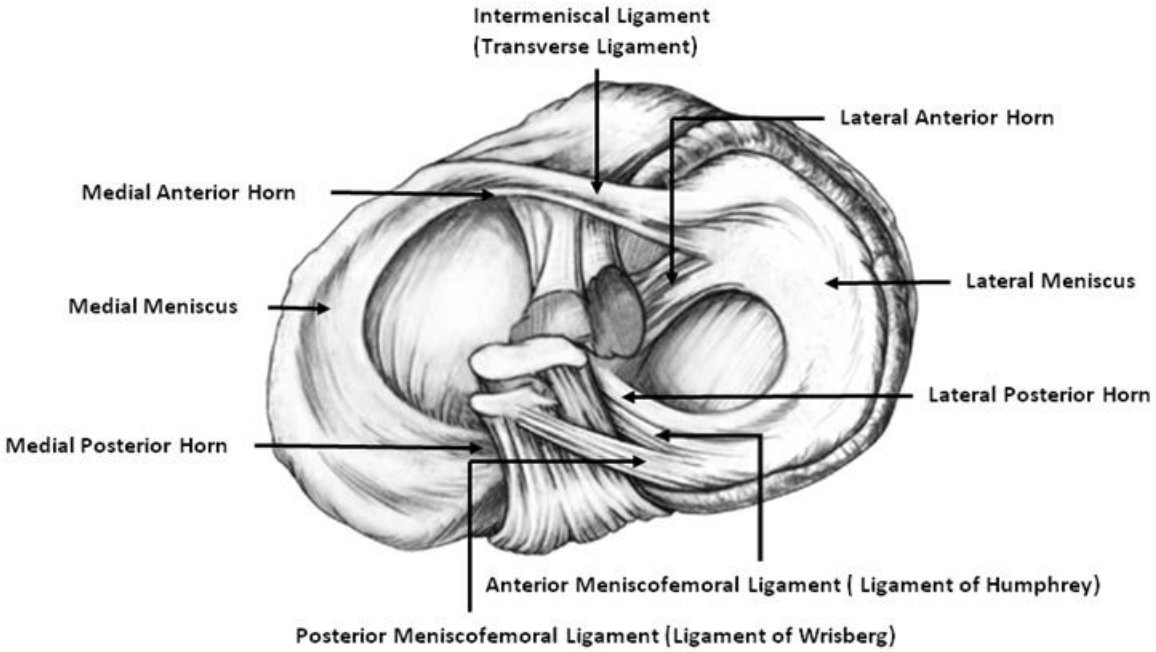

Figure 2.6 Attachments of both the lateral and medial meniscus. Attachments to the tibial plateau: LA horn, LP horn, MA horn, MP horn and coronary ligaments (not shown). Attachments to the femoral condyle: Anterior MFL and the posterior MFL (Image from Dodds et al. 2007[44]).

Ligamentous attachments to the femoral condyle are the anterior and posterior MFLs, which originate from the posterior horn on the lateral meniscus and extend to the lateral surface of the medial condyle[45].

The medial meniscus is known to be comparatively less mobile than the lateral meniscus[46]. This is widely believed to be due to its firm attachment to the MCL, although this has only been proven to be partly true due to the complex composition of the MCL. The MCL has previously been described as consisting of two layers: sMCL and dMCL[47].

The sMCL can be further separated into two portions; the parallel portion with CFs arranged parallel to the SI axis and the oblique portion at the posterior edge of the ligament where the fibres attach to the tibia. Anatomical dissection and histological assessment revealed and confirmed that the medial meniscus is only attached to the posterior oblique portion of the sMCL[45]; a bursae was found to separate the anterior parallel portion of the sMCL from the medial meniscus[48], therefore, only restricting posterior movements of the medial meniscus. The dMCL itself also comprises of two portions: the MFL, which attaches the periphery of the meniscus to the femoral condyle, and the MTL which attaches the periphery of the meniscus to the tibial plateau[49] (Figure 2.7).

Although debated by some, the MTLs, also known as the coronary ligaments, are present on both the medial and lateral sides of the knee[50], as reported in an anatomical dissection study on 85 cadaveric knees[51]. In this same study, it was concluded that MTLs are present in 25.53% of the population. No previous studies on their microstructure and mechanical behaviour were found in literature.

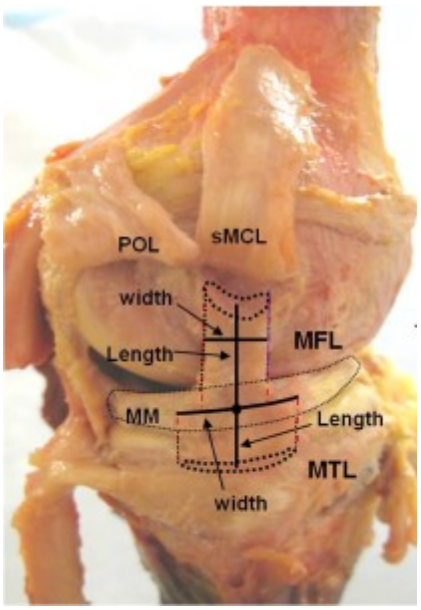

Figure 2.7 View of a knee from the medial side. The sMCL has been removed to reveal the Medial Meniscus. The location and size of the MFL and MTL are indicated by the dotted lines. (Image from LaPrade et al. 2007[49]).

2.2 Finite element models of the knee

Validated analytical models for studying knee joint biomechanics have been available since 1976[52]. The model included descriptions of bone geometries, physiological joint motion and material properties of the ligaments. However, there were no representations of the AC or menisci. Shortcomings of these analytical solutions are their limitations in complexity and the inability to determine stress and strain fields inside each tissue component. Due to the deformable nature of both the AC and the menisci, in conjunction with the significant effect their displacement and deformation has on the stabilisation of the knee, their inclusion would result in a system too complex for derivation of an analytical solution, proving the FE method an invaluable tool.

In a multipart FE model, description for the model domain, material behaviour, loading conditions, contacts and interaction behaviours are required. Accurate descriptions add complexity to the model and demand additional computational

resource. No model reduction may result in a model that takes an unrealistic amount of time to solve or even result in one that is unsolvable. Therefore, considerations must always be given to justify the necessity of such added extra complexity specific for the application of the model.

In the early 1990s, researchers were already fully aware of the influence tissue geometry had on the joint mechanics in the knee[53] and that accurate representations of these geometries in FE models are important. By 1997, a three dimensional full joint contact FE model of the knee with tissue geometries reconstructed from coordinate measuring machine data was developed. Used for studying internal-external loading and uniaxial compression in the SI axis, the model included rigid body bones, deformable linear isotropic AC, fibre reinforced nonlinear elastic menisci and cruciate ligaments. Definitions for the non-penetrating frictionless contact between the soft tissues were also implemented[54]. The study compared the contact pressures, contact area and internal-external rotations predicted from the FE model to previously published literature data and observed good agreement. Though, a shortcoming of the model is the use of hexehedral elements which introduces errors in the description of the tissue geometries. Furthermore, the lack of patellofemoral ligament prevented flexion-extension cases to be modelled. Although no evidence was shown for internal-rotation model prediction and experimental data, the author concluded that improved constitutive ligament models were required. No description was found for the implementation of meniscal constraints.

In 1999, Li et al. published a full joint contact FE model reconstructed from magnetic resonance imaging (MRI) data of a cadaveric specimen [55]. AP loads were applied to the tibia and the predicted knee kinematics was validated using kinematics data obtained from a robotic, universal force-moment sensor system for that same specimen. Compared to the model published in 1997 by Schmiedmayer et al.[54], a strong emphasis was placed on the non-linear mechanical behaviour of

the ligaments. The same constitutive mathematical model was used as that in Schmiedmayer's model; however, Li et al. had different spring stiffness and initial ligament length for the different bundles of ligaments. The separate bundles forming the ligaments, ACL, PCL, MCL, LCL and the superficial and deep MCL were modelled separately. A total of 12 ligament bundles were modelled. The nonlinear behaviour of the springs was defined using equation 2.7.

$$f = \begin{cases} {}^{1}/_{4}\, k\, {\varepsilon^2}/_{\varepsilon_I}, & 0 \le \varepsilon \le 2\varepsilon_I \\ k(\varepsilon - \varepsilon_I), & \varepsilon \ge 2\varepsilon_I \\ 0, & \varepsilon < 0 \end{cases} \quad (2.7)$$

$$\varepsilon = \frac{(l - l_o)}{l_o} \quad (2.8)$$

where k is the spring stiffness, l is the deformed ligament length, l_o is the initial ligament length and ε_I is arbitrary parameter chosen to be 0.03.

The model included rigid body bones meshed with 4 nodes surface elements and deformable AC meshed with 8 node hexahedral elements. The menisci were represented using three springs for each condyle with spring stiffness that varied with the flexion angle of the knee. The spring stiffness for the menisci were determined inversely by minimizing the error between the tibial displacements predicted by the FE model and that measured experimentally under AP loads at various flexion angles. Internal-external moments were applied to the model and the rotations predicted compared to experimental data and showed good correlation at both 0 and 30 degrees flexion angles, validating the ligament models. However, a shortcoming of this FE knee model is the lack of geometrical representation of the menisci. In such a model, contact mechanics cannot be predicted. The importance of the meniscal representation is further discussed below.

With great interest in meniscal replacements, Haut Donahue et al. developed a tibiofemoral FE model of the knee to carry out parametric studies on variables such as meniscal size, shape, material properties and attachment stiffness [56 57]. Validation of this model proved that, providing mesh convergence of the solution is observed, modelling the bones as rigid bodies introduced an error in the predicted contact variables of less than 2% and is therefore acceptable. It was however found that large errors were introduced due to non-physiological restrictions on internal-external and adduction-abduction rotations for model simplification purposes.

Geometries of the tissues were obtained from a cadaveric specimen. The bones were reconstructed from segmentation of CT scan data and the soft tissues from a laser-based coordinate digitising system after dissection. The model domain included the AC, menisci, the meniscal horns, ACL, dMCL and the transverse ligament. The ACL and dMCL were modelled using non-linear springs defined using equation 2.7. A transversely isotropic model was used for the menisci, and the mensical horns were modelled as 10 linear springs with a spring stiffness of 200N/mm. IML was included in the model and represented by a single linear spring. The model was meshed with 8 node trilinear hexahedral elements. The need for dissection to obtain the soft tissue geometries deems this method unsuitable for the purpose of this research. However, the work from Haut Donahue et al. provided useful findings and conclusions with regards to significance of meniscal geometry and representation of the bones.

Parametric studies carried out using this FE model found that contact pressure distribution was sensitive to circumferential modulus, axial/radial modulus and horn stiffness; the predictions were comparatively insensitive to the Poisson ratios, shear modulus, the stiffness of the transverse ligament and the non-linear stiffness and initial strain of the MCL. Using the same model, it was further established that the variation in the size of the meniscus could affect model predictions significantly [58]. It was found that the predicted contact variables were comparatively more

affected by variations in medial meniscus size, where a variation of 0.5mm and 1mm in thickness of the medial meniscus and lateral meniscus respectively resulted in a 10% change in the predictions. It was observed that variations in the medial meniscus geometry had a greater effect on FE predictions than variations in the lateral meniscus geometry. Meakin et al. using a simplified axis-symmetric model of the knee also reported on the significance of geometrical congruency between the articulating surfaces[59].

Although not generated from actual tissue geometries, similar models with computer generated realistic geometries were developed by Jilani et al. and Moglo et al. to investigate the coupling between the four major ligaments, ACL, PCL, MCL and LCL, under axial rotation[60] and AP draw for ligament reconstruction surgery in knees with ACL or PCL injury[61]. The behaviour of the ligaments was found to be heavily coupled. Changes in the mechanical behaviour or resection of one ligament significantly changed the behaviour of the other ligaments particularly during internal-external and flexion-extension rotations of the knee. The model domain included AC and menisci meshed using 8 node solid elements with spring elements representing the ligaments. Linear elastic properties were used for the AC and meniscus. The model included the MCL attachment to the meniscus, however, no validation against experimental data was provided.

For the purpose of investigating the effects of meniscal tears and menisectomies, Peña et al. also developed a quasi-static FE model[62], similar to those reported previously[58 59 60 61]. Bone geometries were reconstructed from CT scan data and the soft tissue geometries, including AC, menisci and ligaments, from MR imaging data. Their later model included the addition of the patella ligament and implemented a hyperelastic transversely isotropic constitutive model for all ligaments. The model examined the effects of meniscal tears and meniscectomy under uniaxial compression and demonstrated its importance in knee joint stability[63]. This model is a validated complete full joint contact model with scan data generated

geometries of all bones (patella, femur, tibia, fibula), articular cartilage, menisci and ligaments (ACL, PCL, Patellofemoral, MCL and LCL), the most extensive in tissue geometry and consideration of suitable constitutive soft tissue models.

In 2006, Yao et al. published a partial knee model which included the MTLs [64]. Although the model only included the medial compartment for the study of ACL deficiency, substantial work was done to validate the model using MR image data of a loaded cadaveric specimen. Bone kinematics measured from MR images were defined for producing 45, 76 and 107 N of anterior loading and applied to the FE model. Predicted meniscal deformation and displacement was then compared to MR images for validation. The study concluded that while predictions from the FE model were comparable to those measured from MR images, errors in local meniscal deformation and translation were observed and was due to unknown mechanical properties of the MTLs. Although, only a partial knee model, this is the first and only model found in literature to include the representation of MTLs.

Whilst the quasi-static deformable models already mentioned have proven invaluable for predicting contact variables and tissue stresses, a downfall of these models are their lack of ability to handle highly non-linear problems such as those experienced during dynamic loading. In 2004, Bratianu et al. published a dynamic three dimensional full joint contact model for investigating the articular cartilage response under strain rate dependent loading conditions[65]. Solved using FE software packages, LS-DYNA and ANSYS by manually defining the joint in different positions determined from literature data, loading conditions simulated activities such as walking and jumping. Although, significant simplifications in the tissue geometries were made and the ligaments were omitted, this model proved the ability to model dynamic cases using FE.

Papaioannou et al. developed a method for studying meniscal behaviour, using a dynamic explicit full lower limb model which included the foot and distal femur[66].

Menisci were modelled as a transversely isotropic material and AC as isotropic linear elastic. Bone kinematics for uniaxial loading at different strain rates were measured using biplane dynamic Roentgen stereogrammetric analysis and applied to the model. Soft tissue kinematics measured using tantalum beads embedded in the cadaveric specimen was used for validation of the FE model. In this model, only compression loading was investigated and no information was provided regarding ligaments modelled. However, the importance of accurate menisci geometry and kinematic descriptions were reconfirmed, agreeing with previous research by Haut Donahue et al.

A subject-specific FE model of the knee to study the effects of frontal plane tibiofemoral angle variation was published in 2010[67]. Subject-specific geometries were obtained from a short bore 1.5 Telsa MR imaging facility. A fat suppressed fast spin echo sequence was used to obtain sagittal plane images of the knee with slice thickness of 2mm. The images were segmented and the solid model exported into FE software, ABAQUS. Cartilage was modelled as isotropic linear elastic and the meniscus as transversely isotropic linear elastic. The model also included the ACL, PCL, LCL and MCL with material properties taken from the literature.

Patient-specific loading conditions were measured using motion capture and force plates and inverse dynamics analysis was performed to determine joint reactions and muscle forces. The resultant joint loading conditions were applied to the FE model via definition of the forces and moments acting about the AP and the SI axes. Loading in the flexion-extension rotational DOF was defined using an angular velocity. This method of modelling knee joint mechanics during full gait cycles was also employed in the model developed by Taiyuan University of Technology[68]. This method of defining patient specific loading conditions is in-line with the techniques proposed for the HTO project and will therefore be of reference for this project.

2.2.1 Segmentation algorithms

MR image data of the knee region is too complex for the use of a completely automated segmentation algorithm. This is due to multiple tissues within the knee sharing similar greyscale values, as well as, variation of greyscale values within the same tissue that reflect the inhomogeneous material composition of natural biological tissues[69]. Semi-automated segmentation algorithms such as, random walks, where the algorithm can segment the boundary of a tissue in 2D or 3D based on seeds placed by the user has been applied to medial images of the brain, heart and lungs[70]. However, adjacent structures of similar material properties are often found in the knee, i.e. between the femoral-tibial AC and the patella-femoral AC. Therefore, the application of boundary detection semi-automated segmentation will not be possible. Thus, in MR imaging scan data, tissues of the knee have to be manually segmented.

Manual segmentation can demand significant human effort. The operator is required to select each individual voxel that is believed to belong to a certain tissue for every slice. Furthermore, manual selection can be subjected to significant inter- and intra- operator variability. Thereby, introducing errors in the final segmented volume. To reduce errors introduced during the segmentation process, assistive algorithms such as threshold paint, floodfill and confidence connected region growing have been implemented in ScanIP, Simpleware Ltd.

Floodfill is an algorithm where the boundary of a tissue is first pre-defined manually by the user. The algorithm then automatically selects all the voxels enclosed by the boundary. Thus, the operator must be careful to ensure there are no gaps in the boundaries. As with manual segmentation, the operator is still required to select the individual voxels in every sagittal slice to create the boundary.

The idea of the confidence connected region growing algorithm is to only select voxels with similar greyscale values that are connected to the initial region, called

the seed. The algorithm calculates the mean and standard deviation of the seed and determines the upper and lower bounds of greyscale values to include.

Say there is currently m number of voxels selected with greyscale values, $\psi_1, \psi_2, \dots, \psi_m$. If we let the greyscale value mean, ψ_{mean}, and standard deviation, $\psi_{s.d.}$, of all the currently selected voxels be,

$$\psi_{mean} = \frac{1}{m} \sum_{i=1}^{m} \psi_i \quad (2.9)$$

$$\psi_{s.d.} = \sqrt{\frac{1}{m} \sum_{i=1}^{m} (\psi_i - \psi_{mean})^2} \quad (2.10)$$

Then the new upper and lower bounds for the greyscale value range to be selected can be calculated using equation 2.11[71], where ζ is the region growing multiplier, an arbitrary constant chosen by the operator.

$$\begin{aligned} \psi_{upper}^{n} &= \psi_{mean} + \zeta \psi_{s.d.} \\ \psi_{lower}^{n} &= \psi_{mean} - \zeta \psi_{s.d.} \end{aligned} \quad (2.11)$$

The algorithm automatically selects all neighbouring voxels within the newly defined greyscale value range and recalculates the mean and standard deviation for the updated segmented volume. The iterative process is repeated according to the number of iterations defined by the operator. The advantage of such a semi-automated algorithm is that operator effort can be greatly reduced. For image scan data with clear distinct boundaries between adjacent tissues with high greyscale contrast, segmentation could be near fully automated. However, on image scan data where the boundaries between adjacent tissues are less distinctive, the algorithm may proof less useful. The effectiveness of this semi-automatic segmentation algorithm is also greatly dependent on the operator's ability in choosing a correct value for the region growing multiplier.

Threshold painting can be used to assist the accurate delineation of tissue boundaries. The tool, paint with threshold, requires the operator to select the

threshold of greyscale values, which are believed to belong to a particular tissue. As with manual segmentation, the operator is required to select voxels. Although different to manual segmentation, only voxels with greyscale values within the upper and lower bounds are selectable. Compared to region growing, this algorithm has greater demands on operator effort and is more prone to operator subjectivity. However, it is useful in image scan data that consist of many adjacent tissues with less distinctive boundaries.

2.2.2 Meshing of the full joint contact Finite Element model

The full joint contact FE models discussed were meshed using first order hexahedral element[54 58 62 65 66] and mixed pentahedral and hexahedral elements[64]. Pure hexahedral meshes generated from medial images are typically voxel based and require significant manual manipulation. Automated mixed hexahedral and tetrahedral mesh meshing algorithm require a surface model to be reconstructed for the segmented volume. These surface models are then meshed using a contour-based meshing algorithm[72]. Developments in voxel-based meshing algorithms have made automated tetrahedral mesh generation for segmented geometries a possibility[73]. Tetrahedral elements are increasingly being recognised as a good choice for meshing irregular geometries common in biomedical applications[74]. Though quadratic tetrahedral elements have been known to perform poorly in contact problems. And as a result, mixed hexahedral and tetrahedral meshes with hexahedral elements assigned in areas of possible contact have been used. In ABAQUS improved tetrahedral elements where stresses are directly calculated on the surface and not extrapolated are now available, these are called enhanced quadratic tetrahedral elements (C3D10I) [75]. An example of a tetrahedral meshed contact model, is the full joint contact knee model published in 2012[76].

Simpleware® is an image processing software with improved voxel-marching cube based hybrid meshing capabilities[77]. Employing image processing techniques, the

meshing algorithm is able to produce multipart volumetric meshes with smooth outer contours and interfaces with excellent conformity[78]. In addition, the software also has built-in tools for generating ABAQUS input script files for direct transfer of the meshed geometry into the FE package, ABAQUS.

2.3 Digital image correlation for surface topology measurement

Digital Image Correlation (DIC) is a non-contact high-resolution optical technique typically used for capturing strain measurements[79 80]. Although less common, the technology can also be used for surface contour measurements. Using a single camera, 2D-DIC setup to measure the surface contour of a conical surface of diameter 100mm and height 30mm, the accuracy was found to be within 0.05mm[81]. Measurement of a 73mm diameter sphere using a 3D-DIC system (DANTEC, Dynamics) with 1M pixels cameras showed an accuracy of 0.28μm[82].

In 3D-DIC, the method relies on a synchronised multiple cameras set up (a minimum of two) to image the object of interest from multiple angles. This typically involves two cameras mounted at a distance apart on a rigid beam supported by a tripod. This allows ease of manipulation of the camera angles, height and horizontal translation. Additional light source is added as required and can been seen mounted in between the two cameras in Figure 2.8.

A calibration target with a known uniform pattern is used for determining unknown system parameters. Images of the calibration target are taken in a variety of location and orientations within the field of view of the cameras. By determining the unknown system parameters, a mapping function can then be computed for the calculation of contour coordinates.

A unique random speckle pattern on the surface of the object must be prepared, as the analytical software relies on tracking subsets of the grey value pattern. Image

registration between the multi-angle images is then performed for calculation of the three-dimensional coordinates[83].

Figure 2.8 A typical 3D-DIC stereo-vision system setup[84]

Various factors can influence the accuracy of this measurement technique, these include; Camera resolution, size of the object of interest, distance between the camera and object, focal length of the lens used, lighting and the quality of the speckle pattern applied[85].

2.4 Conclusions

There are currently a wide range of validated full joint contact FE models available in the literature. However, none of these models have been designed and are not suitable for generating patient specific finite element models for the purpose of this study on a cohort of patients. The objectives for addressing the aims of this project are revised here in relation to the findings from the literature review.

2.4.1 Aim One: FE-gene expression proof of concept

In order to predict strains experienced by the chondrocytes in AC, accurate prediction of stresses and strains at the ECM level is important. There are currently

a range of constitutive models available for modelling the mechanical behaviour of AC. However, the explants geometries in these modelled are perfect axis-symmetric cylinder with flat top and bottom surfaces. Previous research has noted the natural surface curvature of the explants and the possible discrepancy between FE predictions and experimental results. To overcome this problem, the surfaces of the explants are cut using a microtome until a flat surface is achieved. This is not possible for explants to be used in gene expression studies. No study has been carried out previously to quantify the error introduced in FE predictions due to the surface curvature simplifications. Therefore, the newly defined objectives to address this aim are:

- Investigate the effects of surface curvature on FE predictions
- Establish a protocol using 3D-DIC for extracting the surface curvature of the explants

2.4.2 Aim Two: Reconstruction of patient specific tissue geometries

The first step in developing patient-specific FE knee models is to be able to incorporate geometries specific to an individual patient. There are currently a number of published full joint contact FE models of the knee based on geometries reconstructed from the real tissues using CT, stereogrammetric, coordinate measuring machine, as well as, MR imaging on cadavers[58 64 66]. Due to ethical restrictions, extraction of tissues for coordinate measuring and the use of radioactive CT or invasive stereogrammetric imaging are not possible for HTO patients at the centre. In line with current plan for the HTO project, imaging methods for patient specific geometries is restricted to MR imaging.

MR imaging resolution is dependent on the strength of the scanner and scan time. Clinical MR imaging scanners are typically 1.5T and those used for research are 3T. A MR imaging scanner of higher strength would be able to produce a set of scan data of higher resolution in the same amount of time. Or alternatively, it can be

said that a 3T MR imaging scanner can produce the same resolution scan as a 1.5T machine in a shorter time. Cadaveric specimens can be left in an MR imaging scanner to scan over night and produce scan data of high resolution with good signal to noise ratio (SNR). A good SNR is generally defined as the difference in signal intensity between the area of interest and the background. In a knee scan image, as there are multiple structures, SNR is defined as the difference in signal intensity between the areas of interest and their respective adjacent tissues. There is concern that in order to obtain MR imaging scan data with resolution sufficient for delineation and segmentation of the soft tissues, an unrealistic scan time for live patients would be required. However, Yao et al.[64] and Yang et al.[67] demonstrated in their study that segmentation of both soft and hard tissues from MR imaging scan data is possible for live patients. Though, scan image quality can vary greatly between scanners even with the same scan sequence and scan subject. It is therefore, not possible to directly employ scan sequences suggested in the literature. Optimal scan sequence for tissue delineation must be optimised for the scanner intended to be used in this research.

Segmentation of knee scan image data is notorious for being labour intensive and prone to operator subjectivity due to the number of adjacent tissue structures with similar material properties. The aim to develop patient specific FE knee models as a tool for studying the HTO cohort means that a large number of scan image data of the knee will require segmentation. There is, therefore, a great desire to establish methods for reducing operator effort and subjectivity. It is recognised that fully automated segmentation may not currently be possible, though the use of semi-automated tools is a possibility for exploration.

For the same motivations, automated meshing of these models is also desired. Due to the poor surface conformity of hexahedral elements and the labour intensive meshing processes, there is a great interest in the use of automated tetrahedral

meshing algorithms. The use of currently available commercial software, Simpleware, will be investigated.

Objectives identified for addressing this aim are:

- Verify a suitable MR imaging sequence for obtaining image scan data from live patients using the 3Tesla MR scanner at CUBRIC for tissue delineation
- Investigate suitable segmentation methods for reducing operator effort and subjectivity for segmentation of the tissue geometries
- Investigate the use of Simpleware meshing algorithms for automated tetrahedral meshing of the tissue geometries

2.4.3 Aim Three: MTL inclusions in full joint contact FE models

The knee is a complex structure involving many individual tissues with different mechanical properties working together with a vast range of variable factors. As recognised by Bergeron, it is impossible to include every detail of the real "in vivo" system in the model and certain assumptions and simplifications must be made[86]. The validity of these assumptions and simplifications can be examined by validation with experimental results or through the use of parametric and probabilistic modelling. Acceptable simplifications include the use of analytically rigid bones to reduce DOF, the use of linear elastic material properties for menisci and AC for cases with loading times much shorter than the viscoelastic time constant of 1500s[53] and the use of non linear spring elements to model ligaments; these have all been incorporated into the full joint contact knee models in this literature review to reduce DOFs.

Furthermore, an experimental cadaveric study measuring the mean contact pressure, peak contact pressure and change in contact area before and after IML dissection showed that the presence of the IML is mechanically insignificant[87]. However, studies have also highlighted aspects of the model inputs which

significantly affect the accuracy of the FE model predictions. This includes accurate description of the meniscal geometries, constraints and material properties. It was also found that restriction of internal-external and adduction-abduction rotations can cause profound errors in the prediction of knee kinematics. Material properties of the meniscus, meniscal horns, AMFL and PMFL can be obtained from literature. However, it was identified that there is a lack of knowledge with regards to the mechanical behaviour of MTLs and no material data for the tissue has been found in literature.

Objectives identified in the literature review for addressing this aim are:

- Develop a full joint contact FE knee model incorporating patient specific tissue geometries
- Explore the use of the dynamic explicit solver for future incorporation of loading data from musculoskeletal modelling
- Investigate the microstructure and mechanical behaviour of the MTLs
- Verify the method of representation of MTLs in the FE models

2.5 References

[1] M.V. Paterno and T.E. Hewett, 'Biomechanics of multi-ligaments knee injuries (MLKI) and effects on gait', North American Journal of Sports Physical Therapy, 3(4):234-241, 2008

[2] M.E. Eastlack, M.J. Axe, L. Snyder-Mackler, 'Laxity, instability, and functional outcome after ACL injury: copers versus noncopers', 31(2):210-5, 1999

[3] E. Wang, T. Nelson and R. Rauch, 'Back to elements –tetrahedral vs. hexahedral', Proceedings of 2004 International ANSYS Conference, May 24-26, Pittsburgh, PA, USA, 2004

[4] B.P. Bergeron and R.A. Greenes, 'Modeling and simulations in medicine: the state of the art', Symposium on Computer Applications in Medical Care, 1988

[5] National Cancer Institute. http://training.seer.cancer.gov/anatomy/body/terminology.html [Accessed 5th June 2013]

[6] E.S. Grood and W.J. Suntay, ' A joint coordinate system for the clinical description of three-dimensional motions: application to the knee', Journal of Biomechanical Engineering, 105:136-144, 1983

[7] Knee Arthroscopy, Health Pages. http://healthpages.org/surgical-care/knee-arthroscopy/ [Accessed 30th June 2013]

[8] K. Gelse, E. Pöschol and T. Aigner, 'Collagens –structure, function and biosynthesis', Advanced Drug Delivery Review, 55:1531-1546, 2003

[9] H. Lodish, A. Berk and S.L. Zipursky, 'Section 22.3 Collagen: The fibrous protein of the matrix', In Molecular cell biology, W.H. Freemon, New York, 2000

[10] J.A. Weiss and J.C. Gardiner, 'Computational modeling of ligament mechanics', Critical reviews in Biomedical Engineering, 29(3):303-371, 2001

[11] V.C. Mow, W.Y. Gu and F.H. Chen, 'Chapter 5: Structure and function of articular cartilage and meniscus', In Basic Orthopaedic Biomechanics & Mechano-biology (3rd ed.), Lippincott Williams and Wilkins, 181-258, 2005

[12]https://www2.imperial.ac.uk/earthscienceandengineering/rocklibrary/viewglossrecord.php?Term=cross%20polarised%20light [Accessed 21st September 2013]

[13] J.F. Ribeiro E.H. Martins dos Anjos, M.L.S. Mello and Benedicto de Campos Vidal, 'Skin collagen fiber molecular order: a patter of distributional fiber orientation as assessed by optical anisotropy and image analysis', PLoS One 8(1): e54724. doi:10.1371/journal.pone.0054724, 2013

[14] R. Bear, 'The structure of collagen fibrils', In Advances in Protein Chemistry Vol. 7, Academic Press Inc., New York, 69-150, 1952

[15] J.M. Mansour, 'Chatper 5: Biomechanics of cartilage', In Kinesiology: The mechanics and pathomechanics of human movements (Oastis, C.A. ed.), Lippincott Williams and Wilkins, Philadelphia, Ch.5, 66-79, 2003

[16] A.K. Jeffery, G.W. Blunn, C.W. Archer and G. Bentley, 'Three-dimensional collagen architecture in bovine articular cartilage', Journal of Bone & Joint Surgery [Br], 73-B:795-801, 1991

[17] J.A. Buckwalter, V.C. Mow and A. Ratcliffe, 'Restoration of injured or degenerated articular cartilage', 2(4):192-201, 1994

[18] I. Redler, V.C. Mow, M.L. Zimny and J. Mansell, 'The ultrastructure and biomechanical significance of the tidemark of articular cartilage', Clinical Orthopedic Related Research, 112:357-362, 1975

[19] F. Guilak and V.C. Mow, 'The mechanical environment of the chondrocyte: a biphasic finite element model of cell-matrix interactions in articular cartilage', Journal of Biomechanics, 33(12):1663-1673, 2000

[20] N.O. Chahine, C.T. Hung and G.A. Ateshian, 'In-situ measurements of chondrocyte deformation under transient loading', European Cells and Materials, 13:100-111, 2007

[21] L.G. Alexopoulos, L.A. Setton and F. Guilak, 'The biomechanical role of the chondrocyte pericellular matrix in articular cartilage', Acta Biomaterialia, 1(3):317-326, 2005

[22] D.R. Carter, G.S. Beaupré, M.Wong, R.L. Smith, T.P. Andriacchi and D.J. Schurman, 'The mechanobiology of articular cartilage development and degeneration', Clinical Orthopaedics and Related Research, 427S:S69-77, 2004

[23] J.B. Fitzgerald, M. Jin, D. Dean, D.J. Wood, M.H. Zheng and A.J. Grodzinsky, 'Mechanical compression of cartilage explants induces multiple time-dependent gene expression patterns and involves intracellular calcium and cyclic AMP', J Biol Chem, 279:19502-19511, 2004

[24] A.J. Grodzinsky, M.E. Levenston, M. Jin and E.H. Frank, 'Cartilage tissue remodelling in response to mechanical forces', Ann Rev Biomed Eng, 2:691-714, 2000

[25] T.M. Quinn, A.J. Grodzinsky, M.D. Buschmann, Y-J Kim and E.B. Hunziker, 'Mechanical compression alters proteoglycan matrix assembly around individual cells in cartilage explants', J Cell Sci, 111:573-583, 1998

[26] R.S. Thomas, A.R. Clarke, V.C. Duance and E.J. Blain, 'Effects of Wnt3A and mechanical load on cartilage chondrocyte homeostasis', Arthritis Research and Therapy, 3:R203, 2011

[27] M. Wong, M. Siegrist and X. Cao, 'Cyclic compression of articular cartilage explants in associated with progressive consolidation and altered expression pattern of extracellular matrix proteins', Matrix Biology, 18:391-399, 1999

[28] A.C. Hall, E.R. Horwitz and R.J. Wilkins, 'Physiological society symposium: ion transport in health and disease. The cellular physiology of articular cartilage', Experimental physiology, 81:535-545, 1996

[29] L.P. Li, W. Herzog, R.K. Korhonen and J.S. Jurvelin, 'The role of viscoelasticity of collagen fibers in articular cartilage: axial tension versus compression', Medical Engineering and Physics, 27(1): 51-57, 2005

[30] A. Maroudas and M. Venn, 'Chemical composition and swelling of normal and osteoarthritic femoral head cartilage', Annals of the Rheumatic Diseases, 36:399-406, 1977

[31] M.R. DiSilvestro, Q. Zhu, M. Wong, J.S. Jurvelin and J.-K. F. Suh, 'Biphasic poroviscoelastic simulation of the unconfined compression of articular cartilage: I –Simultaneous prediction of reaction force and lateral displacement', Journal of Biomechanical Engineering, 123:191-197, 2001

[32] W. Wilson, C.C. van Donkelaar and J.M. Huyghe, 'A comparison between mechano-electrochemical and biphasic swelling theories for soft hydrated tissues', Journal of Biomechanical Engineering, 127:158-165, 2005

[33] J.Z. Wu and W. Herzog, 'Simulating the swelling and deformation behaviour of soft tissues using a convective thermal analogy', BioMedical Engineering OnLine, 1:8, 2002

[34] W. Wilson, C.C. van Donkelaar, B. van Rietbergen and R. Huiskes, 'A fibril-reinforced poroviscoelastic swelling model for articular cartilage', Journal of Biomechanics, 38:1195-1204, 2005

[35] D.C. Fithian, M.A. Kelly and V.C. Mow, 'Material properties and structure-function relationship in the menisci', Clinical Orthopaedic Related Research, 252:19-31, 1990

[36] K. Bloecker, A. Guermazi, W. Wirth, O.Benichou, C.K. Kwoh, D.J. Hunter, M. Englund, H. Resch and F. Eckstein, 'Tibial coverage, meniscus position, size and damage in knees discordant for joint space narrowing –data from the Osteoarthritis Initiative', Osteoarthritis and Cartilage, 21(3):419-427, 2013

[37] C.S. Proctor, M.B. Schmidt, R.R. Whipple, M.A. Kelly and V.C. Mow, 'Material properties of the normal medial bovine meniscus', Journal of Orthopaedic Research, 7:771-782, 1989

[38] K. Messner and J. Gao, 'The menisci of the knee joint. Anatomical and functional characteristics, and a rationale for clinical treatment', Journal of Anatomy, 193:161-178, 1998

[39] P.G. Bullough, M. Munera, J. Murphy and A.M. Weinstein, 'The strength of the menisci of the knee as it relates to their fine structure', Journal of Bone and Joint Surgery [Br], 52:564-570, 1970

[40] A. Chevrier, M. Nelea, M.B. Hurtig, C.D. Hoemann and M.D. Buschmann, 'Meniscus structure in human, sheep, and rabbit for animal models of meniscus repair', Journal of Orthopaedic Research, 27:1197-1203, 2009

[41] F.N. Ghadially, J-M. A. Lalonde and J.H. Wedge, 'Ultrastructure of normal and torn menisci of the human knee joint', Journal of Anatomy, 136(4):773-791, 1983

[42] D.L. Skaggs, W.H. Warden and V.C. Mow, 'Radial tie fibers influence the tensile properties of the bovine medial meniscus', Journal of Orthopaedic Research, 12(2):176-185, 1994

[43] P.S. Walker and M.J. Erkman, ' The role of the menisci in force transmission across the knee', Clinical Orthopaedic Related Research, 109:184-192, 1975

[44] J.A. Dodds and S.P. Arnoczky, 'Chapter2: Meniscus', In Practical Orthopaedic Sports Medicine & Arthroscopy (1st Edition),Lippincott Williams and Wilkins, Philadelphia, 2007

[45] P.H. Abrahams, R.T. Hutchings and S.C. Marks Jr., 'McMinn's color atlas of human anatomy 4th edition', London:Mosby, 1998, Print

[46] D.I. Bylski-Austrow, M.J. Ciarelli, D.C. Kayner, L.S. Matthews and S.A. Goldstein, 'Displacements of the menisci under joint load: an in vitro study in human knees', J Biomechanics, 27(4):421-431, 1994

[47] F. Liu, B. Yue, H.R. Gadikota, M. Kozanek, W. Liu, T.J. Gill, H.E. Rubash and G. Li, 'Morphology of the medial collateral ligament of the knee', Journal of Orthopaedic Surgery and Research, 5:69, 2010

[48] O.C. Brantigan and A.F. Voshell, 'The tibia collateral ligament: its function, its bursae, and its relation to the medial meniscus', The Journal of Bone and Joint Surgery, 25(1): 121-131, 1943

[49] R.F. LaPrade, A.H. Engebretsen, T.V. Ly, S. Johansen, F.A. Wentorf and L. Engebresten, 'The anatomy of the medial part of the knee', Journal of Bone and Joint Surgery, 89:2000-2010, 2007

[50] T. Brindle, J. Nyland and D.L. Johnson, 'The meniscus: review of basic principles with application to surgery and rehabilitation', J Athl Train, 36(2): 160-169, 2001

[51] F.S. Bezerra, J.N. Alves, M.A.S. Silva, E.T.L. Trajano, T.A. Ferreira, H.A. Vasconcellos and S.S. Valença, 'Quantitative and descriptive analysis of the meniscotibial ligament in human corpses', Brazilian Journal of Morphological Sciences, 24(4): 211-213, 2007

[52] R. Crowninshield, M.H. Pope and R.J. Johnson, 'An analytical model of the knee', Journal of Biomechanics, 9:397-405, 1976

[53] J.D. Feikes, D.R. Wilson and J.J. O'Connor, '3-D Specimen-specific geometric modelling of the knee', Computer methods in Biomechanics and Biomedical Engineering, London: Gordon & Breach, 43-50, 1997, Print

[54] H-B. Schmiedmayer, P. Lugner and T. Gaudernak, 'A mathematical model of human joints including menisci', Computer Methods in Biomechanics and Biomedical Engineering, London: Gordon & Breach, 251-260, 1997, Print

[55] G. Li, J. Gil, A. Kanamori and S. L-Y. Woo, 'A validated three-dimensional computational model of a human knee joint', Journal of Biomechanical Engineering, 121:657-662, 1999

[56] T.L. Haut Donahue, M.L. Hull, M.M. Rashid and C.R. Jacobs, 'A finite element model of the human knee joint for the study of tibio-femoral contact', Journal of Biomechanical Engineering, 124:273-280, 2002

[57] T.L. Haut Donahue, M.L. Hull, M.M. Rashid and C.R. Jacobs, 'How the stiffness of meniscal attachments and meniscal material properties affect tibio-femoral contact pressure computed using a validated finite element model of the human knee joint', Journal of Biomechanics, 36:19-34, 2003

[58] T.L Haut Donahue, M.L. Hull, M.M. Rashid and C.R. Jacobs, 'The sensitivity of tibiofemoral contact pressure to the size and shape of the lateral and medial meniscus', Journal of Orthopaedic Research, 22:807-814, 2004

[59] J.R. Meakin, N.G. Shrive, C.B. Frank and D.A. Hart, ' Finite element analysis of the meniscus: the influence of geometry and material properties on its behaviour', The Knee, 10:33-41, 2003

[60] A. Jilani, A. Shirazi-Adl and M.Z. Bendjaballah, 'Biomechanics of human tibio-femoral joint in axial rotation', The Knee, 4:203-213, 1997

[61] K.E. Moglo and A. Shirazi-Adl, 'On the coupling between anterior and posterior cruciate ligaments, and knee joint response under anterior femoral drawer in flexion: a finite element study', Clinical Biomechanics, 18:751-759, 2003

[62] E. Peña, B. Calvo, M.A. Martínez and M.Doblaré, ' A three-dimensional finite element analysis of the combined behaviour of ligaments and menisci in the healthy human knee joint', Journal of Biomechanics, 39: 1686-1701, 2006

[63] E. Peña, B. Calvo, M.A. Martínez, D. Palanca and M.Doblaré, 'Finite element analysis of the effect of meniscal tears and meniscectomies on human knee biomechanics', Clinical biomechanics, 20:498-507, 2005

[64] J. Yao, J. Snibbe, M. Maloney and A.L. Lerner, 'Stresses and strains in the medial meniscus of an ACL deficient knee under anterior loading: a finite element analysis with image-based experimental validation', Journal of Biomechanical Engineering, 128:135-141, 2006

[65] C. Bratianu, P. Rinderu and L. Gruionu, 'A 3D Finite element model of a knee for joint contact stress analysis during sport activities', Key Engineering Materials, 261-263:513-518, 2004

[66] G. Papaioannou, G. Nianios, C. Mitrogiannis, D. Fyhrie, S. Tashman and K.H. Yang, 'Patient-specific knee joint finite element model validation with high-accuracy kinematics from biplane dynamic Roentgen stereogrammetric analysis', Journal of Biomechanics, 41:2633-2638, 2008

[67] N. Yang, H. Nayeb-Hashemi, P.K. Canavan and A. Vaziri, 'Effect of front plane tibiofemoral angle on the stress and strain at the knee cartilage during the stance phase of gait', Journal of Orthopaedic Research, 28:1539-1547, 2010

[68] Y. Guo, X. Zhang and W. Chen, 'Three-dimensional finite element simulation of total knee joint in gait cycle', Acta Mechanica Solida Sinica, 22(4):347-351, 2009

[69] J. Hohe, S. Faber, R. Muehlbauer, M. Reiser, K.-H. Englmeier and F. Eckstein, 'Three-dimensional analysis and visualization of regional MR signal intensity distribution of articular cartilage', Medical Engineering and Physics, 24:219-227, 2002

[70] L. Grady, T. Schiwietz, S. Aharon and R. Westermann, 'Random walks for interactive organ segmentation in two and three dimensions: implementation and validation', Medical Image Computing & Computer Assisted Intervention, 8(2):773-780, 2005

[71] Simpleware documentation (v5.0), Simpleware Ltd.

[72] M. Viceconti, L. Bellingeri, L. Cristofolini and A. Toni, 'A comparative study on different methods of automatic mesh generation of human femurs', Medical Engineering Physics, 20(1):1-10, 1998

[73] J. Kaminsky, T. Rodt, A. Gharabaghi, J. Forster, G. Brand and M. Samii, 'A universal algorithm for an improved finite element mesh generation Mesh quality assessment in comparison to former automated mesh-generators and an analytic model', Medical Engineering & Physics, 27:383-394, 2005

[74] A. Ramos and J.A. Simões, 'Tetrahedral versus hexahedral finite elements in numerical modelling of the proximal femur', Medical Engineering and Physics, 28(9):916-924, 2006

[75] S.C. Tadepalli, A. Erdemir and P.R. Cavanagh, 'Comparison of hexahedral and tetrahedral elements in finite element analysis of the foot and footware', Journal of Biomechanics, 44(12):2237-2243, 2011

[76] S.J. Abbass, F.M.R. Abdulateef, 'Finite element analysis of human and artificial articular cartilage', Journal of Engineering, 18(4), 2012

[77] P.G. Young, T.B.H. Beresford-West, S.R.L. Coward, B. Notarberardino, B. Walker and A. Abdul-Aziz, 'An efficient approach to converting three-dimensional image data into highly accurate computational models', Philosophical transactions of the Royal Society A, 366:3155-3173, 2008

[78] P. Young, G. Tabor, T. Collins, J. Richterova, E. Dejuniat and T. Beresford-West, 'Automating the generation of 3D finite element models based on medical imaging data', SAE Paper: 06DHM-51, 2005

[79] Moerman K.M., Holt C.A., Evans S.L. and Simms C.K., 'Digital image correlation and finite element modelling as a method to determine mechanical properties of human soft tissue in vivo', Journal of Biomechanics 2009; 42: 1150-1153

[80] Chu T.C., Ranson W.F. and Sutton M.A., 'Applications of digital-image-correlation techniques to experimental mechanics', Experimental Mechanics 1985; 25(3):232-244

[81] S.R. McNeil, M.A. Sutton, Z. Miao and J. Ma, 'Measurement of surface profile using digital image correlation', Experimental Mechanics, 37(1):13-18, 1996

[82] T. Becker, K. Spliffhof, T. Siebert and P. Kletting, 'Error estimations of 3D digital image correlation measurements', Technical Note, DANTEC Dynamics, http://www.dantecdynamics.com/docs/products-and-services/dic/T-Q-400-Accuracy-3DCORR-003-EN.pdf [Accessed 5th April 2014]

[83] Limess, Germany, http://limess.com/index.php/en/products/digital-image-correlation , [Accessed 9th February 2012]

[84] M.A. Sutton, 'Computer vision based, non-contacting deformation and shape measurements: a revolution in progress', Journal of the South Carolina Academy of Science, 11(1):11-17, 2013

[85] J.B. Kwak, 'DIC Methods for small scale measurements', MSc Thesis, Binghamton University, 2008

[86] B.P. Bergeron, R.A. Greenes, 'Modelling and simulation in medicine: the state of the art', Proceedings of the Annual Symposium on Computer Application, 9:282-286, 1988

[87] S-Y. Poh, K-S. A. Yew, P-L. K. Wong, S-B. J. Koh, S-L. Chia, S. Fook-Chong, T-S. Howe, 'Role of the anterior intermeniscal ligament in tibiofemoral contact mechanics during axial loading', The Knee, 2011, doi:10.1016/j.knee.2010.12.008

Chapter 3 Explant-specific finite element models for gene expression studies

Gene expression studies have been used to analyse the effect of mechanical loading on the biological response of the tissue[4 5 6 7]. In these studies, cylindrical osteochondral explants were dissected from the condyles and subjected to different mechanical loading conditions. Loading conditions such as force applied and bulk tissue strain can be measured using load cells, loading platen displacement measurements and optical methods; due to intra and inter-patient variability of AC material properties and the complexity of the inhomogeneous tissue microstructure[1], simple uni-axial compression may induce additional unknown solid and fluid stresses and magnitudes of strain in the ECM, PCM and intracellular regions that are different to the bulk tissue measurements.

Finite element (FE) models have been used for predicting the local stresses and strains experienced in the chondrocytes[2]. Though the accuracy of these models depends on the accurate prediction of the bulk tissue behaviour. Constitutive models for the bulk tissue have strived to describe anisotropic[3], depth dependent[4], biphasic poroviscoelastic[5], fibril-reinforced[6], swelling[7 8 9] mechanical behaviour. Previous authors have recognised that changes in ECM composition and/or organisation, in particular the depth dependent collagen architecture could alter the stresses and strains experienced by the chondrocytes[10]. By the use of inverse finite element methods, the applications of these soft tissue constitutive models have also been extended for determining material parameters for AC[11 12]. Nonetheless, these models assume the AC explants are perfectly axis-symmetrical cylinders with flat top and bottom surfaces[13].

To eliminate possible discrepancies, the top surfaces of these extracted AC explants are sliced using a microtome to match the test material to the FE geometry[14]. Alternatively, an arbitrary displacement is applied until full contact between platen and explant is established during mechanical loading, then a further 5% strain pre-load is added[15]. Consequently, the use of both these methods fails to capture the characteristics of the top layer of the tissue and does not allow an accurate prediction of the stress distribution experienced in the explant.

The superficial layer comprising the uppermost 5-10% of AC is known to have the lowest compressive stiffness and can deform 25% more than the middle zone[15]. For human femoral head AC, aggregate modulus, $\mathrm{H_A}$, increases with depth from 1.16MPa on the surface to 7.75MPa in the deep zone[16] and the correlation can be expressed using equation (3.1), where z in microns (μm) is the depth.

$$\mathrm{H_A(z)} = 1.44\exp^{(0.0012\mathrm{z})} \qquad (3.1)$$

Study of the AC surface changed radically in 1968 with the discovery that the surface of the tissue is in fact uneven[17] and has a unique microstructure different to that of the deeper layers. On top of the tightly woven fibrillar structure in the superficial layer[18] are distinctive fibril bundles with diameters of 1 to 3 μm spaced approximately 10-50μm apart running parallel to the surface. The fibrils unwind at each end and spread into the tissue to anchor the bundle[19] (Figure 3.1).

Undulations and irregularities of three different orders of magnitude were identified and classified into: 1. Primary anatomical contours, 2. Secondary irregularities of about 0.4-0.5mm diameter, 3. Tertiary undulations approximately 20-30μm in diameter[20]. These tertiary undulations are formed by the fibril bundles found on the surface of AC and are crucial to the tribology of articulating joints.

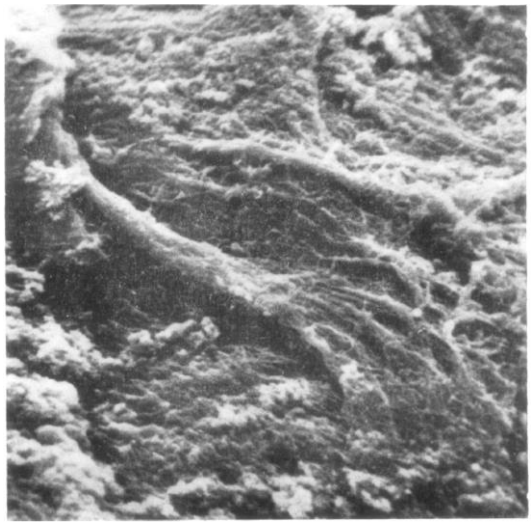

Figure 3.1 Larger diameter fibril bundles of 1-3µm found on the surface of AC[19].

They allow pools of synovial fluid to become trapped between the two surfaces, thereby creating a low friction elasto-hydrodynamic mechanism of lubrication[20]. Removal of the surface layer would therefore introduce false tribological characteristics, unrepresentative of the tissue behaviour *in vivo*.

In addition to affecting the tribology of AC, it has been demonstrated that cutting of the surface disrupts the CF architecture, diminishes the fluid retention ability of the tissue, as well as causes apoptosis of chondrocytes, which alters the biochemical, and consequentially, the material properties of the tissue. This further supports the need for preservation of the surface layer in AC tissue in order to capture its true *in vivo* mechanical behaviour.

It is hypothesised that the natural curvature of the AC tissue surface may affect the stress and strain distributions inside the tissue. As a result, true strains experienced by chondrocytes in uncut explants for gene expression studies will differ due to two factors: the surface geometry of the tissue and inhomogeneity of the microstructure. An in vitro study was carried out on human AC to investigate the effects of the natural tissue surface curvature on the stress and strain distributions. Explants for a gene expression study investigating the effects of physiological and

OA gait was used for possibility to explore correlations between the biological and FE results.

3.1 Materials and Methods

3.1.1 Experimental details of gene expression study on AC

3.1.1.1 Sample collection and preparation

A gene expression study was carried out internally (Metcalfe and Blain) to investigate biological difference in AC explants subjected to healthy and osteoarthritic gait loading patterns. Three excised human lateral femoral condyles were obtained from patients undergoing total knee replacement (TKR) surgery (aged 60-87), with ethical consent (approved by the Research Ethics Committee for Wales: 10/MRE09/28). All condyles had macroscopically intact AC with no evidence of injury at surgery. The femoral condyles were kept in Hank's Balanced Salt solution(HBSS) (Invitrogen, Paisley, Scotland) at 37^{o}C in a 5% CO_2 incubator until testing to ensure tissue remained biologically viable.

Dental putty (Soft Putty/ Regular Set, Dentsply, Addleston, UK) was used to take moulds of the surface geometry of the pre-extraction femoral condyles and post-extraction, after removal of 9mm diameter osteochondral explants, to mark their locations. Four explants were taken from each condyle reflecting the medial, lateral, posterior and anterior regions. The thickness of the cartilage layer for each sample was measured at the edge using vernier callipers. The thickness of cartilage was assumed to be uniform across the whole cross section and was further confirmed post mechanical loading, during processing of the tissue for gene expression studies.

3.1.1.2 Test set up

Mechanical loading was performed using a BOSE Electroforce 3200 (Bose Corporation, Minnesota, USA) testing machine with a 250N load cell controlled by BOSE Wintest 4.1 software. The test was carried out submerged in HBSS to ensure that the tissue did not become dehydrated, which could alter the biological and mechanical properties of the material. The explants were mounted on a tilting plate secured with a pin into the bone tissue. The explants were tilted so that the gap between the explant and the platen were equal all-round the edge.

Typical healthy ('physiological') and OA knee adduction moment waveforms were taken from motion analysis study[21] and applied to the explants as uni-axial compression loading waveforms. Strain controlled loading was found to be prone to separation issues between the explant and the loading platen. As a result, 30 pre-conditioning sinusoidal cycles were applied to the explants at the desired maximum strain to determine the force required. This force was taken to be the maximum force for the respective explants and used for scaling their individual force controlled cyclic load profiles.

Four different cyclic loading profiles were applied: 10% maximum strain (OA waveform), 15% maximum strain (OA waveform), 10% maximum strain (physiological waveform) and 15 % maximum strain (physiological waveform) (Figure 3.2). The four loading conditions were assigned using a random number generator to the four explants obtained from each condyle to ensure no dependency of the results on explant location. Loading cycles were applied at 1Hz, with 60% of the cycle under load and 40% of the cycle at rest for both waveforms. A residual load of 0.1N was used to ensure the platen remained in contact with the sample. Cyclic loading of 1800 cycles were applied whilst submerged to represent 30 minutes of normal walking. Experimental data from the first of the 1800 cycles were used for comparison with FE models.

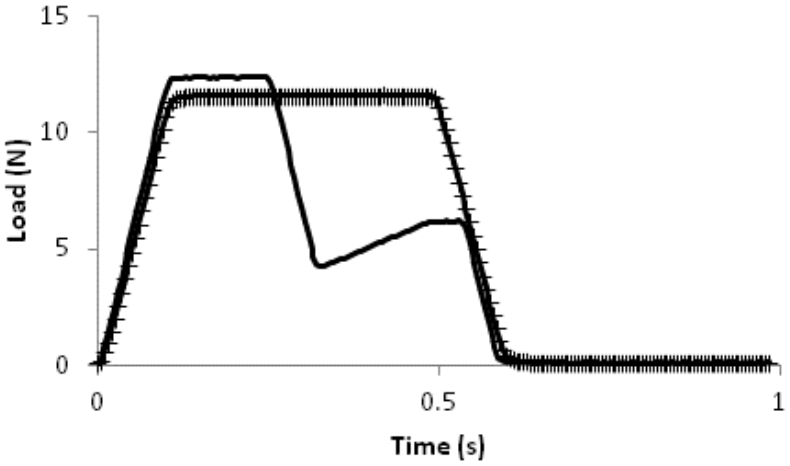

Figure 3.2 Example of the two load controlled waveforms applied. Solid line shows the physiological waveform and the hashed line is a typical osteoarthritic waveform.

3.1.2 Construction of the 3D explant specific surface geometry finite element models

3.1.2.1 Digital image correlation set up

Each femoral condyle had two corresponding putty moulds: one taken before explant extraction to record the original surface geometry of the condyle and one taken after explant extraction to record the locations of the explants dissected out of the condyle. Digital Image Correlation (DIC) was used to extract the condyle surface geometry from the dental putty moulds (Figure3.3).

The putty moulds were first sprayed uniformly with white paint. Random speckle patterns were then applied using black face paint by flicking bristles of a toothbrush. Speckles were approximately 3-5 pixels in size. The moulds were imaged using two 1M pixel cameras (Limess Messtechknik & Software GmbH, Pforzheim, Germany) with lenses of 28mm focal length, model XNP 2.0/28 (Messtechnik GmbH, Köln, Germany). Image acquisition software, Vic-Snap was used and three dimensional representations of the moulds were reconstructed using DIC analysis software, VIC-3D (Correlated Solutions Inc., Columbia, USA).

Camera aperture and shutter speed were adjusted for optimum image sharpness. Calibration of the system was done using a 9 x 9 target grid with 5mm spacing. Standard deviation of residuals was checked to be less than 0.02mm.

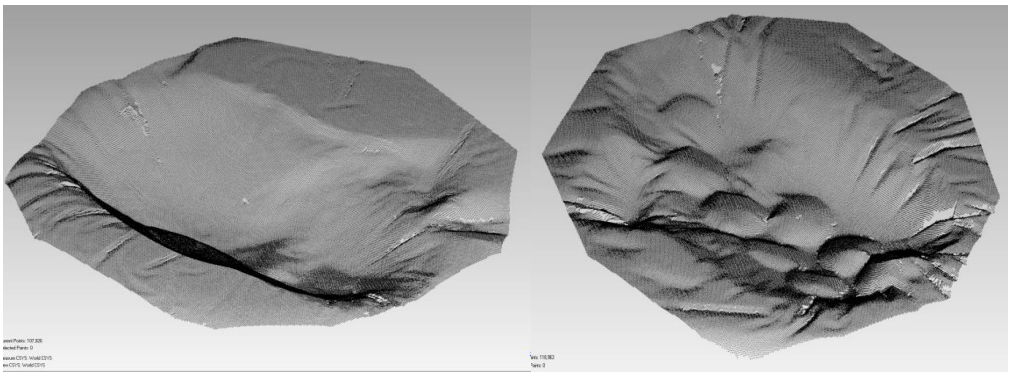

Figure 3.3 Point cloud data of the pre and post explant extraction moulds

3.1.2.2 Determination of explant locations

In order to create explant specific surface geometry models, information regarding the location of the explants must be mapped onto the pre-extraction mould to identify the relevant data points for each explant. Reference axis for the point cloud data for pre- and post- extraction moulds obtained from DIC point cloud data were different and, therefore three dimensional registration software was used to register the two sets of data together (Geomagic®, USA). Deviation in the coordinates between the two sets of data were calculated and plotted on the pre-explant extraction mould (Figure 3.4). Coordinates of a specified range of deviation value, for example, 1.8 <x< 2.1, were extracted for further processing to determine the centre coordinates of each explant (Figure 3.5).

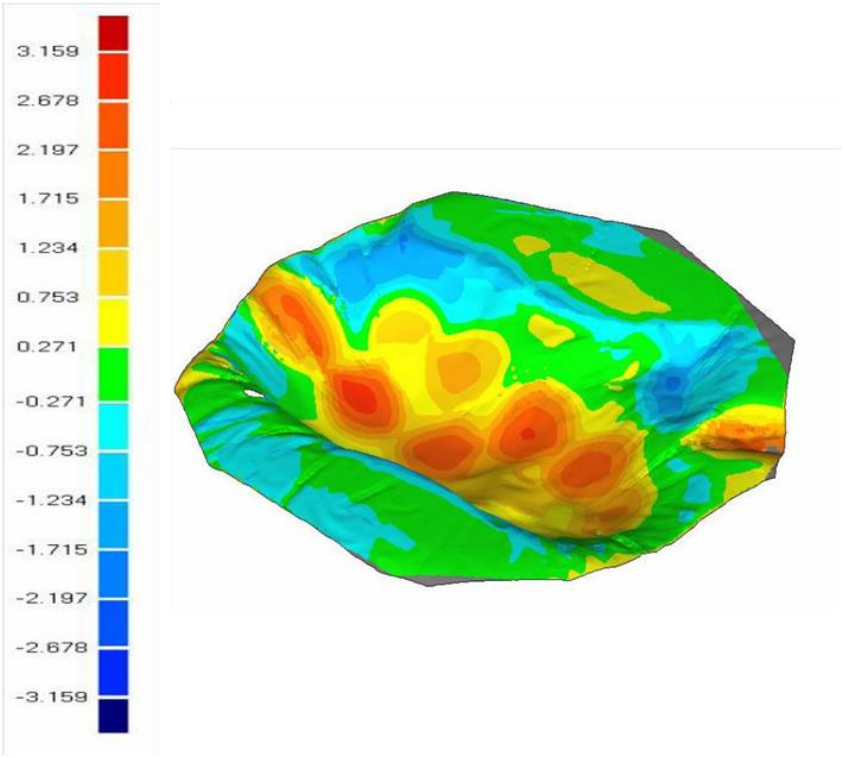

Figure 3.4 Contour plot of calculated vertical coordinate deviations between pre- and post-explant extraction moulds.

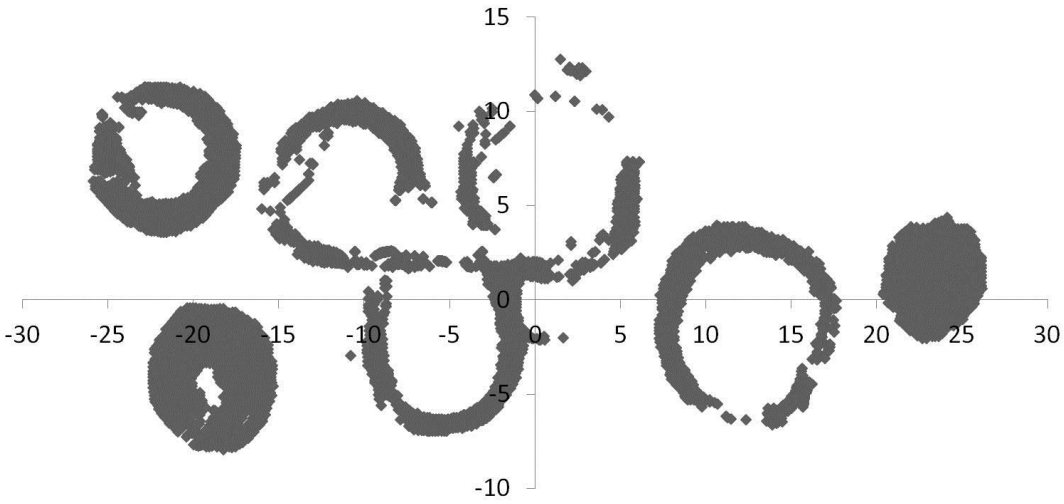

Figure 3.5 Data points extracted for determination of explant centre coordinates, 7 explant locations identified

3.1.2.3 Extraction of individual explant data points

Using an optimisation algorithm (MATLAB®, MathWorks, Inc.) to minimize the error between an ellipse of arbitrary major and minor radii and the data points, an ellipse was fitted to the data points of each individual explant identified and their centre coordinates calculated (Figure3.6). Point cloud data within the loci of the centre coordinates were then extracted for each individual explant to reconstruct their respective surface geometry. Each surface was represented by approximately 2100 data points, giving 33 data points/mm^2.

Point cloud data of the AC explants were used to create Non-uniform Rational B-spline (NURBS) surfaces (Geomagic®, USA). Assuming the thickness of the AC was uniform across the cross section, the NURBS surface was extruded to the measured thickness of the AC explants to create a solid model for meshing in FE software, ABAQUS (Simulia Corps., Dassault Systemes, USA).

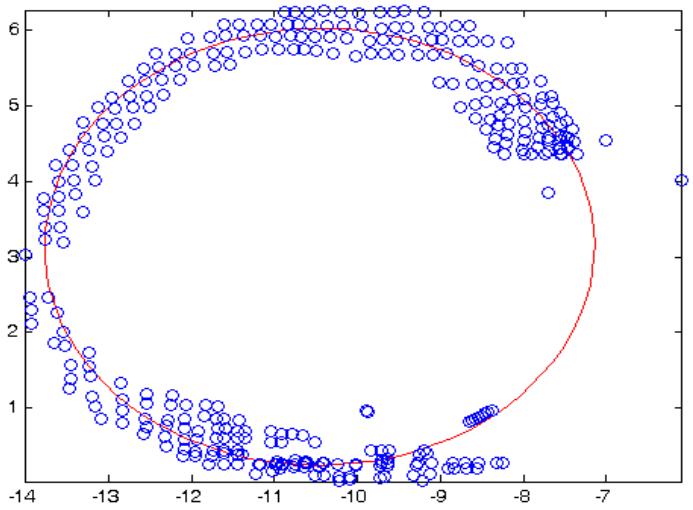

Figure 3.6 Filtered data points identified belonging to a particular explant. An ellipse was fitted to the data points for calculating the centre coordinates of the explant.

3.1.3 Finite Element Study 1: Comparison of axis-symmetric and explant specific finite element models

Compression of the explants by a rigid platen was modelled and solved using the quasi-static method. The explant specific finite element model was meshed with 29,140 quadractic tetrahedral elements with 67,400 nodes.

From the platen displacement data obtained from experiment, viscoelastic effects of AC were concluded to be insignificant over one load cycle which is 1s (Figure 3.7), and therefore the use of a linear elastic constitutive model would be sufficient. The AC was given realistic linear elastic properties, where Young's Modulus, E = 4.2MPa and Poisson's ratio, v = 0.46[22].

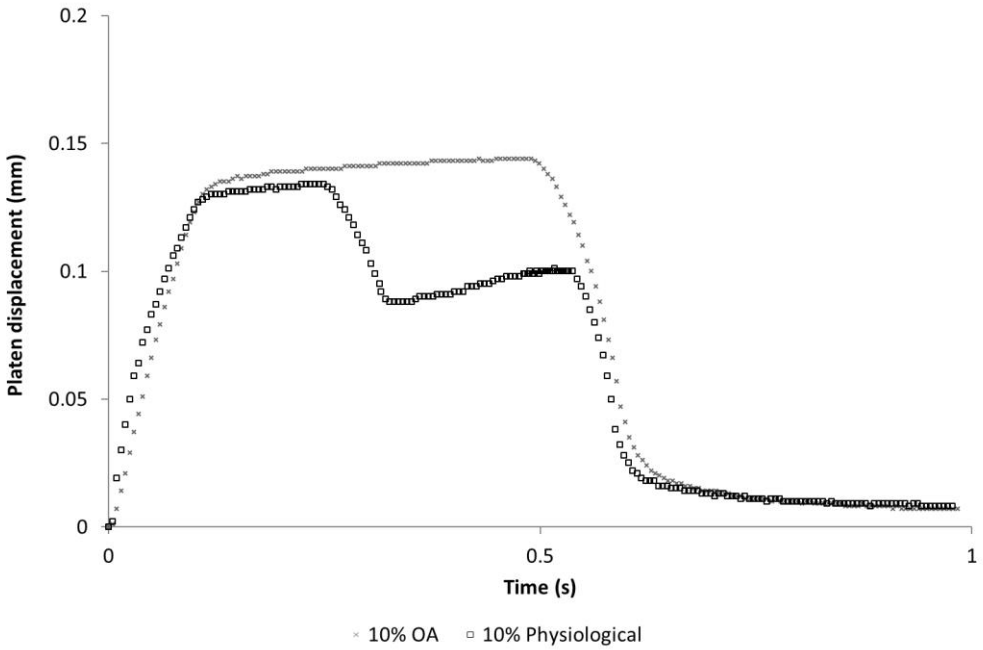

Figure 3.7 Platen displacement measured under OA and Physiological waveform load control

The 10% uni-axial strain equivalent load profile obtained from experimental data was applied over 0.1s, where maximum strain was held for 0.4s and unloaded with the same strain rate of 1/s. For the purpose of investigating possible errors in

stiffness calculation due to surface geometry, only the first cycle of the respective force controlled load profile obtained from the experimental data was applied.

All degrees of freedom (DOF) of the indenter were restricted, except in the axis parallel to the direction of the strain applied. It was assumed that the bone underlying the AC was significantly stiffer than the AC tissue. Therefore, all DOF of the bottom surface nodes were restricted. Interactions between the platen and the AC surface were modelled as hard normal contact with no penetration or separation after contact.

As mechanical loading of the explant was carried out submerged in fluid during the experiment and the surface of the AC was preserved, contact between the platen and tissue surface was assumed to be low friction elasto-hydrodynamic lubrication. Friction coefficient for a 9mm diameter AC explant under 5s of loading lubricated with synovial fluid is 0.01 and increases to 0.25 after 45 mins of loading[23]. In this study, only the first second is of interest and therefore, tangential contact was modelled as frictionless.

For comparison, respective axisymmetric cylindrical models with flat surfaces of the same thickness and diameter were analysed using identical material properties, boundary conditions and loading conditions (Figure 3.8).

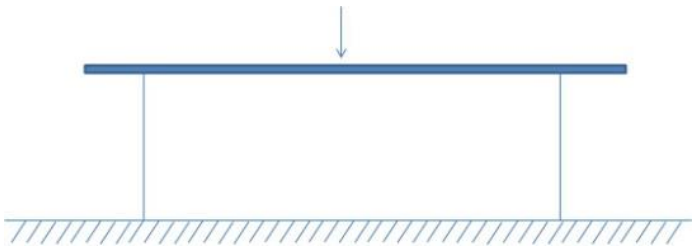

Figure 3.8 Diagram of the axis symmetric cylindrical models with flat surfaces. 10% strain was applied on the platen and the bottom surface of the explant was restricted in all DOFs.

3.1.3.1 Analytical model for validation of axis-symmetric FE model

For validation of the axis-symmetric FE model, the generalised Hooke's law in cylindrical polar coordinates (Equations 3.2-3.4) was used for calculating the maximum expected platen displacement.

$$e_\theta = \frac{[\sigma_\theta - \nu(\sigma_r + \sigma_z)]}{E} + \alpha_T \Delta T \quad (3.2)$$

$$e_r = \frac{[\sigma_r - \nu(\sigma_z + \sigma_\theta)]}{E} + \alpha_T \Delta T \quad (3.3)$$

$$e_z = \frac{[\sigma_z - \nu(\sigma_r + \sigma_\theta)]}{E} + \alpha_T \Delta T \quad (3.4)$$

Where, e_θ, e_r and e_z are the hoop, radial and axial strain respectively and σ_θ, σ_r and σ_z are the hoop, radial and axial stress. E is the young's modulus, ν is the poisson's ratio, α_T is the coefficient of linear thermal expansion and ΔT is the change in temperature.

For an unconfined compression case with no temperature change, where radial stress, σ_r and hoop stress, σ_θ are assumed to be zero, the stress-strain relationship in the axial direction is,

$$e_z = \sigma_Z / E \quad (3.5a)$$

For a confined compression case with no temperature change, where radial strain, e_r and hoop strain, e_θ, are assumed to be zero, the stress-strain relationship in the axial direction can described using equation 3.5b. Manipulation of equation 3.5b results in an expression for the aggregate modulus, H_A, equation 3.6.

$$e_Z = \frac{\left[\left(1 - \frac{2\nu(\nu+\nu^2)}{(1-\nu^2)}\right)\sigma_Z\right]}{E} \quad (3.5b)$$

$$H_A = \frac{\sigma_Z}{e_Z} = \frac{E(1-\nu)}{[(1+\nu)(1-2\nu)]} \quad (3.6)$$

3.1.4 Finite Element Study 2: Determining material properties using explant specific finite element models

Using the protocol detailed in section 3.1.2, a total of 12 explant specific finite element models were generated. Compression was applied using a platen modelled as a rigid body with a radius of 10mm to ensure it was larger than the explants and hence, no boundary effects from the platen could be induced. The explant model was rotated relative to the platen in the FE model and aligned in the same way as in the experiment.

An initial pre-loading step was used to establish contact between the platen and the surface of the AC explants. During this step, displacement controlled loading was applied until a reaction force of 0.1N was measured at the platen reference node, matching the experimental conditions of the mechanical test.

As the lateral displacement was not measured during the unconfined compression test, a specific value for both Young's modulus and Poisson's ratio cannot be determined using the inverse finite element method[24]. Therefore, Poisson's ratio was assumed to be 0.4, similar to values found in literature for linear elastic AC models [25 26], and the Young's modulus of each explant was optimised, by minimizing the error between maximum platen displacement from the experimental data and that predicted in FE. Predictions of the Young's modulus using the explant specific models were compared with their respective aggregate Young's modulus calculated from mechanical loading data, assuming a flat surfaced cylindrical geometry. The ratio of explant-specific FE model predicted stiffness and mechanical loading data calculated stiffness was termed α, stiffness correction factor.

The closeness of explant surface geometry to a flat surface was examined using a surface fitting tool (MATLAB®, MathWorks, Inc.). A flat surface expressed in the form of equation (3.7), was first fitted to the point cloud data of each explant.

$$f(x,y) = A + \mathrm{B}x + Cy \qquad (3.7)$$

The root mean squared error (RMSE) of the fit and coefficients were calculated, using Equation 3.8. Where N is the total number of data points, $\hat{y}_i$ is the vertical coordinate of the flat surface and y_i is the vertical coordinate of the curved surface.

$$RMSE = \sqrt{\frac{\sum_{i=1}^{N}(\hat{y}_i - y_i)^2}{N}} \qquad (3.8)$$

With coefficients B and C kept constant, A was optimised to eliminate negative residues, to ensure that the fitted plane did not intersect the explants surface and that the plane was tangential to the highest point of the surface (Figure 3.9).

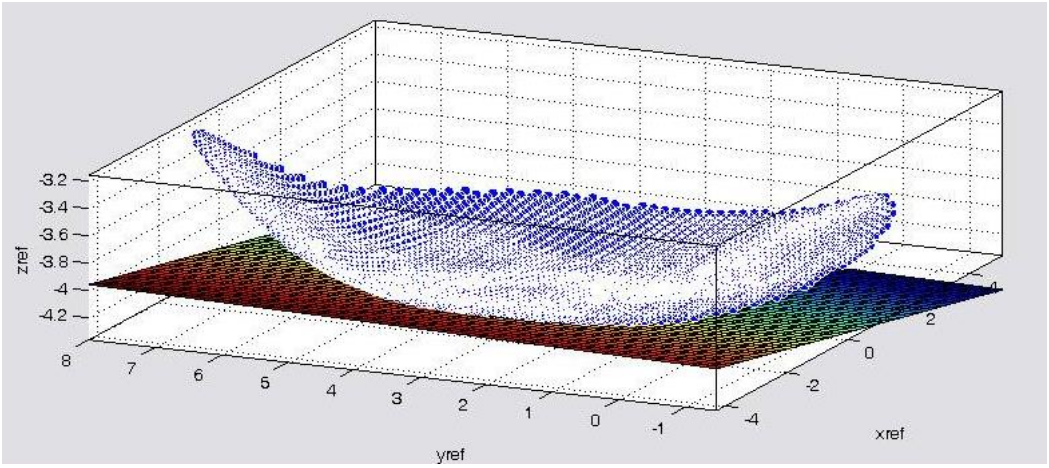

Figure 3.9 Plot of point cloud data and flat surface fitted using surface fitting tool. The flat surface representing the platen has been moved to ensure it is tangential to the highest point and does not intersect the explant surface.

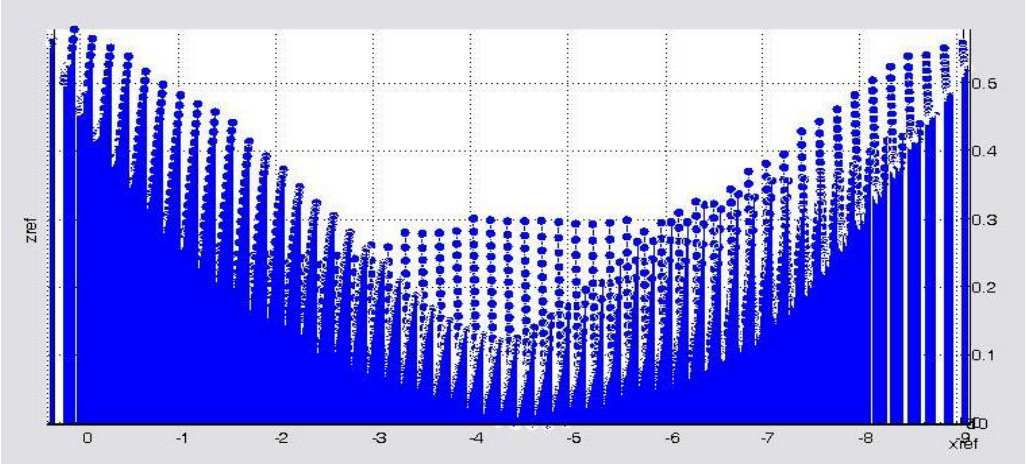

Figure 3.10 Residual plot for the flat surface fitted; used to ensure that the distance between the platen and both edges of the explant is approximately the same.

This allows the true discrepancy between the platen and AC surface to be calculated. The residual plot was also used to check opposite edges had approximately equal residuals, similar to that done during experimental testing (Figure 3.10). The sum of the squared errors, SSE, for each explant was obtained using equation 3.9 and divided by N, no. of data points for calculation of a factor which will be termed, surface flatness, β, using equation 3.10.

$$SSE = \sum_{i=1}^{n} (\hat{y}_i - y_i)^2 \qquad (3.9)$$

$$\beta = RMSE\ x\ \frac{SSE}{N} \qquad (3.10)$$

3.2 Results

3.2.1 Finite Element Study 1: Comparison of axisymmetric and explant specific finite element models

Comparison was carried out for one explant chosen randomly. For the explant specific model, maximum surface displacement at contact between the platen and explant was predicted to be 0.185mm and the maximum principal stress was

0.236MPa. Results for the flat surface model were found to be 0.047mm and 0.030MPa.

Using equation 3.5 and 3.6, the corresponding platen displacements for unconfined and confined compression is 0.0823 and 0.0178mm. Although the top surface of the axis-symmetric model is frictionless, which is an unconfined compression case, the nodes on the bottom surface is fully confined. Therefore, it is expected that the FE predicted platen displacement to be between the values calculated using the two analytical models, proving validity of the FE axis-symmetric model.

Deformation predicted by the axis-symmetric model displayed uniform transverse isotropy across the explants, as nodal displacement decreased linearly with depth from 0.047mm to 0mm. Maximum principal stress experienced across the tissue ranged from -0.0012MPa to 0.03MPa. There were no significant shear stresses predicted.

On the contrary, unique stress and strain patterns were predicted in the explant specific finite element model. Nodal displacements ranged from 0mm at the bottom of the AC to a maximum of 0.185mm experienced at the central region, the site where initial contact with the platen was at the beginning of loading (Figure 3.11). In addition to the depth wise variation, nodal displacement was predicted to decrease radially with the outer region experiencing significantly less displacement, approximately 0.03mm. Similarly, minimum principal stress distribution in the explant specific surface curvature model was found to vary in depth and transversely. The highest minimum principal stresses were predicted at the immediate region adjacent to the point where initial contact with the platen was established (Figure 3.12). Compared to the 0.0001MPa homogeneous shear stress predicted in the flat surface model, shear stresses of 0.15MPa were predicted in the explant specific model (Figure 3.13).

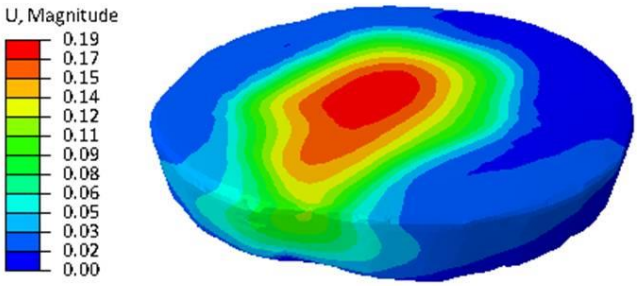

Figure 3.11 Contour plot of nodal displacement predicted for the explants-specific FE model

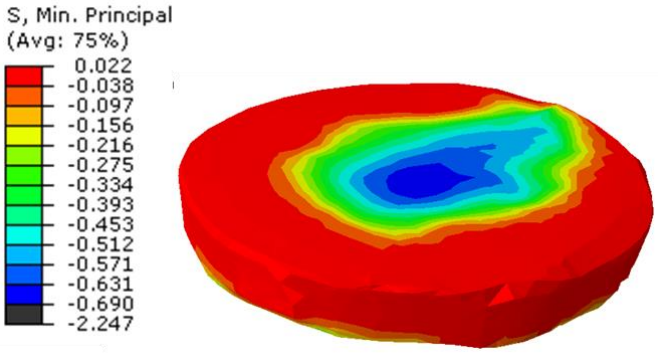

Figure 3.12 Contour plot of minimum principal stress predicted for the explant-specific model

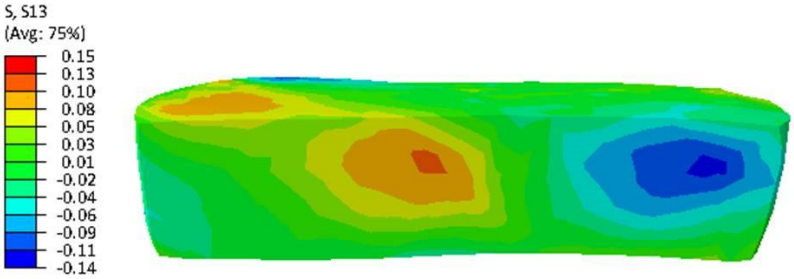

Figure 3.13 Contour plot of significant shear stress predicted in the explant-specific FE model

3.2.2 Finite Element Study 2: Determining material properties using explant specific finite element models

The thickness of the AC explants measured between 1.9-2.57mm and the instantaneous aggregate compressive modulus calculated from experimental data ranged from 1.41-5.51MPa (Table 3.1). Mean values of the explants for each

condyle were 1.99MPa, 3.36MPa and 4.28MPa. The instantaneous compressive modulus of individual AC explants determined using the explant specific models ranged between 2.06-12.87MPa, with mean values of 4.97MPa, 9.68MPa and 8.08MPa and standard deviations of 2.53, 2.93 and 2.74 respectively. Figure 3.14 shows the results of the inverse FE optimisation for platen displacement to determine the young's modulus for Sample 1A. A maximum compressive force of 11.58N was applied and the platen displacement predicted and measured was 0.15mm. This gave a prediction of 0.047 strain in the middle region of the explant (Figure 3.15). The thickness of the explant was 1.9mm and with the use of analytical methods, the strain calculated for the bulk tissue is 0.079. This proves the hypothesis that strains experienced inside the tissue is significantly different to that calculated for the bulk tissue.

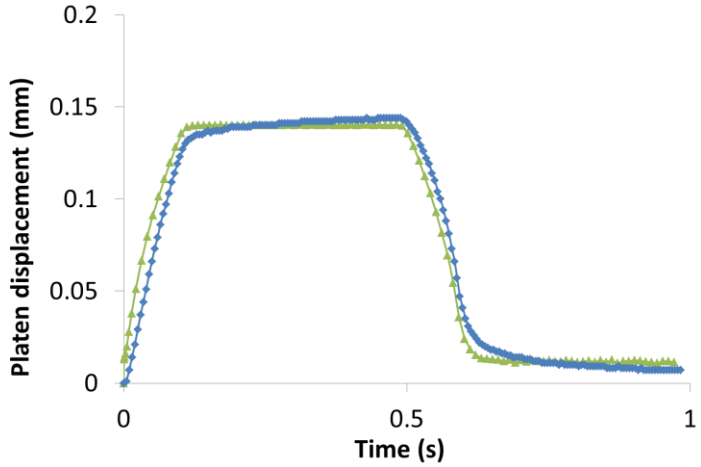

Figure 3.14 Optimisation fit between experimental and FE platen displacement for Sample 1A

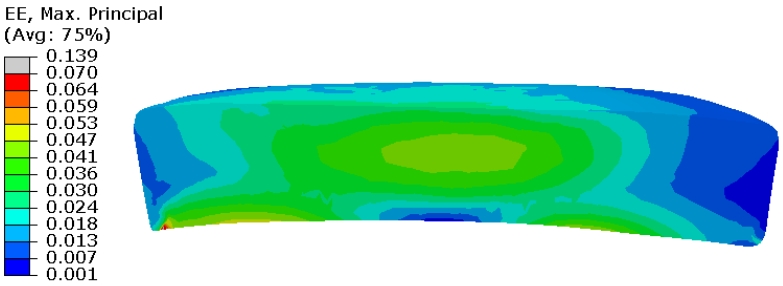

Figure 3.15 Contour plot of strain prediction in Sample 1A

Table 3.1 Thickness of explants, stiffness calculated from experimental data, finite element predicted stiffness and statistical analysis parameters of the surface geometries [locations: a =anterior, p=posterior, m=medial and l=lateral] Z, indicates those closest to the zenith.

Sample	Thickness (mm)	Location	Calculated Stiffness (MPa)	FE Stiffness (MPa)	RMSE	SSE
1A	1.9	AM	2.12	4.78	0.1365	0.06
1B	2.22	PM (Z)	2.84	8.23	0.1785	0.09
1C	2.04	PL	1.57	4.82	0.194	0.32
1D	2.02	AL	1.41	2.06	0.201	0.13
2A	2.41	AM (Z)	4.74	12.87	0.183	0.11
2B	2.56	AL	2.52	8.93	0.26	0.17
2C	2.62	PL	1.55	6.01	0.4235	0.70
2D	2.54	PM	4.64	10.89	0.2275	0.21
3A	2.26	AL	4.97	9.24	0.114	0.05
3B	2.15	AM (Z)	5.51	9.84	0.1821	0.12
3C	2.43	PL	2.53	3.98	0.09901	0.03
3D	2.57	PM	4.09	9.26	0.1319	0.08

Contour plots of vertical nodal displacement, vertical stress component and shear stress predicted at mid-diameter are presented for each individual explant (Figure 3.18-20). Similar stress and strain patterns were predicted for the different explants and are summarised in Figure 3.16. Maximum vertical nodal displacement was always predicted at the point of initial contact and decreased radially with no displacement at the bottom surface, as a zero displacement boundary condition was applied. A similar vertical stress component contour plot pattern was observed with maximum compressive stress values of 0.39-2.7MPa.

The minimum principal stress pattern typically had a distinctive middle column under compressive stress and the outer perimeter in tension of comparatively smaller magnitude. Maximum values of 0.6-2MPa were predicted in the central surface and bottom region with magnitudes decreasing in between. Average stress predicted in the intermediate zone of the middle column was 0.2-0.3MPa. The

width of the middle column varied between samples depending on the surface topology of the explant.

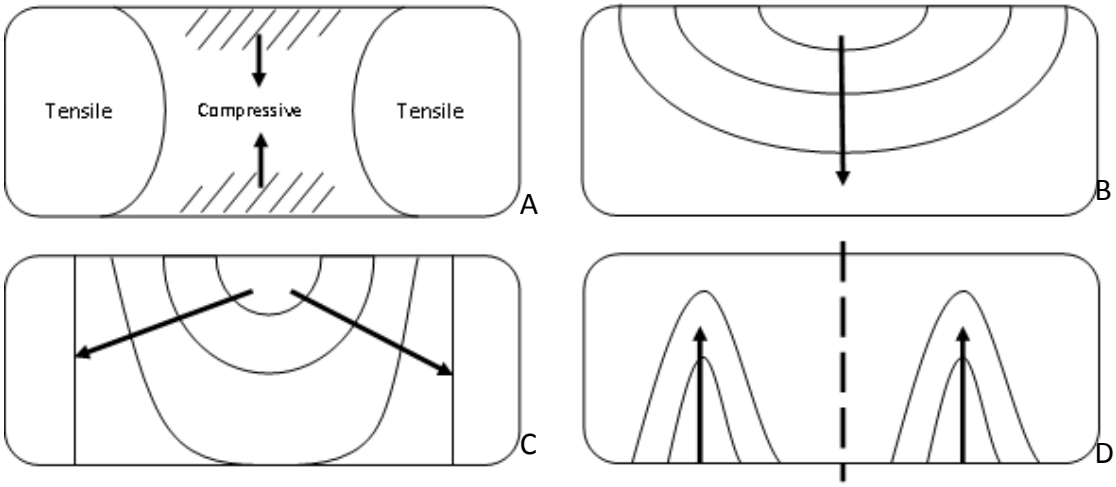

Figure 3.16 Typical stress and strain patterns observed in the mid cross section contour plots of the explant specific FE models. A: Minimum principal stress contour plot pattern. The middle column under compressive stress and the outer perimeter in tension of comparatively smaller magnitude; maximum values were predicted in the shaded regions and the arrows indicate the direction of diminishing stress. B: Vertical nodal displacement contour plot pattern with maximum predicted at the surface contact point. Arrow indicates direction of diminishing nodal displacements predicted with zero values at the bottom surface. C: Vertical compressive stress component contour plot pattern with maximum stress predicted at the point of contact. Arrow indicates direction of diminishing stress values. D: Shear stress contour plot pattern which has been observed to reflect about an axis projected perpendicular from the surface at the point of initial contact. Arrow indicates the direction of diminishing shear stress.

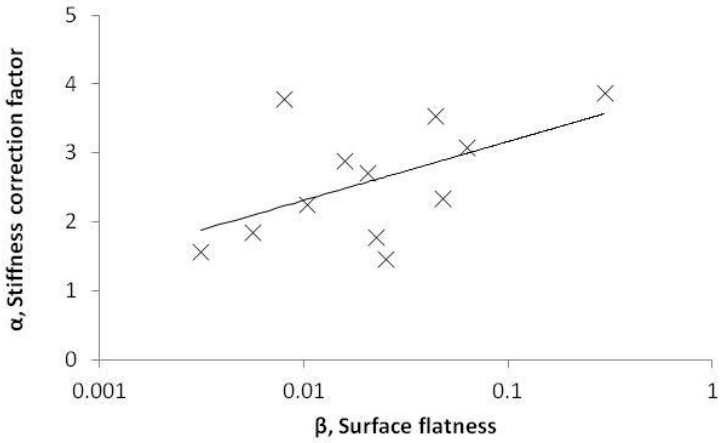

Figure 3.17 Graph of stiffness correction factor plotted against surface flatness.

A shear stress contour plot pattern similar to that observed in study 1 (Figure 3.13) was observed in all explants with an average maximum shear stress of 0.15MPa.

RMSE and SEE values were calculated (Table 3.1) for each explant and surface flatness, β was calculated using equation (3). Stiffness correction factor, α was plotted against surface flatness, β on a logarithmic scale. A logarithmic trend line described using equation (4) was fitted with a R^2 value of 0.5425 (Figure 3.17).

$$\alpha = 0.519 \ln(\beta) + 2.8693 \quad (3.4)$$

3.3 Discussion

The primary goal of this study was to investigate the significance of an accurate surface geometry representation of the AC explants on the prediction of stress and strain experienced in the tissue during mechanical loading.

In the axisymmetric model, transversely uniform depth varying local strain different to that of the bulk tissue strain was noted. This has been reported previously in the literature[27]. However, strain predicted in the explant specific models varied in both the vertical and radial axis (Figure 3.15). Comparison between the axis-symmetric and explant specific models showed that at the point of initial contact, maximum nodal displacement was underestimated by 74.6%. The surface geometry in the explant specific models were found to cause significant shear stress patterns and maximum principal stresses that were not present in the axis-symmetric model, indicating that the surface geometry has induced additional triaxial stresses in the tissue during the unconfined uni-axial compression test (Figure 3.13).

Generalised stress and strain patterns were observed in the explant-specific finite element models. There was no correlation between explants subjected to higher bulk tissue strains and those with higher tissue stress and strain values. This was due to the irregular surface geometries. Therefore, explant-specific surface finite element models are important.

Previous research investigating the effects of friction on FE predictions for unconfined compression comparing results from a lubricated and adhesive fixed surface-platen interface found that frictional effects were only significant for small aspect ratios of approximately 0.28, where aspect ratio is the thickness divided by the diameter of the explant. For aspect ratios of approximately 0.8, frictional effects are minimal[28]. Aspect ratio of the axis-symmetric cylinder studied was 0.21 and therefore, coefficient of friction of 0.01 could have been included in the model. In the explant specific models, the surface curvature would result in a non-constant contact area which increasing with loading. The rate at which the contact area increases with loading would depend on the surface curvature. It is therefore, expected that the effect of friction would increase during loading dependent on the surface curvature. Significance of such effects will require further investigation.

The alignment of the explant relative to the platen could also have a significant effect on the FE results predicted. In this study, the information was not recorded during mechanical loading. In future studies, an improvement to the positioning of the explants relative to the platen is required. Additional possible cause for error in the surface contour measurement is the presence of synovial fluid. The magnitude and the significance of the error were not investigated in this study.

Thicknesses of AC explants measured were within the range 1.65-2.65mm agreeing with those found in the literature for femoral condyles[29]. Furthermore, the instantaneous compressive modulus of individual AC explants and the average compressive modulus of each condyle determined using the explant-specific models were found to agree with those reported previously in the literature[30 31]. In contrast, the mean aggregate compressive moduli calculated from experimental data assuming flat AC surfaces were significantly lower than the range of 4.3MPa and 13MPa reported in a previous study[25]. It was observed that explants taken from the lateral side of the same lateral condyle had lower compressive modulus compared to those taken from the medial location. Furthermore, explants taken

closest to the zenith of each condyle were noted to have the highest compressive modulus of 8.23MPa, 12.87MPa and 9.84MPa. The same correlation was noted with the uncorrected compressive modulus values. However, only after correction using the finite element analysis, were the determined values of compressive modulus comparable to the compressive modulus of normal AC at the zenith of femoral condyles found in previous studies which reported a mean value of 13.1 ±3.6 MPa[32].

A robust non-contact method combining the use of digital image correlation and 3D image registration to extract the surface geometry of each individual explant has been presented and used for creating explant-specific finite element models in this study. Although, it was not possible to compare the accuracy of surface curvature of the FE model against the physical explant and future examination would prove insightful. In this study, a linear elastic model was used for an isolation study on effects of the geometry. It is recommended that in the future, improved constitutive models for AC, such as those described in Section 2.1.4.4, be incorporated for better prediction of boundary conditions, i.e. local stresses and strains, to apply to ECM-PCM-chondrocyte FE models[2].

A number of surface analysis parameters, such as root mean square of the centre line average, skewness, kurtosis, were initially explored and calculated to quantify and make comparable the surface geometries of each explant. During analysis, correlation was only noted between the root mean square error of the best fit plane which indicates the closeness of the explant's surface to a flat surface, the sum of the square error of the corrected plane which represents the volumetric error between the assumed geometry and the real surface geometry, and the stiffness correction factor.

A correlation was observed between the errors in stiffness calculated and the product result of the conformity of the explant surface to a flat surface and the

volumetric error introduced by the geometry assumption. Although a relationship equation has been established in this study, due to a small sample number, the equation should only be taken as a suggestion. Application of the equation on explants of other diameters has not been explored. It is proposed that in the future, with greater sample numbers, a stiffness correction factor could be calculated based on known surface parameters without the need of carrying out inverse finite element modelling on explant-specific models to determine the correct instantaneous stiffness of the material.

In conclusion, explant-specific finite element models are essential for accurate determination of AC explants' material properties and prediction of tissue stresses and strains. This is particularly relevant for gene expression studies where cutting of the surface is not possible. Surface undulations can significantly alter the stress and strain patterns and induce additional stresses, such as shear stresses inside the tissue. In addition, it was demonstrated that the flat surface assumption used in inverse FE models could introduce significant errors in the prediction of material stiffness.

3.4 Acknowledgments

Mechanical loading experiment was conducted by Mr. Andrew Metcalfe and Dr. Emma Blain.

3.5 Figures

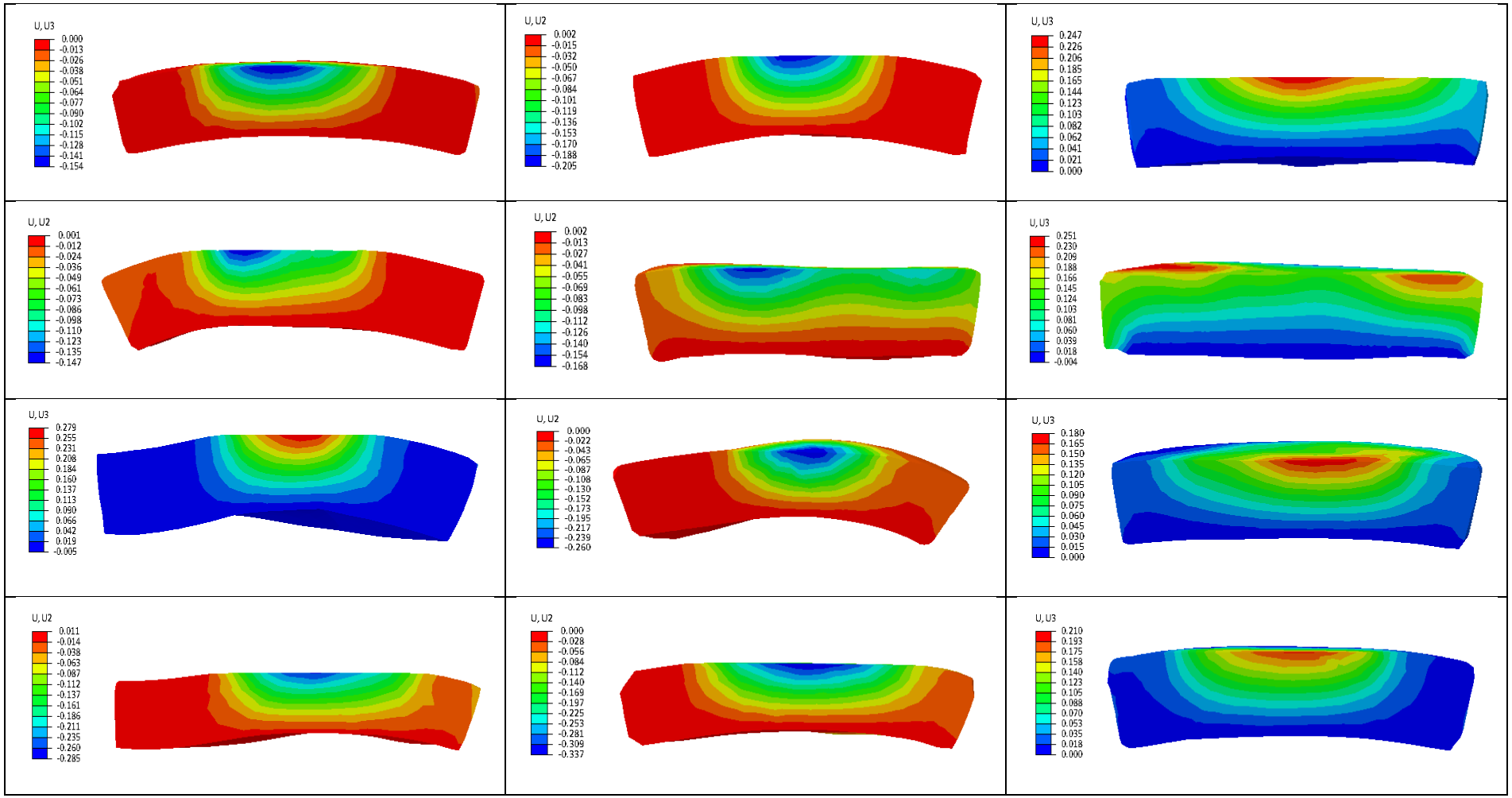

Figure 3.18 Cross-section view at mid-diameter of nodal displacement contour plot for each explant-specific FE model. Column 1: Explant 1A-1D from top to bottom, Column 2: Explant 2A-2D and Column 3: Explant 3A-3D.

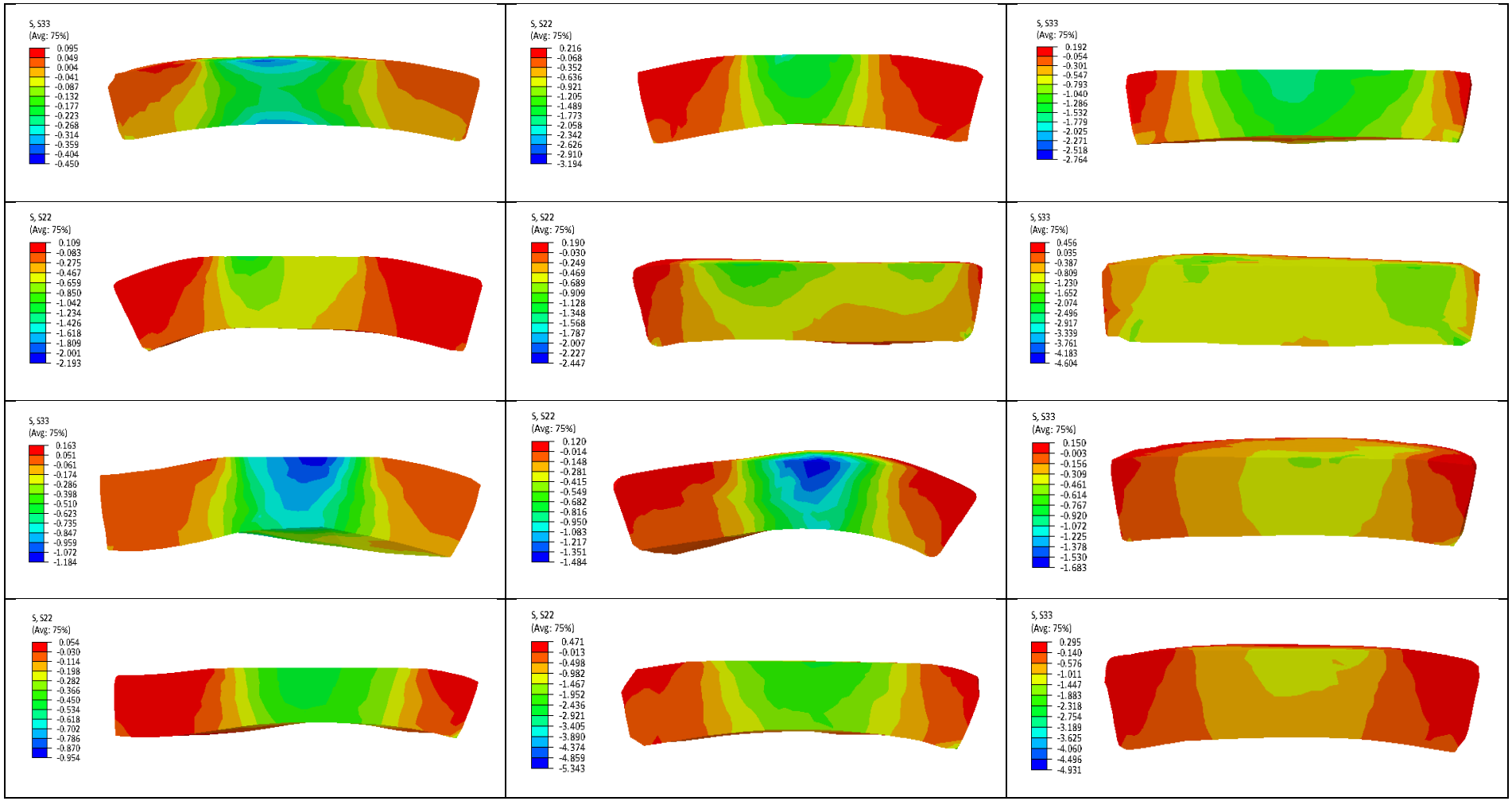

Figure 3.19 Cross-section view at mid-diameter of vertical stress component contour plot for each explant-specific FE model. Column 1: Explant 1A-1D from top to bottom, Column 2: Explant 2A-2D and Column 3: Explant 3A-3D.

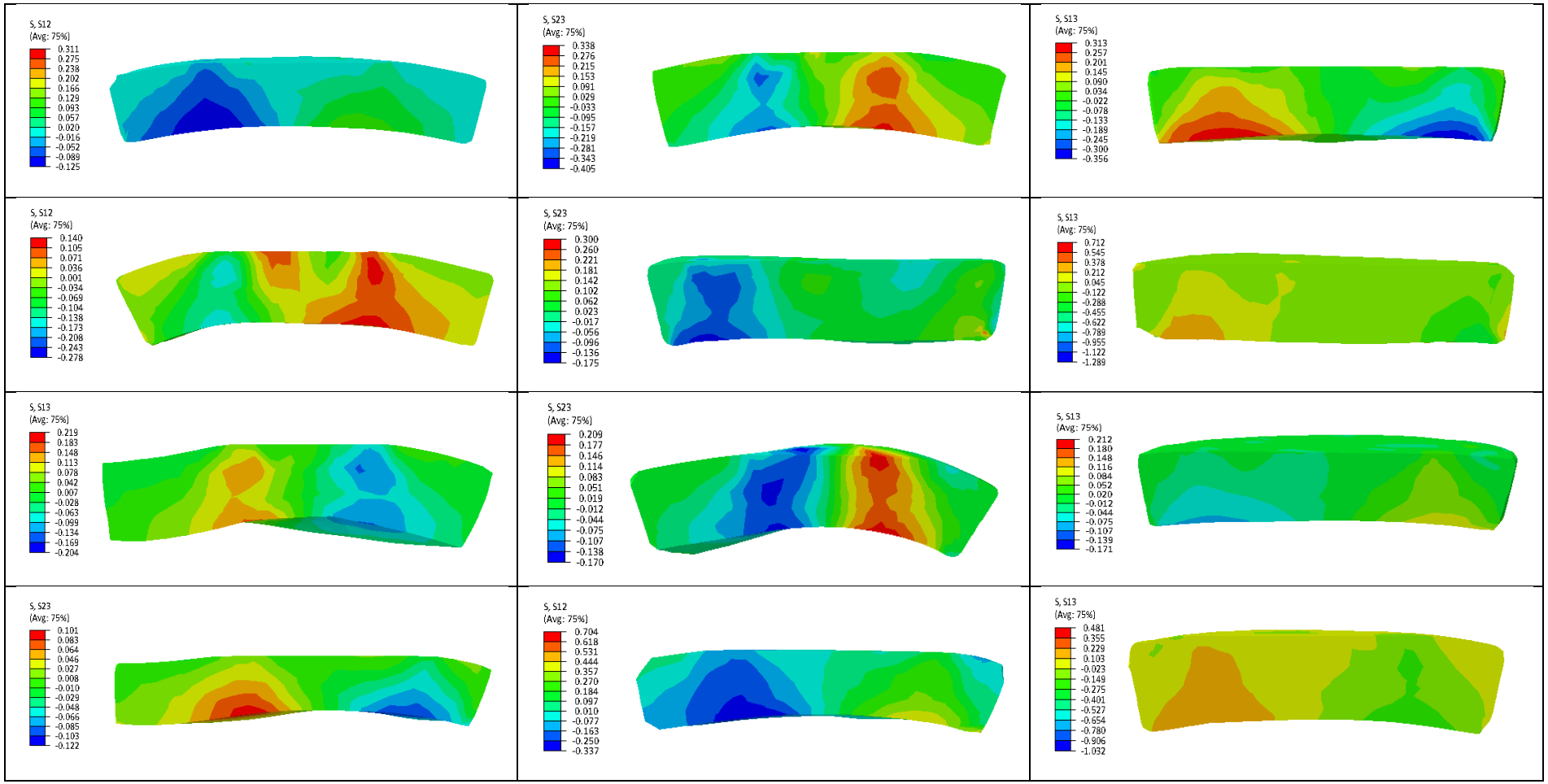

Figure 3.20 Cross-section view at mid-diameter of shear stress contour plot for each explant-specific FE model. Column 1: Explant 1A-1D from top to bottom, Column 2: Explant 2A-2D and Column 3: Explant 3A-3D.

3.6 References

[1] M.A. McLeod, R.E. Wilusz and F. Guilak, 'Depth-dependent anisotropy of the micromechanical properties of the extracellular and pericellular matrices of articular cartilage evaluated via atomic force microscopy', Journal of Biomechanics, 46(3):586-592, 2013

[2] L.G. Alexopoulos, L.A. Setton and F. Guilak, 'The biomechanical role of the chondrocyte pericellular matrix in articular cartilage', Acta Biomaterialia, 1(3):317-326, 2005

[3] P.S. Donzelli, R.L. Spiler, G.A. Ateshian and V.C. Mow, 'Contact analysis of biphasic transversely isotropic cartilage layers and correlation with tissue failure', J Biomech, 32:1037-1047, 1999

[4] S. Chegini and S.J. Ferguson, 'Time and depth dependent poisson's ratio of cartilage explained by an inhomogeneous orthotropic fiber embedded biphasic model', J Biomech, 43(9):1660-1666, 2010

[5] M.R. DiSilvestro, Q. Zhu, M. Wong, J.S. Jurvelin and J-K. F. Suh, 'Biphasic poroviscoelastic simulation of the unconfined compression of articular cartilage: I- Simultaneous prediction of reaction force and lateral displacement', J Biomech Eng, 123:191-197, 2001

[6] W. Wilson, C.C. van Donkelaar, B. van Rietbergen, K. Ito and R. Huiskes, 'Stresses in the local collagen network of articular cartilage: a poroviscoelastic fibril-reinforced finite element study', J of Biomech, 37:357-366, 2004

[7] W. Wilson, C.C. van Dokelaar, B. van Rietbergen and R. Huiskes, 'A fibril reinforced poroviscoelastic swelling model for articular cartilage', J Biomech, 38:1195-1204, 2005

[8] J.Z. Wu and W. Herzog, 'Simulating the swelling and deformation behavior in soft tissues using a convective thermal analogy', BioMed Eng Online, 1:8, 2002

[9] W. Wilson, C.C. van Donkelaar and J.M. Huyghe, 'A comparison between mechano-electrochemical and biphasic swelling theories for soft hydrated tissues', J of Biomech Eng, 127:158-165

[10] P. Julkunen, P. Kiviranta, W. Wilson, J.S. Jurvelin and R.K. Korhonen, 'Characterization of articular cartilage by combining microscopic analysis with a fibril-reinforced finite-element model', J Biomech, 40:1862-1870, 2007

[11] M. Kauer, V. Vuskovic, J. Dual, G. Szekely and M. Bajka, 'Inverse finite element characterization of soft tissues', Medical Image Analysis, 6(3):275-287, 2002

[12] S. Evans and S. Avril, 'Identification of material parameters through inverse finite element modeling', Computer Methods in Biomechanics and Biomedical Engineering, 15(1):1-2, 2012

[13] M.E. Levenston, E.H. Frank and A.J. Grodzinsky, 'Electrokinetic and poroelastic coupling during finite deformations of charged porous media', Journal of Applied Mechanics, 66: 323-333, 1999

[14] X.L. Lu and V.C. Mow, 'Biomechanics of articular cartilage and determination of material properties', Medicine & Science in Sports & Exercise, 40(2): 193-199, 2008

[15] A.D. Pearle, R.F. Warren and S.A. Rodeo, 'Basic science of articular cartilage and osteoarthritis', Clin Sports Med, 24:1-12, 2005

[16] S.S. Chen, Y.H. Falcovitz, R. Schneiderman, A. Maroudas and R.L. Sah, 'Depth-dependent compressive properties of normal aged human femoral head articular cartilage: relationship to fixed charge density', Osteoarthritis Cartilage, 9(6):561-569, 2001

[17] I. Redler and L. Zimny, 'Scanning Electron Microscopy of normal and abnormal articular cartilage and synovium', J Bone Joint Surgery, 52-A(7):1395-1404, 1970

[18] J.P. Wu, T.B. Kirk and M.H. Zheng, 'Study of the collagen structure in the superficial zone and physiological state of articular cartilage using a 3D confocal imaging technique', J Ortho Surg Res, 3:29, 2008

[19] P.S. Walker, J. Sikorski, D. Dowson, M.D. Longfield, V. Wright and T. Buckley, 'Behaviour of synovial fluid on surface of articular cartilage a scanning electron microscope study', Annals of the Rheumatic Disease, 28:1-14, 1969

[20] D.L. Gardner, 'The influence of microscopic technology on knowledge of cartilage surface structure', Annals of the Rheumatic Disease, 1972, 31; 235-257

[21] A.J. Metcalfe, C. Stewart, N. Postans, A.L. Dodds, C.A. Holt and A.P. Roberts, 'The effect of osteoarthritis of the knee on the biomechanics of other joints in the lower limbs', Bone Joint J, 95(3):348-353, 2012

[22] G. Li, O. Lopez and H. Rubash, 'Variability of a three-dimensional finite element computational model of a human knee joint', ASME Journal of Biomechanical Engineering 121: 657-662, 2001

[23] H. Forster and J. Fisher, 'The influence of loading time and lubrication on the friction of articular cartilage', Proceedings of the Institute of Mechanical Engineers, Part H: Journal of Engineering in Medicine, 210:109-119, 1996

[24] S.L. Evans, 'Errors and uncertainties in the indentation testing of soft tissues', International Conference on the Mechanics of Biomaterials and Tissues, 2010

[25] J.M. Mansour, 'Chatper 5: Biomechanics of cartilage', In Kinesiology: The mechanics and pathomechanics of human movements (Oastis, C.A. ed.), Lippincott Williams and Wilkins, Philadelphia, Ch.5, 66-79, 2003

[26] K.E. Moglo and A. Shirazi-Adl, 'On the coupling between anterior and posterior cruciate ligaments, and knee joint response under anterior femoral drawer in flexion: a finite element study', Clinical Biomehcanics, 18:751-759, 2003

[27] F. Guilak, A. Ratcliffe and V.C. Mow, 'Chondrocyte deformation and local tissue strain in articular cartilage: a confocal microscopy study', Journal of Orthopaedic Research, 13:410-412, 1995

[28] R.L. Spilker, J.-K. Suh and V.C. Mow, 'Effects of friction on the unconfined compressive response of articular cartilage: a finite element analysis', Journal of Biomechanical Engineering, 112: 138-146, 1990

[29] D.E.T. Shepherd and B.B. Seedhom, 'Thickness of human articular cartilage in joints of the lower limb', Ann Rheum Dis, 58:27-34, 1999

[30] M.K. Barker and B.B. Seedhom, 'The relationship of the compressive modulus of articular cartilage with its deformation response to cyclic loading: does cartilage optimize its modulus so as to minimize the strains arising in it due to the prevalent loading regime?', Rheumatology, 40:274-284, 2001

[31] F. Boschetti, G. Pennati, F. Gervaso, G.M. Peretti and G. Dubini, 'Biomechanical properties of human articular cartilage under compressive loads', Biorheology, 41:159-166, 2004

[32] S. Roberts, B. Weightman, J. Urban and D. Chappell, 'Mechanical and biomedical properties of human articular cartilage in osteoarthritic femoral heads and in autopsy specimens', The Journal of Bone and Joint Surgery, 68-B(2):278-288, 1986

Chapter 4 Reconstruction of finite element models from patient specific MR imaging data of the knee

The aim is to assess the feasibility and establish a protocol to create finite element models from patient specific image data obtained from MRI for the HTO cohort at the ARUKBBC. Patient factors, such as convenience, time, comfort and ethics is an important consideration in setting up such protocol. HTO patients have a clinical MR imaging scan of the knee as part of their clinical treatment. However, clinical MR imaging scanners typically have a magnetic field strength of 1.5 Tesla or lower. Low magnetic field strength negatively affects the signal-to-noise ratio (SNR), resolution of the image and acquisition time. Although it was not possible to obtain the MR data for dissemination, the suitability of clinical MR image scan data for the HTO patients was examined and proven to have insufficient resolution and had a poor SNR. It was therefore proposed that the 3T MR imaging scanner at CUBRIC is to be used. Other than the magnetic field strength of the scanner, the quality of the MR scan image is a compromise between the long acquisition time and high resolution.

Reconstruction of tissue geometries from MR images involve the stages of (1) tissue delineation (2) segmentation of the geometries (3) meshing of the geometries. The objectives were therefore:

- Work in conjunction with the dynamic and loaded MRI project collecting tissue kinematics data, identify a suitable MR scan sequence with a reasonable acquisition time that would allow sufficient resolution for

delineation of the following tissues: bones, menisci, articular cartilage and ligaments.

- Assess the suitability of the segmentation tools in imaging processing software, Simpleware, for segmentation of the tissues. Establishing a protocol that minimises operator effort, input and subjectivity.
- Investigate possible errors in geometry introduced during the meshing process and meshing algorithms in image processing software, Simpleware.

The protocol used for creating the full joint contact FE knee model used in this creating the FE model in Chapter 6 of this thesis is detailed in Section 4.

4.1 MR scan sequence for delineation of soft and hard tissues

4.1.1 Methods

As part of the ARUKBBC research protocol for HTO patient volunteers, MR imagining scan data from the 3Tesla MR imaging scanner of their knee can be obtained. MR imaging scan sequence can have a profound effect on the resolution and signal to noise ratio of the acquired image data. The resolution and signal to noise ratio are determining factors of the ease of tissue delineation. Though the higher resolution could mean increased acquisition time. Two scan sequence were considered: A Gradient Recalled Echo scan (GRE) sequence, known for significant reduction in acquisition time by employing small flip angles, which also consequently reduces T1 weighting[1]. And a Fast Imaging Employing Steady-State Acquisition (FIESTA-C), which utilizes the T2 steady state contrast mechanism. FIESTA-C is known for producing high SNR images of fluid filled tissues where a strong contrast against background tissues with lower water content is possible.

Two sets of MR images of healthy knees from the age group 40+ and 20+, acquired using different scan sequences and resolutions on the same 3 Tesla MR scanner manufactured by General Electric were compared for ease in delineating the tissue

boundaries. The suitability of the image scan data for tissue delineation was assessed by the examining the greyscale contrast and transition between adjacent tissues. Primary interest was focused on obtaining patient specific geometries of the bones (femur, tibia, fibula and patella), AC and menisci.

Set 1, acquired using a Gradient Recalled Echo scan (GRE) sequence, had 88 sagittal slices with a slice thickness of 1mm and in plane resolution of 1mm x 1mm for a field of view of 158mm x 114mm.

Set 2 was obtained using a Fast Imaging Employing Steady-State Acquisition (FIESTA-C) scan sequence which utilizes the T2 steady state contrast mechanism, was used and produced 186 sagittal slices with a slice thickness of 0.5mm and in-plane resolution of 0.37mm x 0.37mm for a field of view of 93mm x 182mm.

4.1.2 Results

Delineation of the menisci was not possible on Set 1 MR scan data obtained using GRE, as there was minimal greyscale contrast between voxels belonging to the menisci and those belonging to the adjacent AC tissue. In addition, in-plane resolution of 1mm was also found to be too low for accurate representation of AC which has a typical thickness of approximately 2mm (Figure 4.1).

MR imaging data from Set 2 showed a clear distinction of the high signal intensity regions (bright) for cancellous bone surrounded by a low signal intensity region (dark), which helped to differentiate the high signal intensity voxels for AC from those for cancellous bone. The low signal intensity zone found between cancellous bone and AC has been reported to be the transition region between bone and AC, which includes both cortical bone and calcified AC[2 3]. Voxels of menisci had low signal intensity which helped to separate the femoral and tibial AC layers (Figure 4.1). Furthermore, it was noted that the patellar ligament and cruciate ligaments were also identifiable as regions of low signal intensity (Figure 4.2).

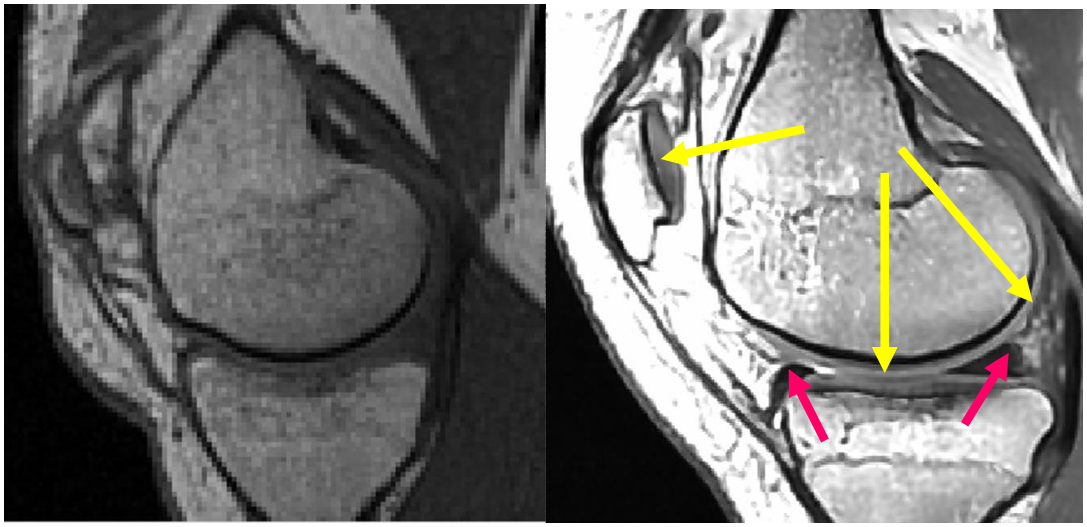

Figure 4.1 Left: An image of a sagittal slice from SET 1. Although voxel greyscale contrast of adjacent tissues was sufficient for bone delineation, the boundaries of the meniscus, AC and ligaments were difficult to identify. Right: Representative slice taken from Set 2 which shows a comparatively higher signal to noise ratio. The higher resolution allows AC (indicated by yellow arrows) to be represented by a greater number of voxels across its thickness. Menisci (indicated by pink arrows) have a low signal intensity which helped to separate the femoral and tibial AC.

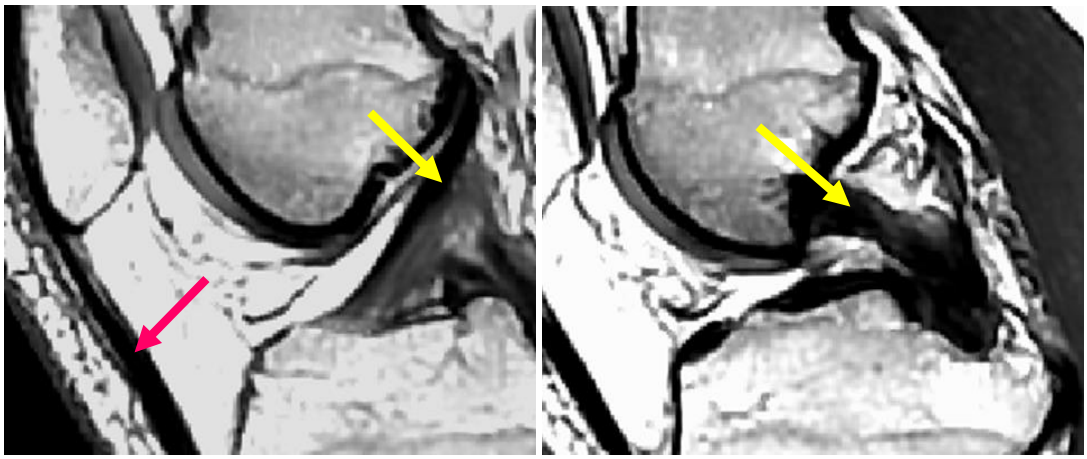

Figure 4.2 Left: Patella Ligament indicated by pink arrow and Anterior Cruciate Ligament (ACL) indicated by yellow arrow Right: Posterior Cruciate Ligament (PCL).

Greyscale values of voxels along the super-inferior axis across a sagittal slice taken from the medial compartment were plotted for both set 1 and set 2 (Figure 4.3 and 4.4). Greyscale values range from 0-255, where voxels with 0 appear black and 255

appear white. On the graph, it can be seen that transitions from one tissue to another are clearly marked by a distinct change in the signal intensity.

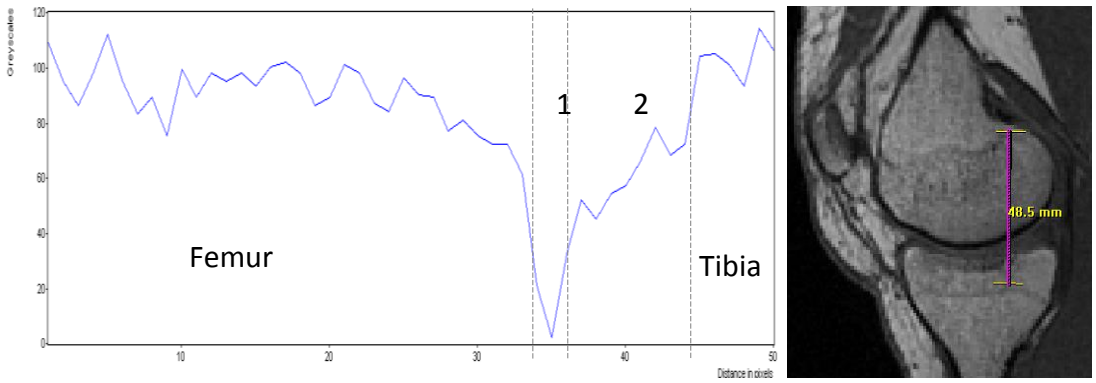

Figure 4.3 Plot of voxel greyscale values along a profile line on a sagittal slice taken from the posterior part of the medial compartment of Set 1. Regions of higher greyscale values for the femur and tibia and a region of low signal intensity for femoral cortical bone (1) can be identified. However, the femoral AC-meniscus-tibial AC transition in the middle region (2) is difficult to delineate.

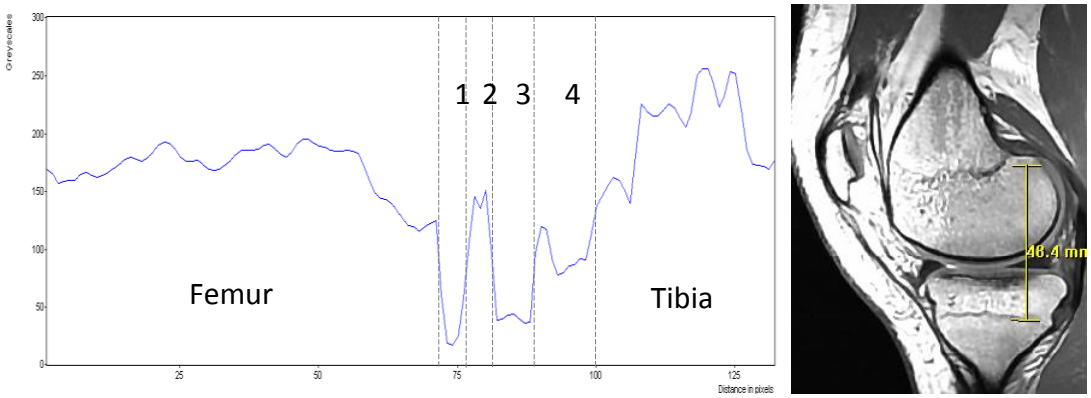

Figure 4.4 Plot of voxel greyscale values along a profile line on a sagittal slice taken from the posterior part of the medial compartment of Set 2. A distinct transition of greyscale values can be seen, from high signal intensity for the femoral cancellous bone region, to low intensity for the femoral cortical bone region (1), to high signal intensity for the femoral AC region (2), then low signal intensity for the medial meniscus (3), through to relatively higher tibial AC (4) and finally a high signal intensity region for the tibia.

4.2 Segmentation of soft and hard tissues

As discussed in Section 2.2.1, the use of a completely automated segmentation algorithm for generation of patient specific tissue geometries from MR imagining data is not currently possible using the tools available. This is due to the complexity of the tissue structures in the knee, variability of the greyscale values of voxels belonging to the same tissue, as well as, the overlapping greyscale value range for voxels belonging to two different tissues.

4.2.1 Methods

Three semi-automated segmentation algorithms available in image processing software, Simpleware, were explored: floodfill, confidence region growing and paint with threshold (see section 2.2.1 for explanation).

Floodfill requires the boundary of the tissue of interest to first be clearly defined. Pixels within this boundary are than automatically assigned to the same tissue. For tissues with a clear boundary of pixels with contrasting greyscale, such as bone (Figure 4.2), threshold can be used to pick out the boundary and floodfill can potentially offer a great reduction in time.

Providing an appropriate seed and algorithm parameter have been chosen, confidence region growing has the greatest potential for reducing operator effort and subjectivity. The iterative process for determining greyscale bounds also allows the algorithm to cope with mechanical properties variation in a tissue, which would give rise to variation in greyscale.

Comparatively, threshold plant requires most operator effort. Though, operator subjectivity would be the same as that of floodfill. This is because floodfill requires the use of threshold to first define the boundary. Threshold is a filter, where the operator is required to define the range of greyscale of interest. The filter then automatically selects all pixels belonging to that greyscale. In the case of threshold

paint, the operator needs to paint over the pixels believed to belong to the tissue of interest, but only pixels with greyscale within the range defined can be selected.

Operator effort and the ability of the algorithm to delineate pixels belonging to the tissue of interest correctly with minimal operator input were used to assess the suitability of the segmentation algorithm.

4.2.2 Results

As seen in Figure 4.1, multiple regions in the image scan data had pixels belong to the same threshold. Therefore, the use of threshold alone was not possible. As a result, the pixels defining the boundaries of each tissue of interest had to be selected manually. The advantage of floodfill over full manual segmentation is that for tissues with a large volume to surface area ratio (approximately 4-5), such as the femur and tibia, the majority of the voxels are automatically selected. However, for tissues with a smaller volume to surface area ratio, such as the AC and meniscus, which is around 1, the time saving benefit was found to be small.

The use of confidence connected region growing for the knee MR imaging slices was found to be extremely sensitive and difficult to optimise. The greyscale values of voxels belonging to the same tissue appeared to vary within the slice and between each slice. For example, greyscale values for the femoral cancellous bone ranged from 111-255 in a slice from the medial side, whereas it ranged from 156-255 for a slice from the lateral side. This meant that too often, some voxels belonging to the mask were not selected and required correction using manual segmentation (Figure 4.5). Furthermore, in some areas where the boundary between adjacent tissues with similar greyscale values was not well defined, bleeding happened and incorrect voxels were selected (Figure 4.6).

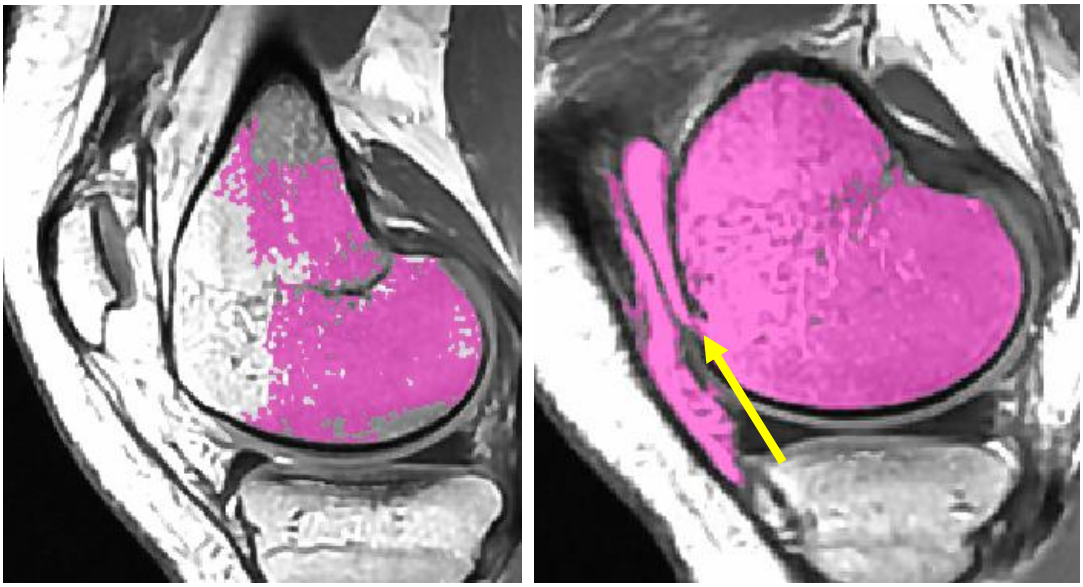

Figure 4.5 Left: Greyscale values of voxels belonging to the same tissue varied within slices and between slices, subsequently leading to problems where the voxels were not segmented. Right: Adjacent tissues with similar greyscale values often caused incorrect selection of voxels.

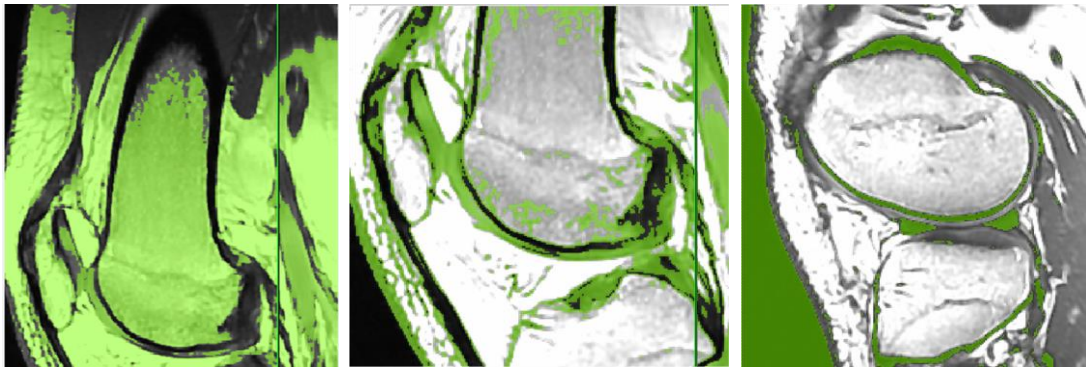

Figure 4.6 Paint with threshold tool used for selecting voxels belonging to the femur (left), femoral AC (middle) and meniscus (right). As seen above, greyscale threshold bounds set for each tissue also highlight voxels belonging to other tissues in other areas of the sagittal slice. The low signal intensity area in between the two tissues is shared by the compact cortical bone and calcified cartilage layer.

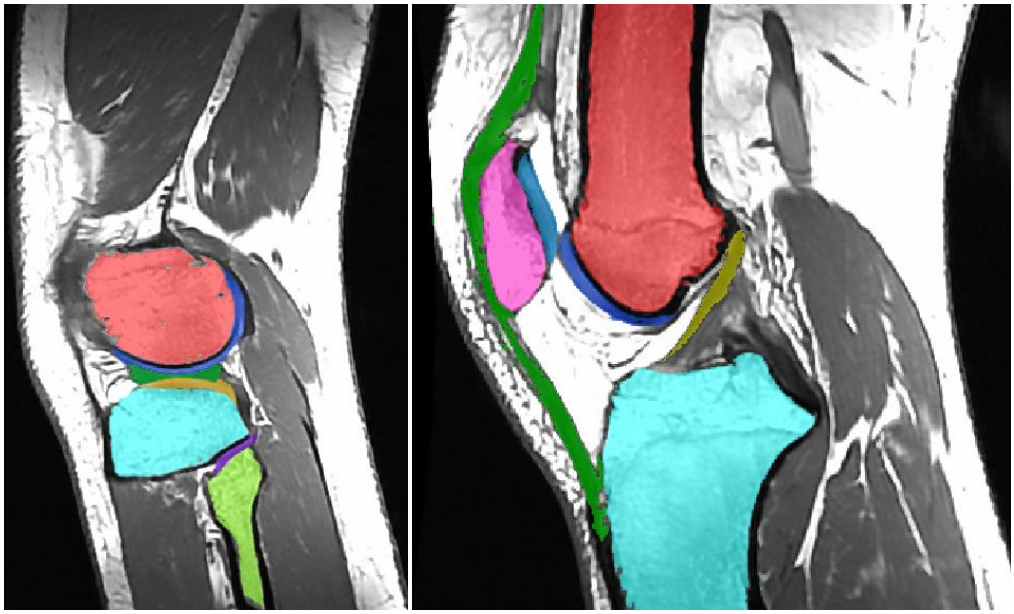

Figure 4.7 Left: A sagittal slice taken from the lateral side of the knee with femur (red), femoral AC (dark blue), lateral meniscus (dark green), tibial AC (yellow), tibia (light blue), fibula AC (purple) and fibula (light green) after segmentation Right: A sagittal slice taken from the intercondylar region showing the segmented masks for femur (red), femoral AC (dark blue), ACL (gold), tibia (light blue), patella AC (sky blue), patella (pink) and patella ligament (dark green).

It was found that the variation in greyscale values and the location for each tissue was small between the immediate adjacent slices. As a result, segmentation could be carried out on two to three slices at the same time using paint with little error, thereby, reducing both time and effort required immensely. Using the 'paint with threshold' algorithm, the bones (femur, tibia, fibula and patella), their respective AC, lateral and medial meniscus, patella ligament and anterior and posterior ligament were segmented (Figure 4.7 and 4.8).

Upper and lower bounds for greyscale value used for delineating bone, menisci, AC and ligaments were $105<\Psi<255$, $0<\Psi<59$, $56<\Psi<156$ and $0< \Psi<32$ respectively. However, as mentioned before, due to the inter- and intra- slice variability of the greyscale values within the same tissue, some small adjustments to the upper and lower bounds for greyscale values were required for some slices.

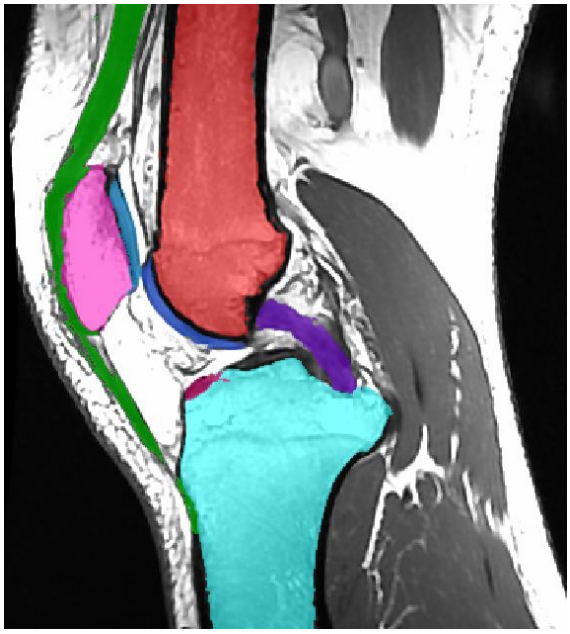

Figure 4.8 A sagittal slice taken from the intercondylar region with femur (red), femoral AC (dark blue), PCL (purple), medial meniscus (dark pink), tibia (light blue), patella AC (sky blue), patella (pink) and patella ligament (dark green) after segmentation.

4.3 Meshing of the geometries

Stacking of the selected segmented voxels on each slice to reconstruct the 3D volume is automated in ScanIP v5.0, Simpleware Ltd and meshing can be done using two available meshing algorithms, FE Grid and FE Free with the +FE module, Simpleware Ltd.

4.3.1 FE Grid meshing algorithm

FE Grid is a meshing algorithm available in Simpleware, Simpleware Ltd., which is based on a hybrid of the marching cube and the voxel based meshing algorithms[4]. The algorithm which is voxel based essentially creates a hexahedral mesh for the segmented volume. Utilizes the marching cube based method, which is known for its ability to create meshes true to the surface geometry of the segmented volume, the algorithm creates tetrahedral elements for the surface layer that are compatible with the hexahedral mesh. The algorithm was further extended to allow

inhomogeneous mesh densities by the use of an octree-based approach. The idea is that at the center of the volumes, away from the surfaces, clusters of elements can be replaced by equivalent elements of a larger size. This allows a coarser mesh in the centre of large segmented volumes and thereby, reducing the mesh size. The FE Grid algorithm does not allow localised mesh refinement in areas of interest and therefore, was not considered.

4.3.2 FE Free meshing algorithm

The FE Free meshing algorithm is fundamentally an extension of the FE Grid meshing algorithm to improve surface feature preservation. The algorithm takes the surface mesh generated using the FE Grid meshing method and remeshes the surface of the segmented volume taking into account surface features. Based on the new surface mesh created, the algorithm then populates the internal volume with tetrahedral elements using a Delaunay/ advancing front algorithm[4].

Consequentially, the mesh density of the final meshed geometry is based on the resolution of the MR imaging data, as well as, the surface topology of the segmented volume. Meshing of the model with original data resolution results in a femoral part mesh of 2.5 million elements. Therefore, pre-mesh preparation where a smoothing algorithm is applied to remove the ridges from the voxel edges of the segmented volume and resampling data to a lower resolution is required.

For better surface feature preservation and the availability of a mesh refinement tool for areas of interest, the FE free meshing algorithm will be used. Compound coarseness is a single value which automatically controls the multiple advanced meshing parameters for the FE free meshing algorithm. This is similar to the idea of the mesh density adjustment tool in FE Grid for mesh size reduction. In FE free element reduction is done based on the intricacy of the surface topology. The operator chooses the value of compound coarseness and the algorithm calculates and optimizes the parameters responsible for defining the size of the elements and

the transition from high to low density regions. A compound coarseness value set to zero means no element reduction will be applied.

4.3.3 Methods

The amount of data resampling required is a compromise between mesh geometry accuracy and the mesh size. The compound coarseness applied during the meshing processes can also greatly affect the mesh size and quality. The effects of data resampling and the use of compound coarseness on the resulting mesh size and quality specifically for generating patient specific finite element knee models was investigated. For the current full joint contact finite element knee model, only the bones, AC and menisci were to be included and therefore, the meshing protocol using the FE Free algorithm was investigated with consideration of these tissues only.

4.3.3.1 Data resampling

AC and meniscus thicknesses are approximately 1-2mm[5] and 3-5mm[6] respectively and the original data resolution was 0.37 x 0.37 x 0.5mm. The data was resampled to two different resolutions of 0.9 x 0.9 x 0.9mm, 1.8 x 1.8 x 1.8mm and 2.7 x 2.7 x 1.8mm using the nearest neighbour interpolation method. Voxel size in the S-I axis have been chosen to be below 2mm in order to avoid missing sections in the AC. The volume of the segmented tissues before and after data re-sampling are compared to examine the errors introduced.

4.3.3.2 Compound coarseness and mesh refinement

The correct value for compound coarseness and about of mesh refinement required was examined. The optimum values were determined by the lowest no. of elements required whilst maintaining good element quality. Good element quality is defined by the in-out aspect ratio and the maximum edge length. In-out aspect ratio[4] is defined as the inscribed sphere radius,r_i, divided by the circumscribing sphere radius, r_o, multiplied by a factor of 3 (Figure 4.9).

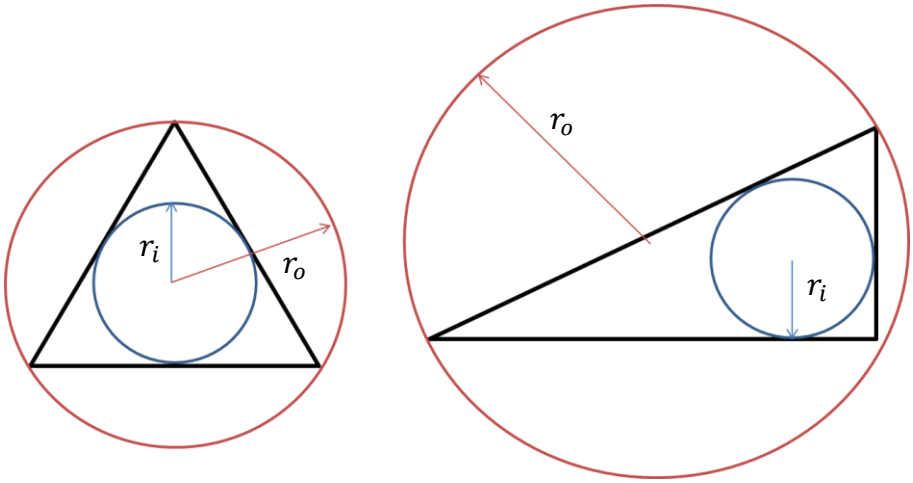

Figure 4.9 Good vs. bad In-out aspect ratio

Maximum edge length aspect ratio is defined as the length of the longest edge dived by the shortest edge of an element[4]. Tetrahedral elements with an in-out aspect ratio less than 0.1 and a maximum edge length ratio greater than 10, may give rise to near zero volume and distorted element problems leading to failure of the finite element analysis.

4.3.4 Results

4.3.4.1 Effects of data resampling

It was found that resampling to 1.8 x 1.8 x 1.8mm and 2.7 x 2.7 x 1.8mm helped significantly in reducing the number of elements required to mesh tissues with large volume to surface area ratios, such as the femur and tibia. However, the accuracy of the final model volume and shape of AC and meniscus were compromised due to the thinness of the tissues (Figure 4.9).

Resampling to a lower resolution caused a reduction in the volume of the tissues, therefore some regions of smaller volume and thinner sections were lost. In order to produce a usable mesh, a morphological filter, dilate, had to be applied to increase the volume of AC and menisci, thus, significantly changing their volume

and surface area (Table 4.1). Though, it was noticed that the change in ratio of volume to surface area for each tissue remained relatively constant.

Volumetric Absolute error was taken as the difference in the volume of each tissue before and after resampling. Using the volumes of each tissue at original scan resolution, the volumetric percentage errors were also calculated and are presented in Table 4.1. Significant volumetric percentage errors, ranging from 0.54 – 5.45%, were observed for the menisci. Surface area absolute error and percentage error were calculated based on the same principals as the volumetric errors. The surface area absolute error ranged from 50-300mm^2 and the surface area percentage error were 1.13%, 1.67%, 1.41%, 1.36%, 2.78% and 2.04% for the femur, tibia, femoral AC, Tibial AC, lateral meniscus and medial meniscus.

Figure 4.10 A 3D render of the segmented volume for femur (pink) and femoral AC (blue). The data was resampled to 2.7 x 2.7 x 2.7 mm. The thickness of the AC layer had to be artificially increased due to aliasing from data resampling.

Table 4.1 Segmentation statistics of each tissue for the three models of different resolution and for the cropped femur and tibia model.

Tissue	Volume (mm^3)	Errors		Surface Area (mm^2)	Ratio
		Δ	$\%_{error}$		
Femur original	156,000	-	-	26,500	5.89
Femur 0.9mm res	157,000	1,000	0.64	26,600	5.90
Femur 0.9mm res (cropped)	104,000	-	-	18,200	5.71
Femur 1.8mm res	159,000	3,000	1.92	26,800	5.93
Femur 2.7mm res	157,000	1,000	0.64	26,700	5.88
Tibia original	96,200	-	-	18,000	5.34
Tibia 0.9mm res	96,600	400	0.42	18,100	5.34
Tibia 0.9mm res (cropped)	43,500	-	-	10,200	4.26
Tibia 1.8mm res	97,600	1,400	1.46	18,100	5.39
Tibia 2.7mm res	96,300	100	0.10	17,800	5.41
Femoral AC original	38,100	-	-	21,300	1.79
Femoral AC 0.9mm res	38,200	100	0.26	21,300	1.79
Femoral AC 1.8mm res	38,300	200	0.52	21,300	1.80
Femoral AC 2.7mm res	38,200	100	0.26	21,000	1.82
Tibial AC original	9,420	-	-	5,910	1.59
Tibial AC 0.9mm res	9,400	20	0.21	5,880	1.60
Tibial AC 1.8mm res	9,470	50	0.53	5,940	1.59
Tibial AC 2.7mm res	9,390	30	0.32	5,860	1.60
Lateral Meniscus original	3,720	-	-	2,520	1.48
Lateral Meniscus 0.9mm res	3,700	20	0.54	2,520	1.47
Lateral Meniscus 1.8mm res	3,900	180	4.84	2,590	1.51
Lateral Meniscus 2.7mm res	3,640	80	2.15	2,460	1.48
Medial Meniscus original	2,500	-	-	2,450	1.02
Medial Meniscus 0.9mm res	2,530	30	1.20	2,470	1.02
Medial Meniscus 1.8mm res	2,570	70	2.77	2,470	1.04
Medial Meniscus 2.7mm res	2,360	140	5.45	2,270	1.04

Resampling to 0.9 x 0.9 x 0.9mm provided a better resolution of the thickness of AC and meniscus with little aliasing whilst still allowing a reduction of elements in the final mesh. To further reduce the size of the final mesh volume, portion from the proximal femur and distal tibia were cropped, resulting in a volume reduction of 53,000mm (33.8%) and 53,100mm (55.0%) respectively. A recursive Gaussian smoothing algorithm was used and it was found that optimal required input parameters, σ_x, σ_y and σ_z were 3.6 for bone and AC and 1.8 for meniscus.

4.3.4.2 Compound coarseness and mesh refinement

The number of elements used to mesh the geometries reduced exponentially with decreasing compound coarseness (Figure 4.10). The reduction was also more significant in the femur, which had a higher volume to surface area ratio.

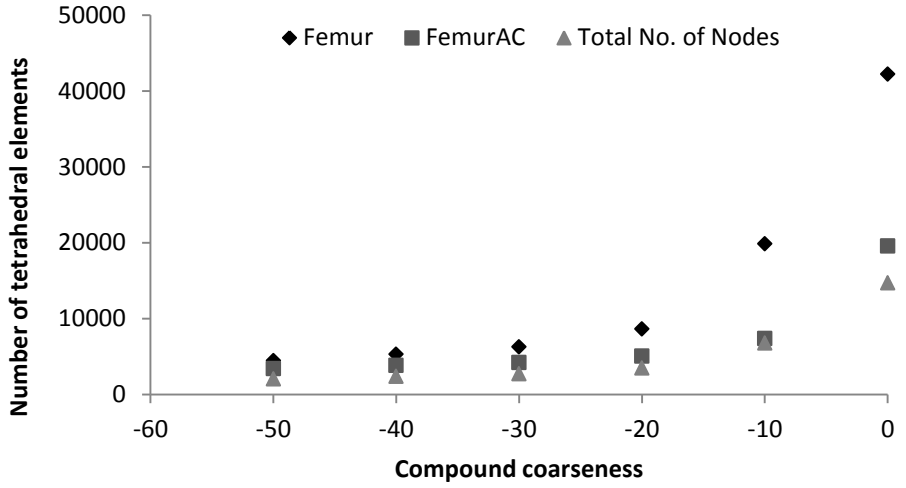

Figure 4.11 Total number of nodes and number of elements used to mesh the femur and femoral AC plotted against the compound coarseness value applied.

A compound coarseness of zero in the 2.7 x 2.7 x 2.7mm resolution model of the femoral part resulted in a model with a total of 61,773 tetrahedral elements where the femur had 42,228 elements and the femoral AC had 19,545. 10-node quadratic tetrahedral elements were used, giving the model, which has 14,692 nodes a total of 44,076 DOF. Applying a compound coarseness of -50, which is the maximum

amount of element reduction possible, resulted in a mesh with 4,437 elements for the femur and 3,404 for the femoral AC (Figure 4.11). This resulted in a mesh with 7.9 times fewer number of elements in total and a reduction in the individual parts for the femur and femoral AC by 9.6 and 5.7 times, respectively. The total number of nodes in the model was reduced to 2065 which gives 6,195 DOF.

However, element reduction caused the thin AC to be meshed with only one layer of tetrahedral elements, which resulted in poor quality elements with a low in-out aspect ratio and high maximum edge length aspect ratio values. Furthermore, complex stress distribution through the thickness of the AC in the area of contact is expected. Therefore a greater number of elements across the thickness of the AC layers are desirable.

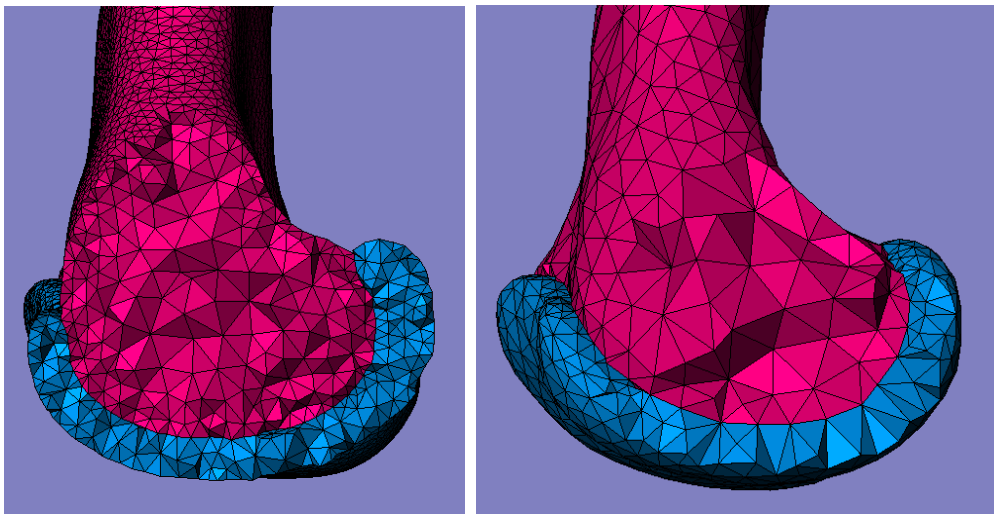

Figure 4.12 Left: 3D rendering of the femoral part finite element mesh with the femur (pink) and femoral AC (blue), showing the surface conformity between the two meshes. The model contains 61,773 tetrahedral elements and no element reduction was applied. Right: Maximum element reduction applied (compound coarseness = -50). The total number of elements used to mesh the model was reduced to 7,841.

To increase the number of elements used across the thickness of the femoral AC part whilst keeping the number of elements in the femur part low, the use of the 'mesh refinement' tool was explored. Mesh refinement allows a region of particular

interest to be apportioned a higher mesh density. Two mesh refinement mesh sizes were investigated i.e. with the maximum edge length target specified to be 3.6mm and 2.7mm.

On examination of a sagittal view cut model, it was found that mesh refinement with a 3.6mm maximum edge length target defined for femoral AC increased the number of elements across the thickness to two in most areas. For comparison, the number of elements for femur and femoral AC was 9,074 and 8,996 respectively with a total of 4480 nodes. However, there were still occasional single long thin elements found. Analysis of the meshing statistics revealed that the lowest in-out aspect ratio was 0.015, which is considerably below the recommended value of 0.1.

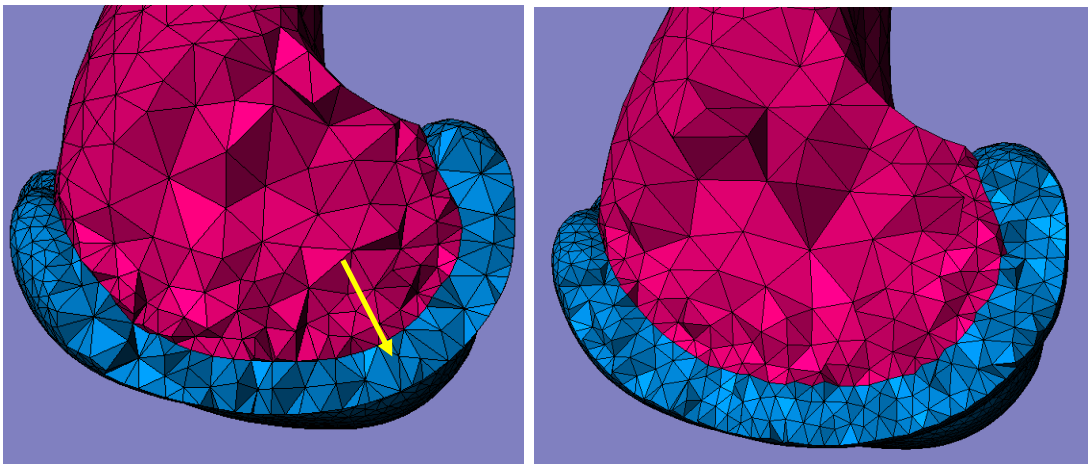

Figure 4.13 Mesh refinement used for the femoral AC part to increase the number of elements across the thickness and improve mesh quality. Left: mesh refinement with maximum edge length target in the femoral AC part set to 3.6mm, occasional single long narrow elements with poor mesh quality can be found (highlighted by yellow arrow) Right: mesh refinement with maximum edge length target set at 2.7mm.

Decreasing the maximum edge length target value set for mesh refinement in femoral AC to 2.7mm further increased the number of elements across the thickness (Figure 4.12). The total number of elements increased to 37,357 with 83,354 nodes, which was double the size of the mesh with 3.7mm maximum edge length target mesh refinement and comparable to the size of the model a

compound coarseness of -10. However, a larger proportion (64%) of the total number of elements for the femoral part was of AC mesh; in contrast, in the model with no mesh refinement, 73% of the total number of elements were of the bone mesh. The lowest in-out aspect ratio was 0.191 and maximum edge length aspect ratio was 9.68.

4.3.5 Considerations for exportation into FE package

After data resampling and smoothing, adjacent masks may overlap. Booleans algorithms can be used to resolve mask overlap by subtracting one from the other. However, it was found that resolving mask overlap prior to meshing led to small gaps between element surfaces between adjacent tissues in the final meshed geometry. These small gaps make it difficult for the 'find contact pairs' function in ABAQUS to identify surfaces that are in contact. Instead masks overlap had to be resolved first using Boolean to subtract the bone masks from its respective AC mask to ensure conformity of the two surface geometries. The morphological filter 'dilate' was then used on the bone to ensure the edges of the two masks overlapped ensuring no gap was present between the adjacent element surfaces in the final mesh.

A 'pre-smoothing' process was applied with 100 iterations for both the femoral and tibial part. The iterations increase the time required to mesh the models, however, it optimisation of the quality of the tetrahedral elements. 'Allow part change' was selected to allow reassignment of the surface voxels during the iterative smoothing process.

The knee joint tissues are physically under constant compression and therefore appear thinner than normal in the MRI scan data. As the femur, meniscus and tibia were segmented separated without resolving mask overlap with each other to allow for the true un-deformed state of the tissues, the geometries may interfere with one another. The femur and tibia components therefore, have to be translated

away from each other in the reconstructed model to create a gap large enough for the menisci to fit. Transformations of the tissues relative to each other in model space have to be done in ABAQUS and are required to be imported as separate instances. Exportation of a multi-part meshed model from Simpleware into ABAQUS creates a single instance with multiple sets of elements. Therefore, in order to be able to translate the femoral bone-AC component relative to the menisci and the tibial bone-AC component, these must be exported as separate ABAQUS input files (.inp). To ensure that the various tissues are imported into ABAQUS in the correct location relative to each other, the individual part meshes must be exported using the whole model's global coordinates. Four ABAQUS input files, one for the: femur bone and AC, tibia bone and AC, medial meniscus and lateral meniscus were created. These files were then imported into ABAQUS and combined into one model. The femur bone and AC component, as were as the menisci were then translated in the SI axis to avoid interference of the meshed geometries.

For the femur bone-AC component and tibia bone-AC component, although 'contact pairs' can be selected in the meshing dialog of Simpleware which automatically creates the interaction definition and surface sets for the touching element surfaces from the two neighbouring tissues, the surface sets cannot be copied between models in ABAQUS. 'Copy objects' is necessary for amalgamating the separate input files (.inp) for the femoral, tibial, lateral meniscus and medial meniscus models. It was therefore concluded that 'find contact pairs' in ABAQUS was the best method for creating the surface sets necessary for creating the tie contact between bone and AC. Mesh conformity was best when there was a small uniform overlap between the two adjacent masks which is automatically resolved in the pre-processing stage of the meshing algorithm.

4.3.5.1 Protocol used for creating the finite element model

1. Create a separate mask for each of the tissues to be segmented. (Femur, femoral AC, Tibia, Tibial AC, Lateral Meniscus and Medial Meniscus)

2. Set upper and lower threshold bounds for bones. **Segment** bones using paint with threshold and multi-slice selector tool in the sagittal view
3. Unpaint voxels at the distal end of the femur and tibia to **crop** the segmented volume to the desired size
4. Make bone masks (or any adjacent masks) invisible and repeat step 1 for the other soft tissues
5. Adjust the threshold for segmenting AC to include the low signal intensity area at the femoral bone and AC interface
6. **Resample** data to 0.9 x 0.9 x 0.9mm
7. Create four separate models to include masks as listed; 1. Femoral AC and femur, 2. Tibial AC and tibia, 3. Lateral meniscus, 4. Medial meniscus
8. Apply **recursive Gaussian smoothing** with sigma values of (3.6, 3.6, 3.6)mm to the femoral and tibial models (i.e. model 1 and 2)
9. Apply recursive Gaussian smoothing with sigma values of (1.8, 1.8, 1.8)mm to the menisci models (i.e. model 3 and 4)
10. Resolve mask overlap between bone and AC in both the tibial and femoral models
11. Apply morphological filter, dilate, with a structuring element ball of 1 pixel x 1 pixel x 1 pixel on the bones to establish a small uniform overlap between the bone and AC interface
12. Select the following parameters for the **meshing** options. In the pre-processing tab of the meshing dialog, select to apply pre-smoothing with 100 iterations, allow part change and export using absolute global coordinates. Deselect use greyscale values
13. In the volume meshing tab, select higher order in other options for quadratic elements. Set the advanced parameters manually for both femoral and tibial parts. Values are given in Table 4.2
14. In the contacts tab for the femoral part, add contact pair between femur and femoral AC.

15. Select model type ‘FE’ and export type ‘Abaqus volume (solid/shell). Mesh femoral model (model 1)
16. Check mesh statistics in the log toolbox; ensure lowest in-out aspect ratio is above 0.1 and maximum edge length aspect ratio is below 10.
17. **Export** model
18. Repeat step 15 to 17 for the tibial model (model 2)

Repeat step 15 to 17 for the lateral meniscus model (model 3) and medial meniscus model (model 4).

4.4 Discussion

MR imaging scan data from SET 2, acquired from a 3T GE MR machine using the scan sequence FIESTA-C with an in-plane resolution of 0.37 x 0.37mm and a slice thickness of 0.5mm provided good contrast between the menisci, AC and bones for delineation of their boundaries. Cancellous bone and AC with high signal intensity, which appeared as bright voxels, were separated by the cortical bone-calcified cartilage transition zone, and menisci which had low signal intensity that appeared as dark voxels.

Three manual assistive segmentation tools were examined and ‘paint with threshold’ was found to be most time efficient when threshold painting was used in conjunction with multi-slice selector tool. All the bones (Femur, Tibia, Patella and Fibula, their respective AC, meniscus, the cruciate ligaments, collateral ligaments and the patella ligament were segmented. However, as these were segmented on MR scan data with a different cropped volume, the model coordinates differed to those of this model and their positions could not be referenced properly. Hence, the ligaments were not included in this model. Future models should have all tissues of interest, segmented from the same set of cropped MR scan data.

Although fully automated segmentation of the various knee soft tissues is not currently possible, it is believed that there will be a possibility in the future, with

the use of techniques such as machine learning, segmentation algorithms could be taught to look for patterns in MR image scan data of the knee and decide based on probability.

Furthermore, the MR scan data used for this project are of live humans. It was therefore, not possible to dissection the individual segmented tissue for comparison with the segmented volumes. The accuracy and possible errors introduced during the segmentation process could not be quantified. It is recommended that a segmentation study be carried out with cadavers in the future for quantifying the accuracy of the proposed method.

Resampling of the data was necessary and was done after segmentation, to prevent loss of voxel greyscale information during delineation of the tissues. This was particularly important for tissues with thinner sections, such as AC, menisci and ligaments, which are already only represented by a few voxels in the original scan data resolution. The process of data resampling was found to introduce errors in the volume and surface area of the segmented tissue. Volumetric and surface area percentage errors were found to be highest for the menisci. As demonstrated in Chapter 2 and Chapter 3, variations in the size and geometry of the meniscus and articular cartilage have a significant effect on FE predictions. It is therefore concluded that the use of alternative non-voxel based meshing algorithms should be explored.

The enhanced surface feature based marching cube- voxel hybrid meshing algorithm, +FE Free, was used for meshing all of the tissue geometries. Compound coarseness in conjunction with mesh refinement for the AC masks generally provided meshes with good quality. The use of mesh refinement also allowed a higher percentage of the total number of elements in the model to be in the region of interest, thereby, increasing the mesh density in the area for better mesh performance. However, occasionally meshes contained a few elements with poor

mesh quality. In these cases, compound coarseness control could not be used and small adjustments of the advanced meshing parameters were required. It was noted that decreasing the value difference between the target minimum edge length and the maximum edge length improved the in-out aspect ratio of the elements. The advanced parameters used for meshing the femur-femoral AC and the tibia-tibial AC are presented in Table 4.2.

Table 4.2 Advanced parameters used for meshing the femoral and tibial parts.

Parameter	Femur	Tibia
Target minimum edge length (mm)	7	9
Maximum edge length (mm)	9	11
Target maximum error (mm)	1	0.09
Surface change rate	62	100
Target no. of elements across a layer	0.5	2
International change rate	30	67
Quality optimization cycles	8	8

Some consideration for compatibility between the meshing options in Simpleware and the model manipulation and definition methods in ABAQUS were required. In order to allow the tissues to be translated in relation to each other, the femoral part (femur and femoral AC), tibial part (tibia and tibial AC) and the menisci needed to be exported as separate models. Details are provided in Section 4.3.5.

Mesh convergence was not performed due to the difficulty in obtaining a mesh without any bad quality elements. Only one bad quality element is needed to prevent the whole FE model from being solvable. A systematic variation of compound coarseness to generate several solvable meshes of different mesh density was not possible. Small alterations to the region for mesh refinement and the amount of mesh refinement had to be adjusted to obtain a solvable mesh. This

alters the total number of elements inconsistent. Furthermore, mesh densities in the mesh refinement region varied gradually and therefore, was difficult to classify as a mesh of a particular density. This made performing a mesh convergence study difficult and hence, the effect of meshing on the model output was not performed in this project.

4.5 Acknowledgments

Work on MR imaging scan sequence optimization and scan data acquisition of the healthy knee was conducted in conjunction with studies undertaken by Dr. Gemma Whatling, Dan Watling and Peter Hobden.

4.6 References

[1] R.H. Hashemi, W.G. Bradley Jr. and C.J. Lisanti, 'MRI: The Basics 3rd edition', Wolters Kluwer, 2010

[2] F. Eckstein, H. Sittek, S. Milz, R. Putz and M. Resier, 'The morphology of articular cartilage assessed by magnetic resonance imaging (MRI). Reproducibility and anatomical correlation', Surg Radiol Anat, 16(4): 429-38, 1994

[3] F. Eckstein, H. Sittek, S. Milz, E. Schulte, B. Kiefer, M. Reiser and R. Putz, 'The potential of magnetic resonance imaging (MRI) for quantifying articular cartilage thickness – a methodological study', Clinical Biomechanics, 10(8): 434-440, 1995

[4] P.G. Young, T.B.H. Beresford-West, S.R.L. Coward, B. Notarberardino, B. Walker and A. Abdul-Aziz, 'An efficient approach to converting three-dimensional image data into highly accurate computational models', Philosophical Transactions of The Royal Society, Part A: Mathematical, Physical & Engineering Sciences, 366: 3155-3173, 2008

[5] J.M. Mansour, 'Biomechanics of Cartilage', Kinesiology: The mechanics and pathomechanics of human movement (Oatis, C.A., ed.). Lippincott Williams and Wilkins, Philadelphia, Ch. 5: 66-79, 2003

[6] G.C. Bessette, 'The meniscus', Orthopaedics, 15(1): 35-42, 1992

Chapter 5 Anatomy and microstructure of the meniscotibial ligaments

Held by a complex ensemble of ligaments working simultaneously, the translations and deformations of the menisci are important determinates of knee kinematics. Ligamental constraints of the menisci include the anterior and posterior horn attachments, the intermeniscal ligament (IML), meniscofemoral ligament (MFL), anterior meniscofemoral ligament (AMFL), posterior meniscofemoral ligament (PMFL), meniscotibial ligaments (MTLs) and deep medial collateral ligament (dMCL). Previous research has been carried out to better understand the microstructure and mechanical behaviour of the MFLs[1], IML[2], horn attachments[3 4 5] and the dMCL[6]. However, little has been found in the literature reporting on the microstructure and mechanical properties of the MTLs.

The MTLs are found on the outer periphery of the menisci. They attach the mobile menisci to the tibial plateau and are thought to play a significant role in menisci kinematics during knee loading. The knee model proposed by Yao et al.[7] is the first and only knee model published which has included the MTLs. With limited knowledge of the microstructure, anatomy and mechanical behaviour of the tissue, the MTLs were modelled based on best assumptions made for the orientation of the collagen fibres (CFs), thickness, length, stiffness and ligament pre-strain. CFs are known to align in the direction of mechanical loading. Assuming the function of the MTLs is to anchor the menisci to the tibial plateau, they have been represented in previous FE models using linear springs aligned parallel to the S-I axis[8].

Comparison of the FE predicted meniscal translation and deformation with that measured using MR imaging showed localized discrepancies in the anterior and

posterior regions of the menisci[8]. The authors attributed these discrepancies to several contributing factors, one of which included the unknown mechanical behaviour of the MTL. Yao et al. later published a paper with details of medial meniscus deformation and translation sensitivity to the stiffness of the MTLs under anterior loading[9]. It demonstrated that between models with MTL stiffness of 1MPa and 5MPa, there was a significant difference in meniscal translation, particularly in the anterior region. It can therefore be concluded that, inclusion of the MTLs and an understanding of their mechanical behaviour are important for accurate prediction of knee kinematics in FE models.

Arrangements of CFs have a profound effect on the mechanical behaviour of musculoskeletal tissues, such as AC[10], meniscus[11 12], bone[13] and ligaments[14 15]. The use of polarised light microscopy with Picrosirius Red staining to enhance the birefringence of collagen to study its arrangement began in the 1970s[16]. Picrosirius red is a combination of Sirius Red which stains tissue red and picric acid which prevents the staining of non-collageneous structures, making picrosirius red specific to collagen with only a few exceptions. These exceptions exhibit little birefringence and can easily be distinguished under polarised light microscopy. Junqueira et al. found that an estimated 120 Sirius red molecules bind parallel to the axis of each Type I collagen molecule[17] which results in a 700% increase in light intensity under polarised light[12]. With the use of circular polarised light microscopy and image analysis software, sophistication of this technique in the study of CF arrangement allows the identification of the collagen type, quantification of collagen content, thickness of the fibres based on the light hue emitted and their spatial distribution[18].

Based on the knowledge that Type I collagen is found in ligaments, tendons and menisci, it was hypothesised that the MTLs also contained Type I collagen and its fibre arrangement could be studied using crossed polarised light microscopy with birefringence enhancement using Picrosirius red staining. The aim of this study was

to assess the CF arrangement in MTLs, for validation of the current method of including MTLs in FE full joint contact knee model.

5.1 Anatomy of the meniscotibial ligaments

5.1.1 *Sample collection and preparation*

Five excised tibial plateaus as intact as possible (including menisci and MTLs) were obtained from Total Knee Replacement (TKR) surgery with ethical consent (approved by the Research Ethics Committee for Wales: 10/MRE09/28). Excised tissue was stored in Hank's Balanced Salt Solution (Invitrogen, Paisley, Scotland) at 4°C until dissection.

During extraction of the tibial plateau in TKR surgeries, damage may be caused to the excised tissue. Therefore, only 'as intact as possible' samples could be collected (Figure 5.1). State of the tibial plateau, such as degeneration of the menisci, articular cartilage and surgical damage to the menisci were recorded. Fat deposits and the cruciate ligaments were first removed from the samples to reveal the menisci and its tibial attachments (Figure 5.2). The menisci were then gently lifted away from the tibial plateau to examine areas where peripheral attachments to the plateau are present (Figure 5.3, 5.4 and 5.5).

5.1.2 *Results*

In sample 1, MTLs were observed in the medial posterior region and the lateral anterior region. As the medial meniscus was gently displaced in the anterior direction, a ligamentous structure which stretches over the medial tibial AC, attaching the medial meniscus to the tibial plateau was clearly observed (Figure 5.3). Similarly, as the lateral meniscus was displaced in the posterior direction, a firm attachment of the lateral meniscus to the tibial plateau along the entire anterior periphery of the lateral meniscus was observed (Figure 5.4). MTLs from

sample 1 were not collected as the patient suffered from additional autoimmune disease.

In sample 2, MTLs were found in the medial posterior region and the lateral anterior region, as seen in sample 1; though in comparison with sample 1, the MTLs in sample 2 extended further along both peripheries. The MTL was found to extend from the middle region to the posterior region on the medial side (Figure 5.5) and from the anterior region to the middle region on the lateral side (Figure 5.6), covering almost half of the outer edge of the menisci. Significant degeneration of the lateral meniscus was observed and fat deposits were found attached to the anterior part of the tibial plateau (Figure 5.2).

Sample 3 was found to have suffered severe degeneration. Calcified tissue was found in the posterior part of the medial meniscus and the tissue lacked the stiffness of healthy fibrous tissue. Only a small portion of the MTL was found at the lateral anterior portion with large amounts of fat on the outer surface.

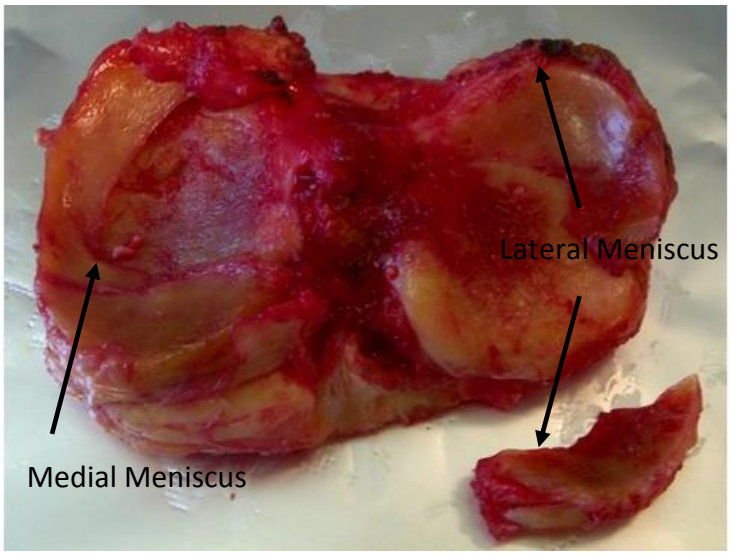

Figure5.1 'As intact as possible' excised tibial plateau from TKR surgery, sample 1 (right knee).

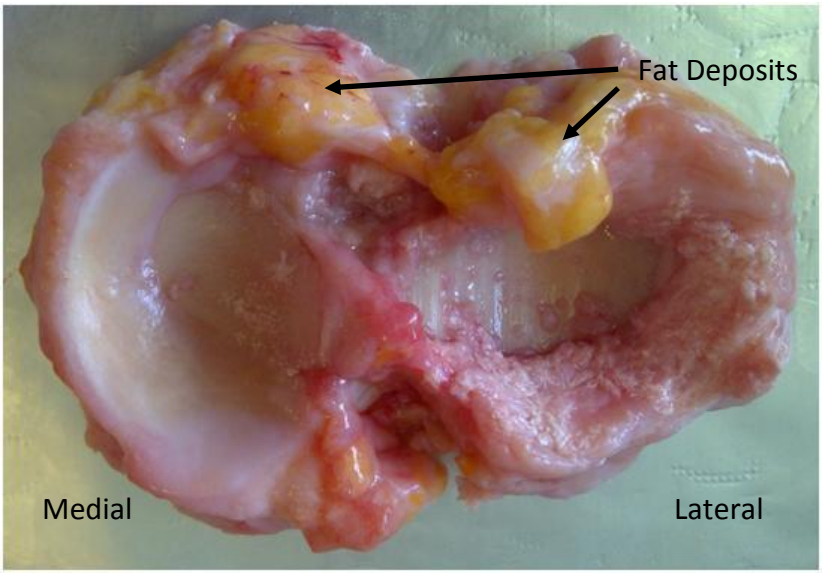

Figure 5.2 Excised tibial plateau, sample 2 (Right Knee). Significant degeneration of the lateral meniscus and fat deposits in the anterior region of the tibial plateau.

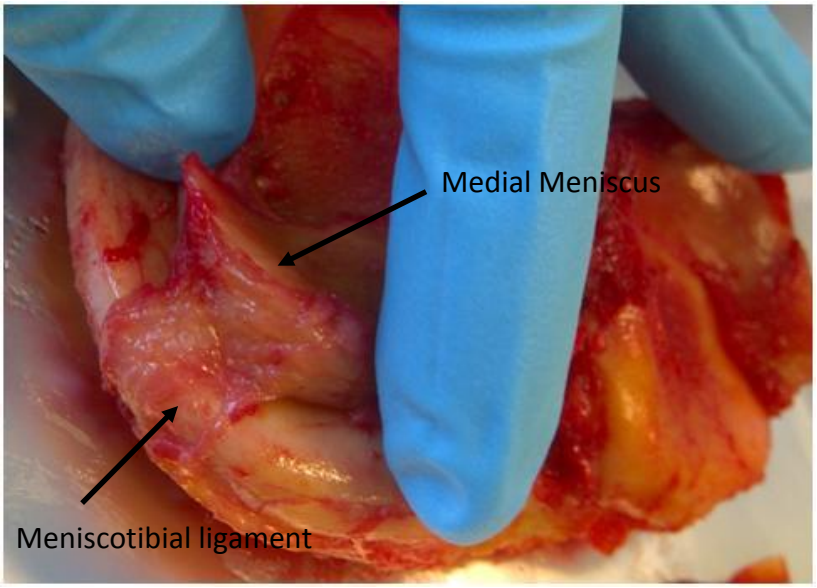

Figure5.3 Peripheral meniscal attachment found in the medial posterior region of sample 1.

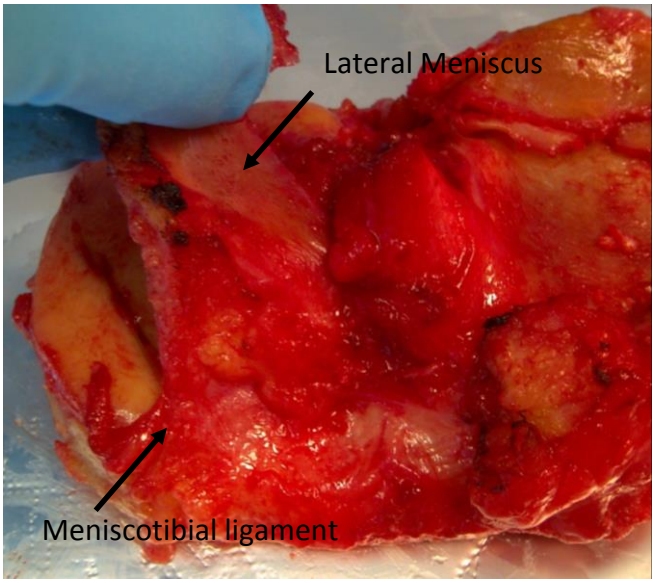

Figure 5.4 Peripheral meniscal attachment found in the lateral anterior region of sample 1.

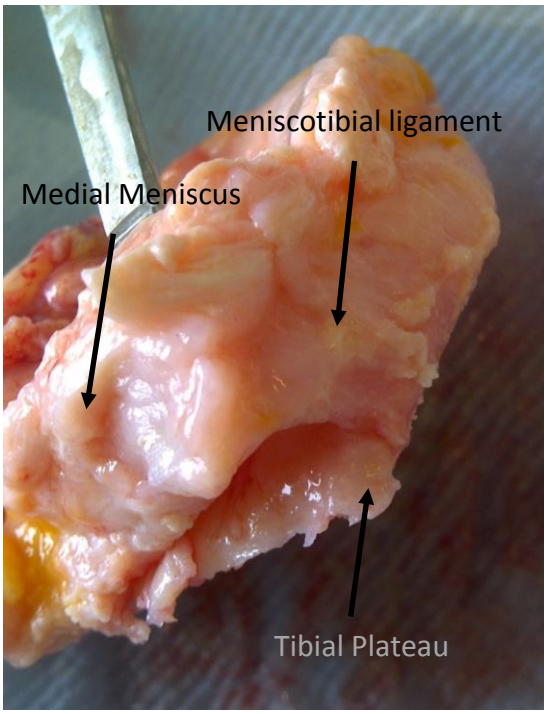

Figure 5.5 Peripheral meniscal attached found on the medial side of sample 2.

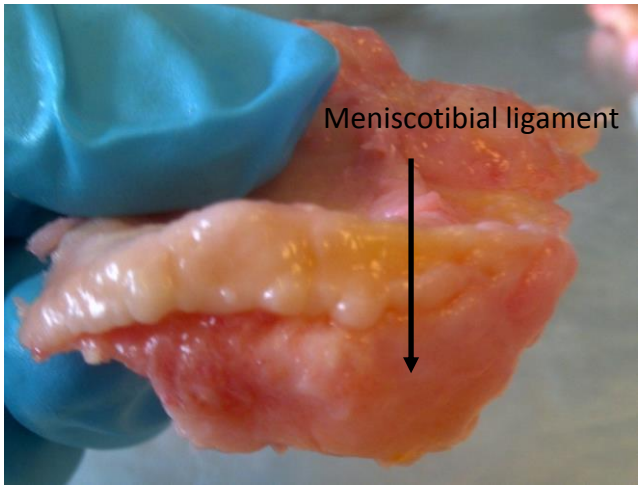

Figure 5.6 Peripheral meniscal attachment found on the lateral side in sample 2. The superior edge of the MTL originally attached to the periphery of the lateral meniscus has been resected. The inferior edge remains attached to the tibial plateau.

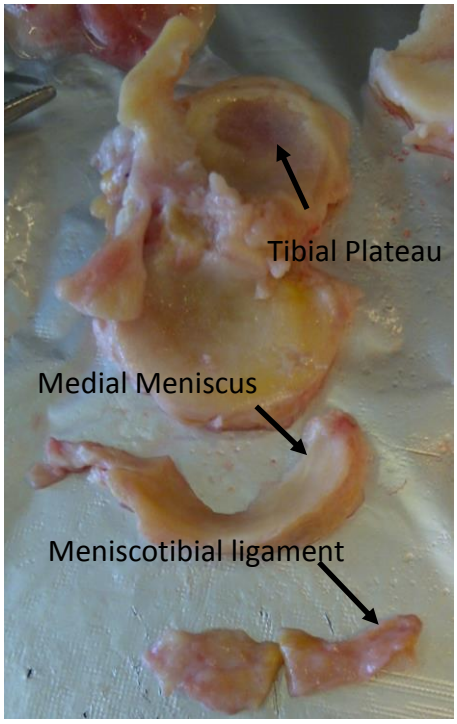

Figure 5.7 Excised tibial plateau, sample 4. MTL was found on the medial side. The harvested MTL was further dissected into two parts due to specimen size restriction for histological processing.

In sample 4, the lateral meniscus was heavily degenerated and was no longer of a normal rigid fibrous texture. In comparison, the medial meniscus tissue appeared relatively healthier. MTL was only found on the medial side extending from the periphery of the anterior region to the middle region of the meniscus (Figure 5.7).

The medial meniscus in sample 5 was found to be degenerated similar to the lateral meniscus found in sample 4. Severe damage was also noted in the medial tibial plateau. Although the lateral meniscus and plateau appeared to be relatively intact and healthy, no MTLs were found around both the medial and lateral meniscus.

Table 5.1 Summary of locations where MTLs were observed in each sample

	Medial	**Lateral**
Sample 1 (not collected)	Posterior	Anterior
Sample 2	Middle-Posterior	Anterior-Middle
Sample 3	-	Anterior
Sample 4	Anterior-Middle	-
Sample 5	-	-

5.2 Collagen fibre arrangement in meniscotibial ligaments

5.2.1 *Histology of the mensicotibial ligaments*

Peripheral attachments were removed from the menisci and the tibial plateau and placed in 95% ethanol for 24 hours prior to histology processing. The MTLs were placed in labelled petri dishes to facilitate identification of the histology slides orientation post histology processing (Figure 5.8). The MTLs collected were embedded in wax and sectioned at right angles to the ML axis, parallel to the SI-AP plane of the flattened MTL.

The histology slides were first de-waxed using 2 changes of xylene for 2 mins each. The slides were then rehydrated using alcohol and distilled water. The slides were submerged twice in 100% ethanol for 2 mins each, then 95% ethanol for 2 mins, 70% ethanol for 2 mins and finally in distilled water for 5 mins.

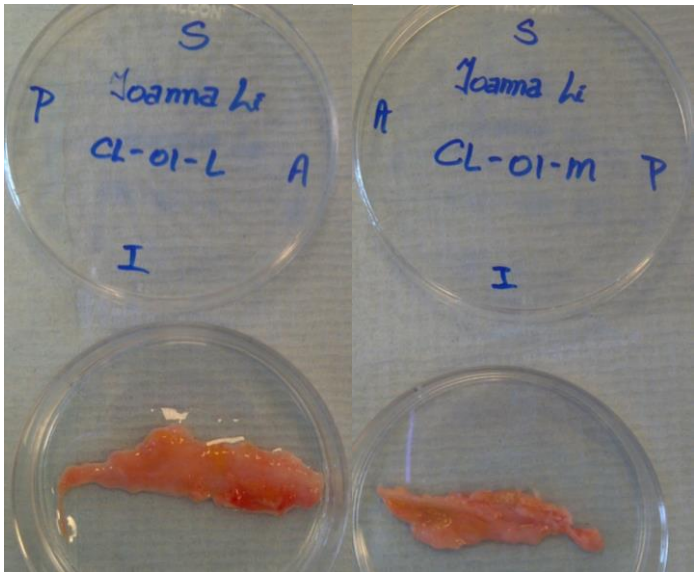

Figure 5.8 MTLs collected from the medial and lateral side of sample 2 (right knee).

Staining was carried out by immersing the slides in 0.1% Sirius Red (F3B) in saturated aqueous picric acid and incubated for 1 hour at room temperature and counter stained in Mayer's Haemalum working solution (Haematoxyline) for 5 mins.

The slides were then washed in tap water for 5 mins until no bleeding of the stains was observed and dehydrated with alcohol, by following the re-hydration protocol in reverse. Finally, cover slips were mounted with DPX and left to dry.

Crossed polarised light microscopy on the stained histology slides was carried out on a Zeiss microscope using a 6.3 x objective. The samples were orientated with the AP axis of the MTLs aligned parallel to the horizontal axis of the camera. Images were taken at five locations: anterior, posterior, inferior, superior and middle region of each ligament. The cross polarisers were then rotated between 0° and 180° to examine the orientation of the CFs.

Using photographs taken of the ligaments prior to histological processing, the location of each image relative to the reference axis of the knee were then determined and labelled as near horn, middle, superior and inferior regions, with reference to ligamentous regions near the anterior and posterior horn, at any

location between but not adjacent to the meniscal horns, near the meniscotibial-menisci interface and near the meniscotibial-tibia plateau interface respectively.

5.2.2 *Results*

In the near horn region, bright orange bands approximately 8µm in width running obliquely across the image were observed. Taken with the polarizing filter set at 0°, contrasting dark and bright adjacent bands were seen (Figure 5.9). It was also noted that bands which were observed as bright orange in the polarizing light microscopy image taken with the polarizing filter set at 0° (Figure 5.9), appear dark in the polarizing light microscopy image taken with the polarizing filter set at 45° (Figure 5.10) and vice versa for bands which appear dark in Figure 5.9.

In the middle region, bands of CF bundles with crimping were observed (Figure 5.11 and Figure 5.15). In comparison to images taken at the near horn region (Figure 5.9), the bundles in the middle region were orientated transversely across the image. Comparison between Figures 5.12, 5.13 and 5.14 with the polarising filter set at 0°, 45° and 90° respectively, the light intensity of the CFs were lower in Figure 5.14. This indicates that the dominant orientations of the fibres are parallel to the plane of light vibration with the filter set at 90°, which is parallel to the horizontal axis of the image. Differences in light hue; green, yellow and orange, were observed and are due to variations in the thickness of the fibres[18]. Figure 5.15- Figure 5.17 and Figure 5.18-Figure 5.21 shows another two further sets of images of a MTL at the middle region without and with the polarising filters set at varying angles. Observations of CF orientation correlated well with those observed for the same presented in Figures 5.11-14.

In the inferior region, transversely orientated fibre bundles consistent with that noted for the middle region was also observed (Figure 5.22). Minimal light intensity was observed in the image taken with the polarising filter set at 0°, indicating that the CFs are orientated parallel to the plane of light vibration, which is parallel to the

vertical axis of the image, the SI axis in the frame of reference for the knee (Figure 5.23).The bright orange bands observed in other regions were also observed in the inferior region when the polarising filter was set at 45° (Figure5.24). This confirms the low light intensity in Figure 5.23 were not due to the lack of fibres but rather the alignment of the fibres to the plane of light vibration.

In the image of a MTL taken at the superior region, ligamentous fibroblast cells stained blue black by Haematoxylin were observed at the top half of the image (Figure 5.25). This is as expected in the transition region between the MTL and the meniscus. In the bottom half of the image taken at the superior region of a MTL, transversely orientated fibre bundles consistent with findings in other regions of the MTLs was observed (Figure 5.26 and Figure 5.27).

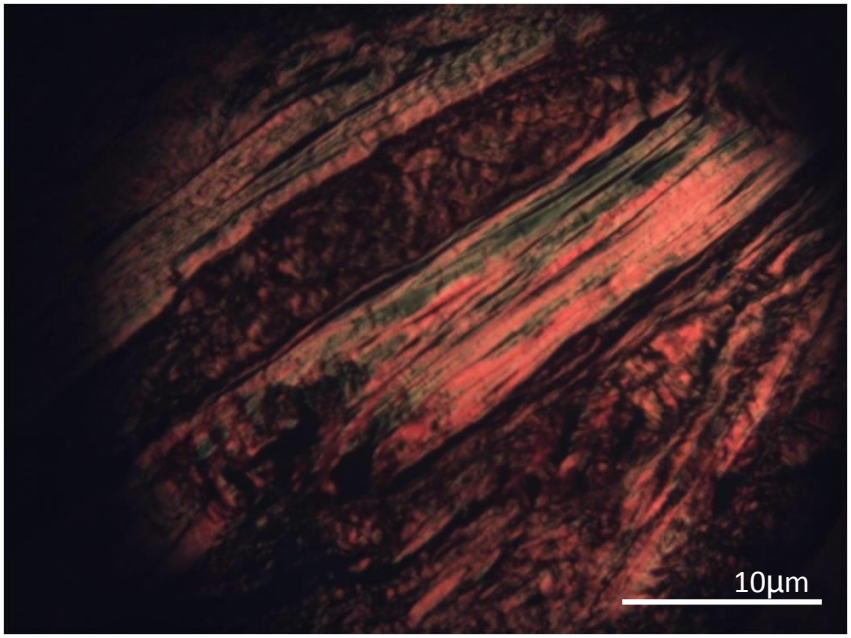

Figure 5.9 Polarising light microscopy image of a MTL at the near horn region with the polarising filter set at 0°.

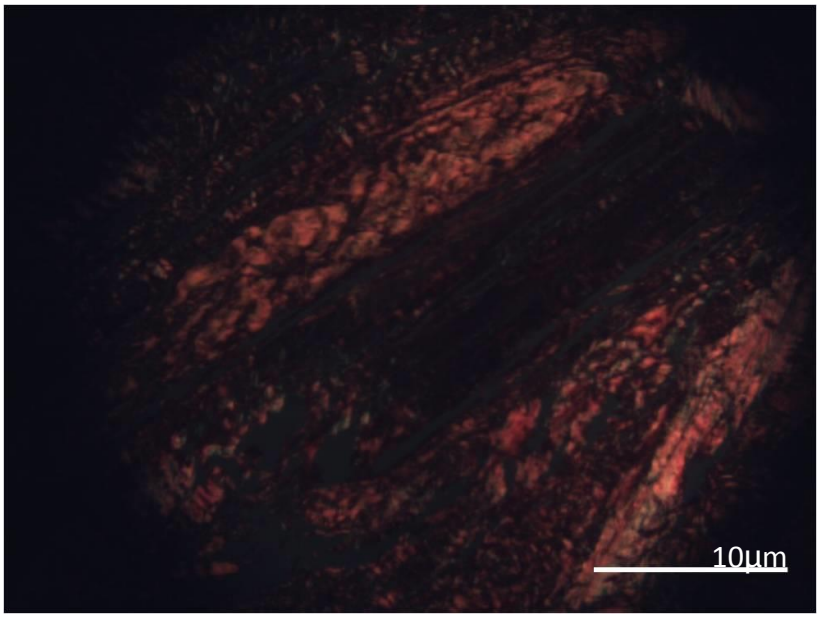

Figure 5.10 Polarising light microscopy image of a MTL at the near horn region, as presented in Figure 5.9, with the polarising filter set at 45°.

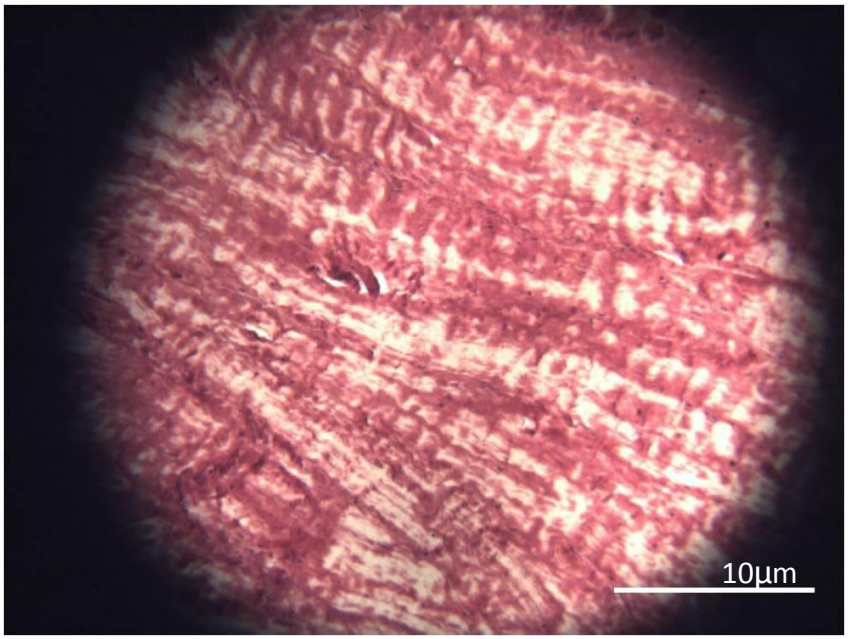

Figure 5.11 Light microscopy image of a MTL at the middle region with picrosirius red staining.

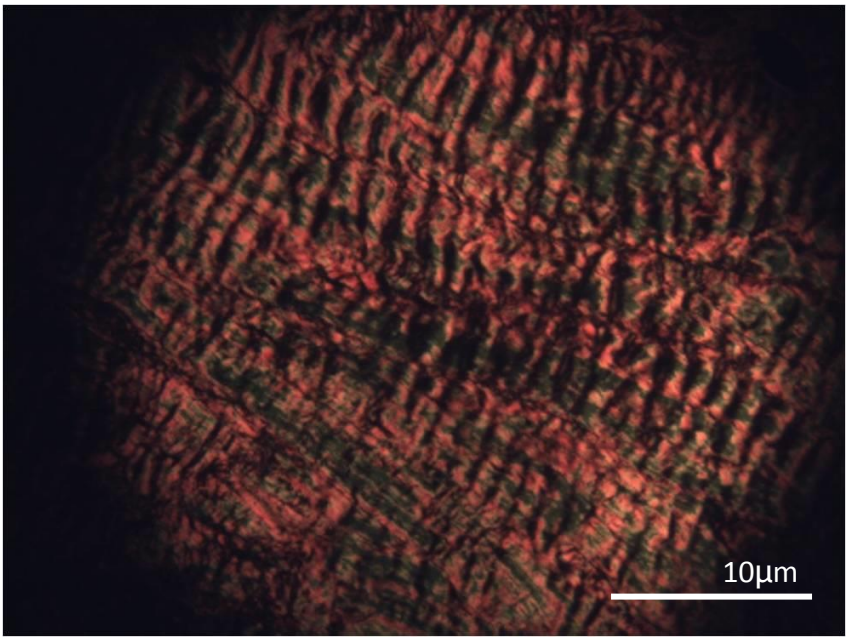

Figure 5.12 Polarising light microscopy image of a MTL at the middle region, as presented in Figure 5.11, with the polarising filter set at 0°.

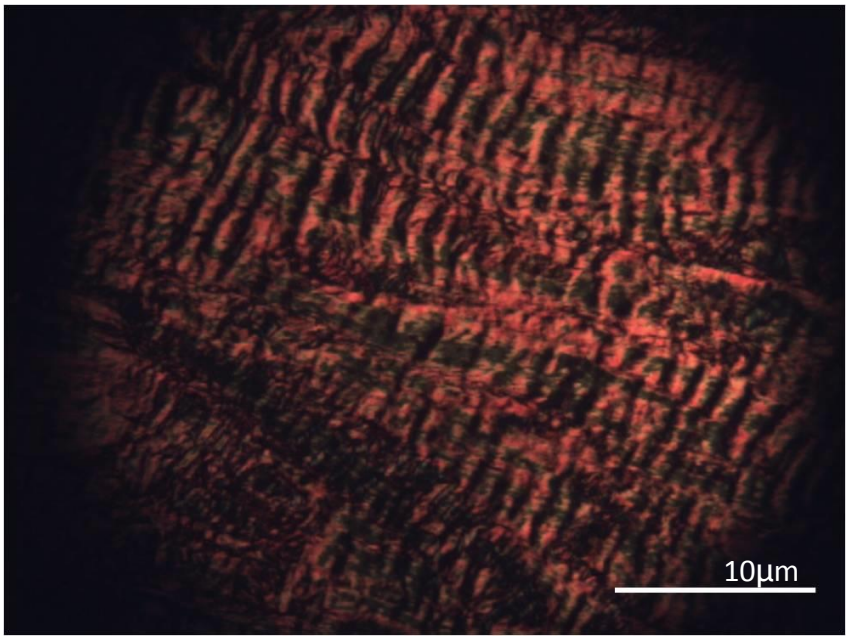

Figure 5.13 Polarising light microscopy image of a MTL at the middle region, as presented in Figures 5.11 and 5.12, with the polarising filter set at 45°.

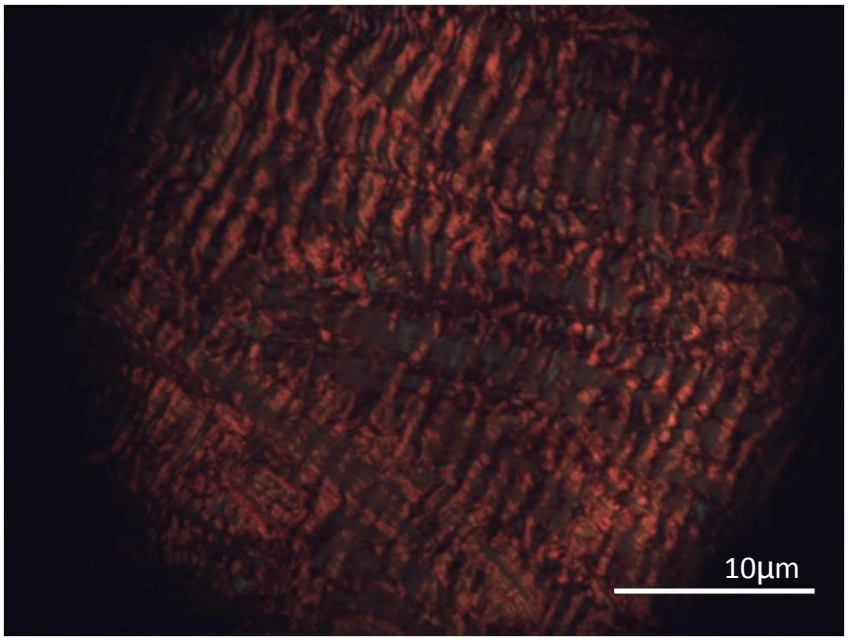

Figure 5.14 Polarising light microscopy image of a MTL at the middle region, as presented in Figures 5.11, 5.12 ad 5.13, with the polarising filter set at 90°.

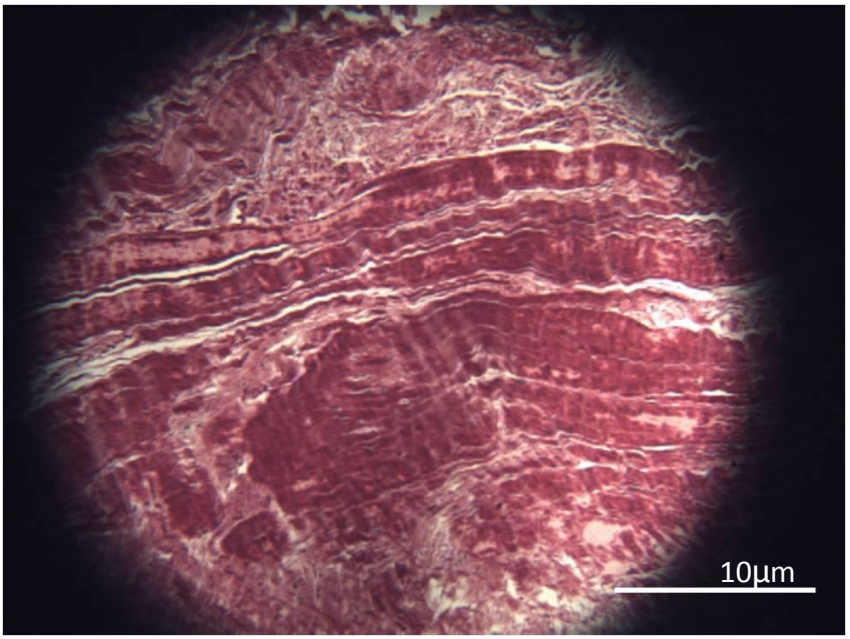

Figure 5.15 Light microscopy image of a MTL at the middle region stained with picrosirius red.

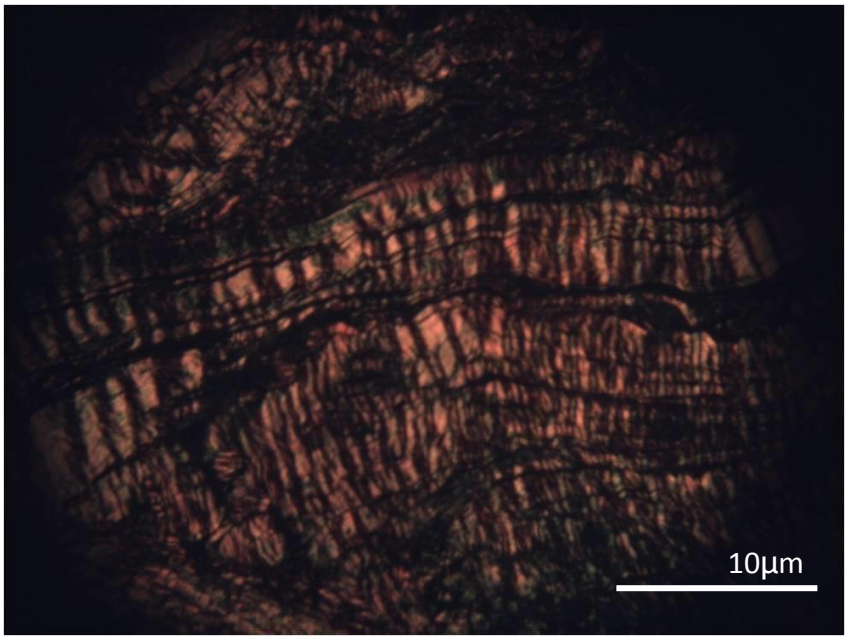

Figure 5.16 Polarising light microscopy image of the specimen presented in Figure 5.15, at the middle region of a MTL, with the polarising filter set at 0°.

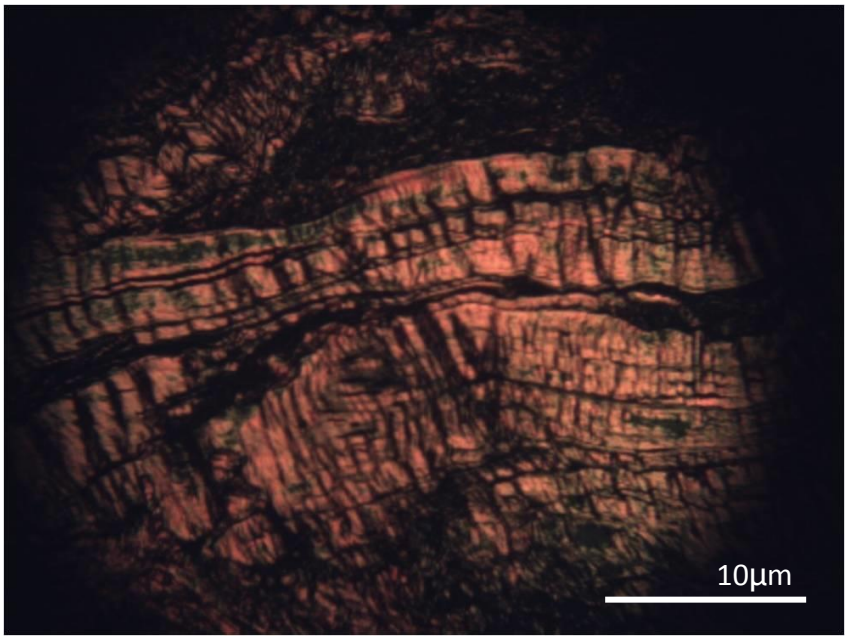

Figure 5.17 Polarising light microscopy image of a MTL at the middle region, as presented in Figures 5.15 and 5.16 with the polarising filter set at 45°.

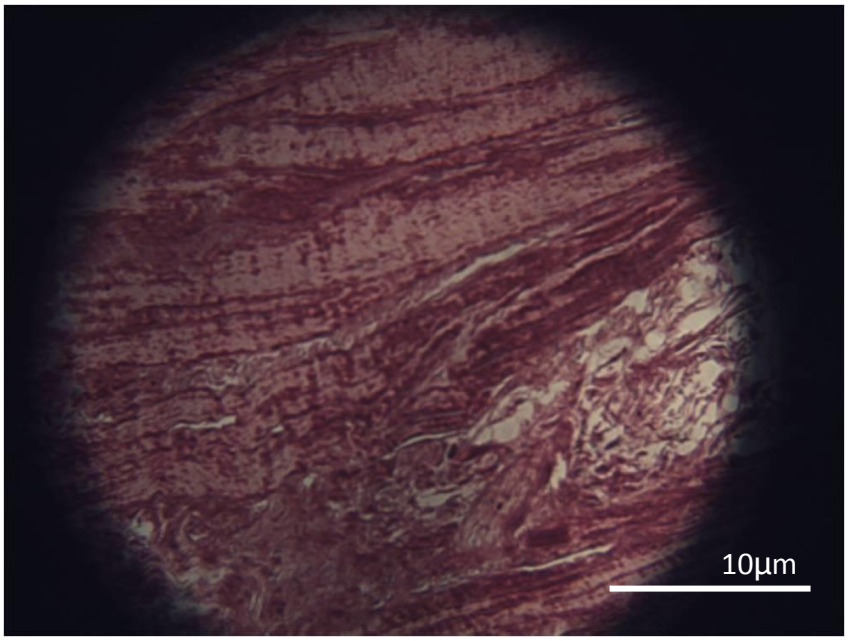

Figure 5.18 Light microscopy image of a MTL at the middle region stained with picrosirius red.

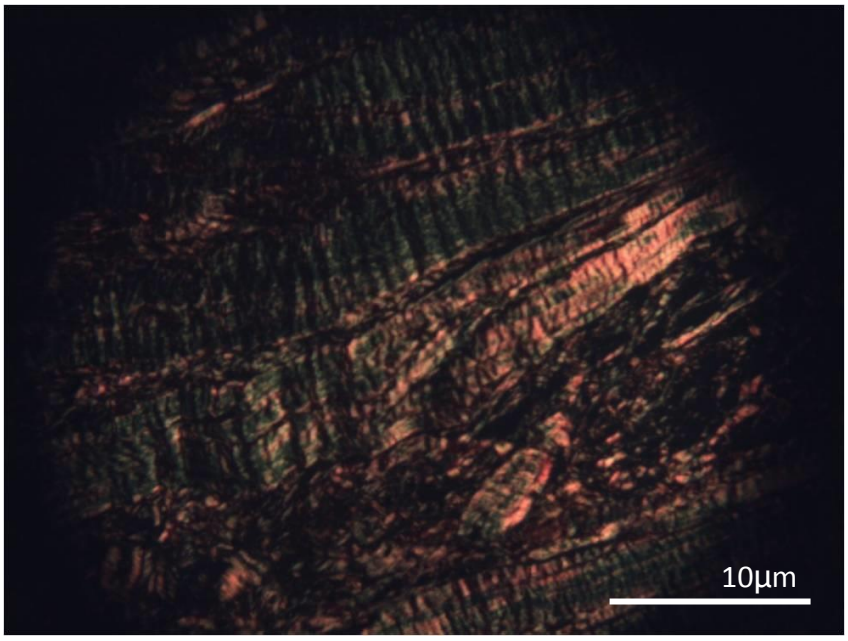

Figure5.19 Polarising light microscopy image of the specimen presented in Figure 5.18, at the middle region of a MTL with the polarising filter set at 0°.

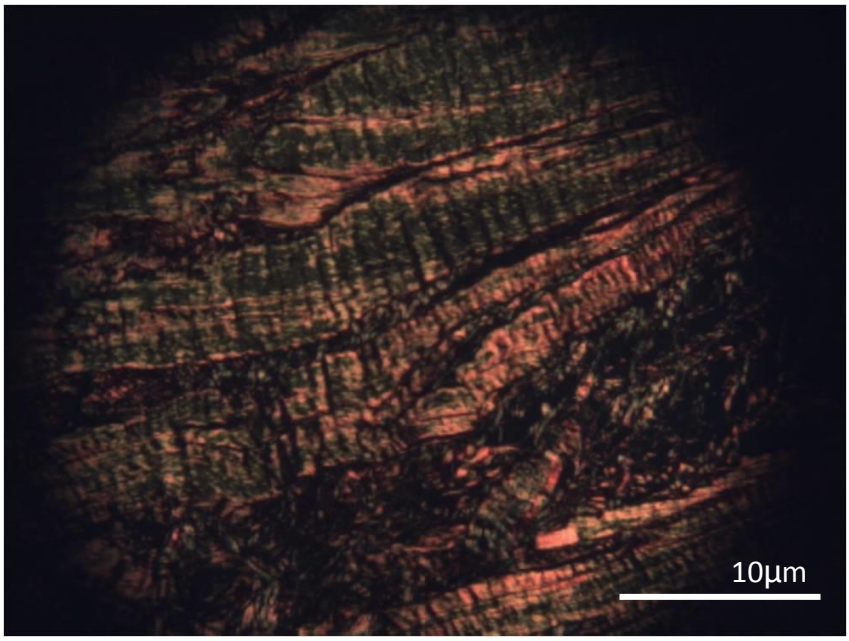

Figure 5.20 Polarising light microscopy image of a MTL at the middle region, presented in Figures 5.18 and 5.19 with the polarising filter set at 45°.

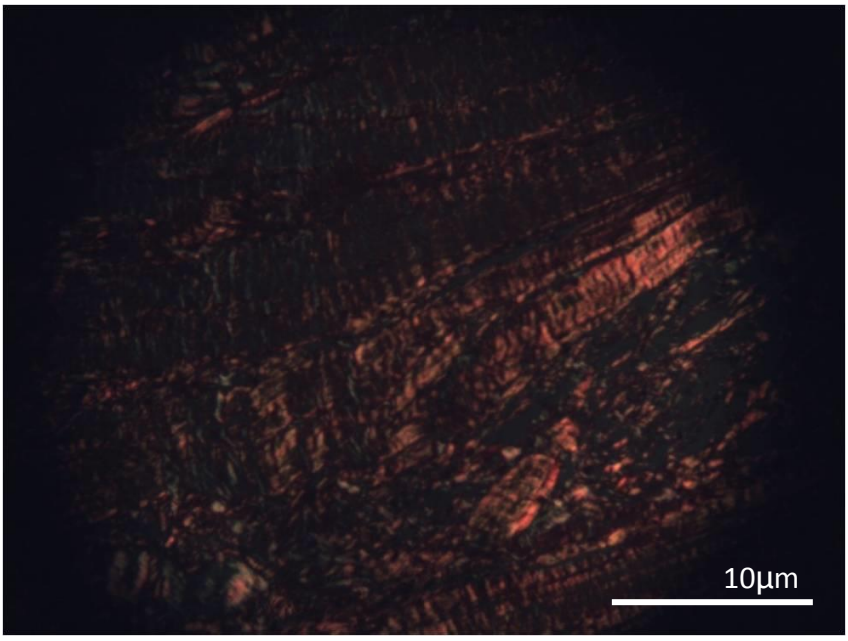

Figure 5.21 Polarising light microscopy image of a MTL at the middle region, presented in Figures 5.18, 5.19 and 5.20, with the polarising filter set at 90°.

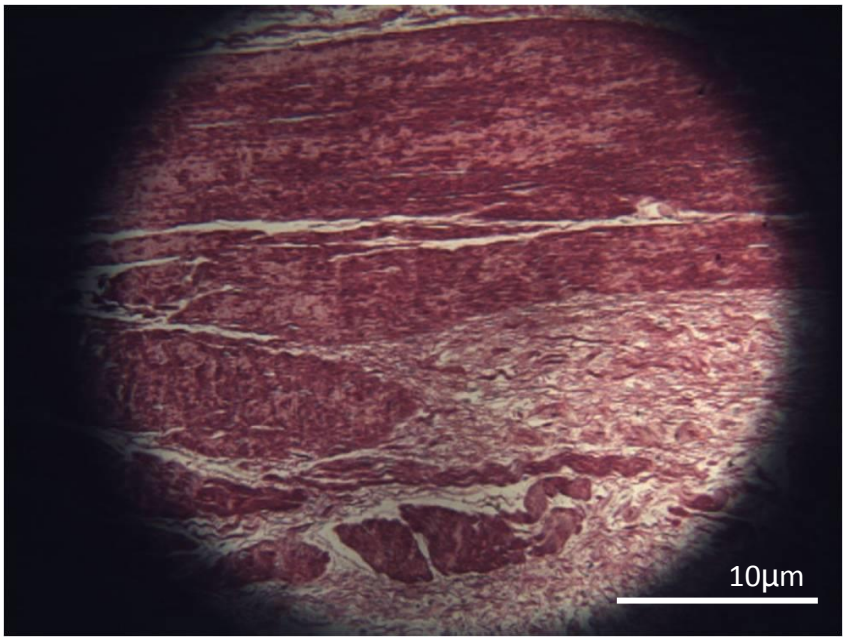

Figure 5.22 Light microscopy image of a MTL at the inferior region stained with picrosirius red.

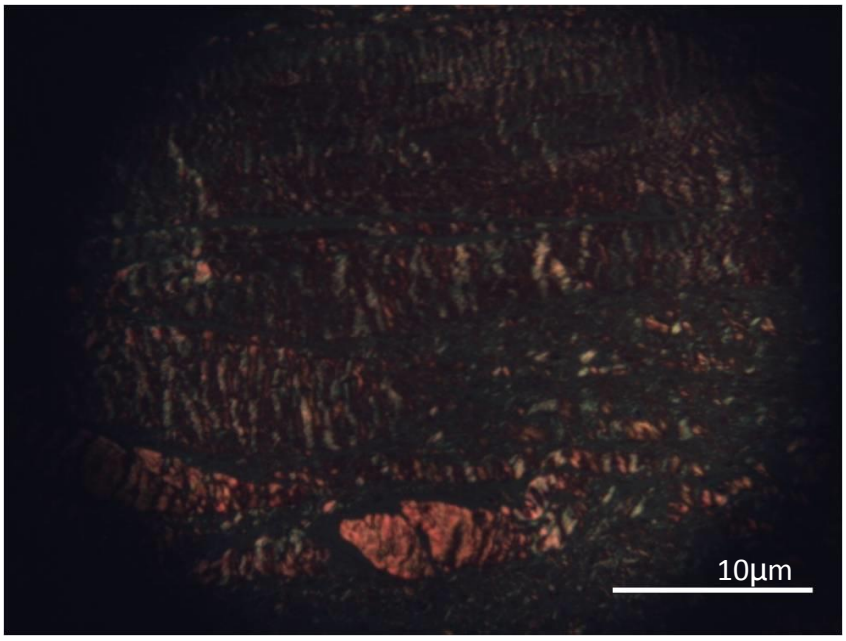

Figure 5.23 Polarising light microscopy image of the specimen presented in Figure 5.22, a MTL at the inferior region, with the polarising filter set at 0°.

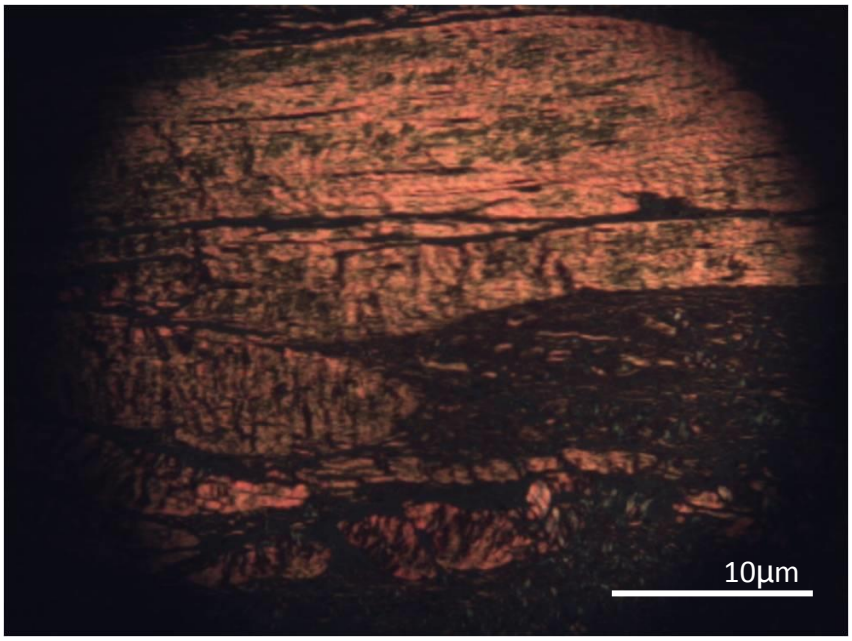

Figure 5.24 Polarising light microscopy image of the specimen presented in Figure 5.22, a MTL at the inferior region, with the polarising filter set at 45°.

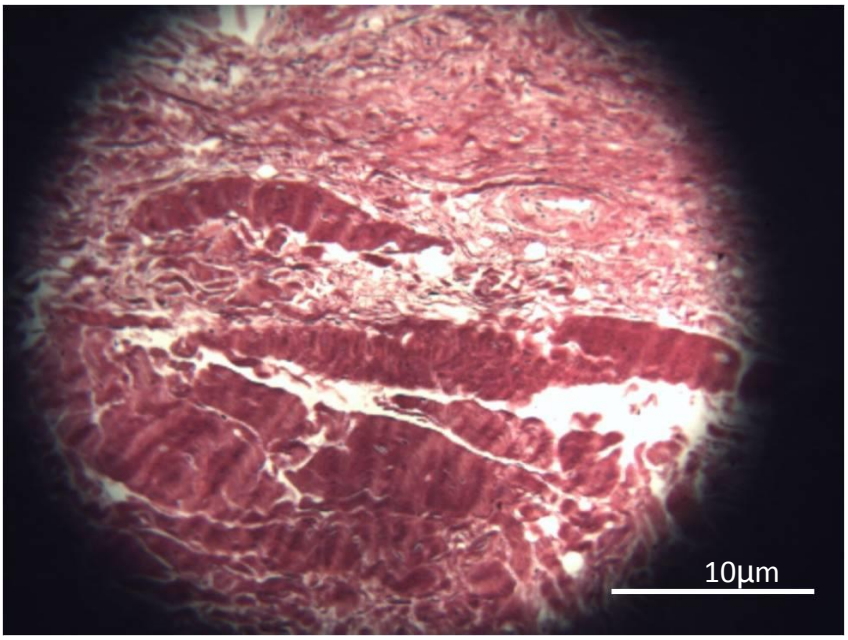

Figure 5.25 Light microscopy image of a MTL stained with picrosirius red at the superior region, the MTL-meniscus interface.

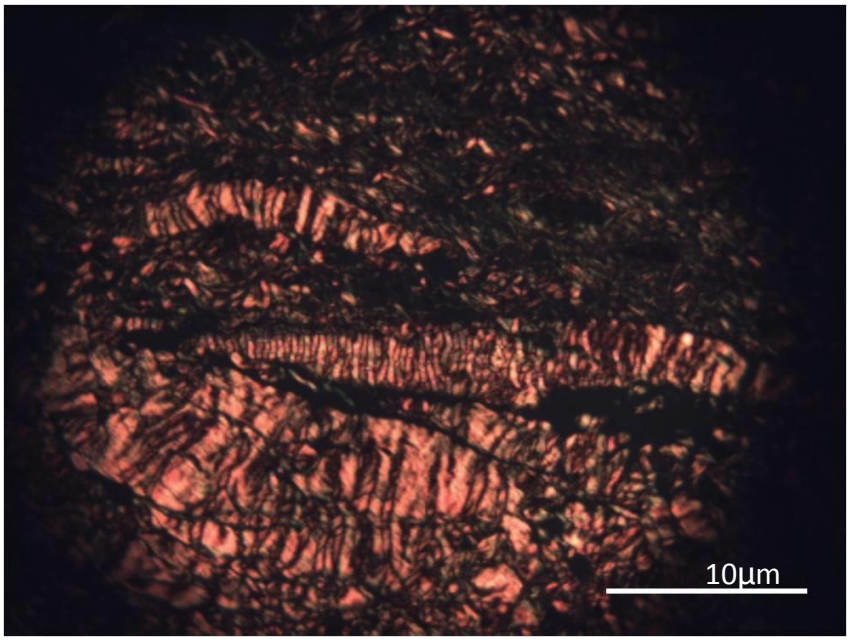

Figure 5.26 Polarising light microscopy image of the specimen presented in Figure 5.25, at the superior region of a MTL, with the polarising filter set at 0°.

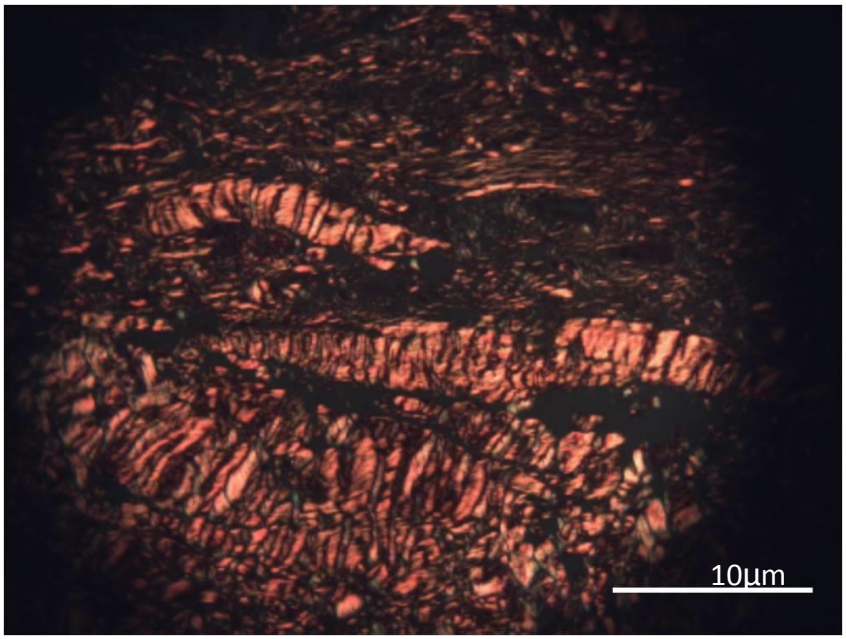

Figure 5.27 Polarising light microscopy image of the specimen presented in Figures 5.25 and 5.26, at the superior region of a MTL, with the polarising filter set at 15°.

5.3 Discussion

All five knee specimens collected were of the right knee and the presence of the MTL was noted in four of the specimens. This indicates that MTLs were found in 80% of the knee specimens collected for this study. This is a significantly higher percentage compared to the 23.53% found in a previous study[19]. However, it must be noted that the previous study was carried out using fixed cadaveric specimens. Due to the thinness of the MTLs, it is believed that the fixing process could damage the tissue and hence, lead to missed identification of the presence of the tissue. Differences in results between the two studies could also be due to a statistical error in this study, as it was only possible to collect five knee specimens. Another possible explanation could be that the knee specimens in this study were collected from TKR surgeries where patients displayed signs of OA, rather than healthy knee joints. A greater number of specimens to determine the true percentage of the population with MTLs and further studies will need to be carried out in order to investigate the relationship between MTLs and OA.

MTLs were found on the medial side in three out of the five specimens and the lateral side also in three out of the five specimens (Table 5.1). A single MTL spanning the entire periphery of the medial and lateral side was not found in any of the specimens collected. Instead, MTLs spanning regions of the tibial plateau periphery were observed. Around the medial meniscus, MTLs were found in the anterior, middle and posterior regions, whereas, MTLs were only found around the anterior and middle regions of the lateral meniscus (Figure 5.28).

In TKR surgery, the whole tibial plateau is removed from the affected joint, during which the menisci can be damaged (Figure 5.2). As a result, the MTL in these regions may sometimes be severed collaterally. Another potential cause of damage to the MTLs was in surgeries where the tibial plateau was cut above the attachment of the MTL. The inferior edge of the ligament attaches to the tibia plateau several

millimetres below the tibial articular cartilage and depending on the patient's case, the surgeon may have made the cut above or below the attachment point. In knee specimens and regions where no MTLs were observed, it was therefore not possible to determine whether the MTLs were initially or whether they were damaged upon removal from the patient. In the future, if possible, it would be beneficial to carry out an extensive anatomy study in the presence of MTLs using un-fixed non-OA cadavers.

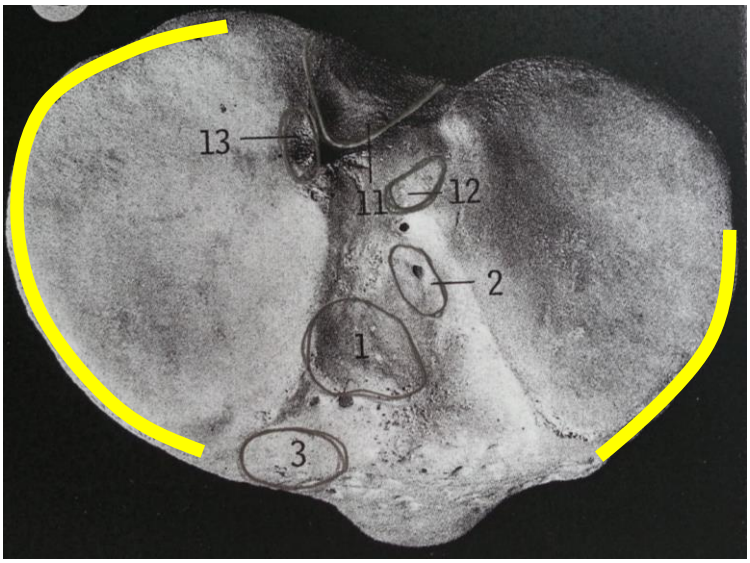

Figure 5.28 Image of the tibial plateau with attachment sites marked[20]. Anterior and posterior horn of the medial meniscus (3 and 13), anterior and posterior horn of the lateral meniscus (2 and 12), anterior cruciate ligament (1) and posterior cruciate ligament (11); Yellow indicates additional tibial plateau attachments, the MTL attachment sites, found in this study.

High light intensity bands ranging from 6-8µm were observed in the polarising light microscopy images from all regions of the MTLs. These high light intensity bands, which appear dark when the polarising filter is set at a certain angle, are believed to be CF bundles. The angle of the filter at which birefringence extinction happens is the angle of optic axis and therefore, indicates the orientation of the fibres.

The high light intensity bands were observed to be approximately 6-8μm in width, supporting the argument that the CF found in MTLs are Type I collagen which has been reported to be approximately 1-10μm in diameter[15].

CF bundles in all regions, except the near horn region, of all specimens were found to run dominantly parallel to the AP axis of the flattened MTLs, similar to the dominant circumferential fibre arrangement found in the meniscus.

In images taken of regions near the meniscal horns, the bundles were observed to run obliquely across the AP-SI plane of the flattened MTLs. Orientation of the fibres within the CF bundles were found to vary between the different regions. In the regions nearest to the mensical horns, large differences in areas with high and low light intensity were noted between images with the polarising filter set at 0° and 45°. The separate fibre bundles were noted to have high intensity at one angle and appear completely dark at another. It is therefore believed that the fibres within a collagen bundle in the regions nearest the meniscal horns are highly uniformly orientated.

In the middle region, crimping was noted in the fibre bundles, with the fibre bundle arrangement and organization were similar to that observed in the menisci[21]. Although differences between areas with high and low light intensity were noted, the contrast was comparatively less compared to that observed the near the horn regions. Some fibres were found to have high light intensity in each fibre bundle at each polarising filter angle. Light intensity for the fibres at 0° and 45° were comparable, although images with the filters set at 90° were significantly dimmer. It is therefore, concluded that fibre bundles in the middle region consist of fibres orientated at a variety of angles with a majority aligned parallel to circumferential fibres in the menisci. Compared to other regions, the CF bundles were found to be tightly packed and highly orientated.

Light intensity of the fibres in images with a polarising filter angle of 0° and 90° were found to be lowest for the MTL-tibia interface, although high light intensity was noted in the same regions in the image with a polarising filter angle of 45°. It is therefore believed that at the MTL-tibia interface, fibres in the transverse fibre bundles are orientated in two dominant directions; vertically, parallel to the SI axis and transversely, parallel to the circumferential fibres of the menisci.

At the superior region, at the MTL-meniscus interface, it was found that the light intensity of the fibres were comparable in all images with the polarising filter set at 0°, 45° and 90°. This indicates that the CFs in the transverse fibre bundles in the superior region are amorphously orientated.

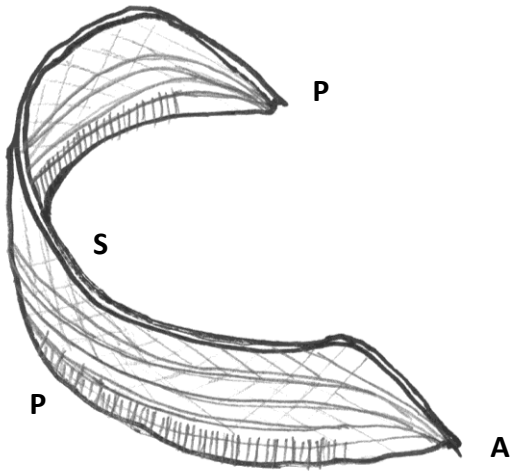

Figure 5.29 Diagram illustrating fibre orientation in the anterior (A), posterior (P), superior (S) and inferior (I) regions in a medial meniscotibial ligament

CFs arrangements are known to align with the direction of loading. This has led to previous hypotheses that the fibre orientations in MTLs are aligned parallel to the SI axis to resist detachment of the meniscus from the tibial plateau. Although, the findings in this study are contradictory to previous assumptions, they are logically feasible. The MTLs are a membrane like material which attaches the periphery of the meniscus to the underlying bone, at the same time forming a cradle around the

meniscus. Comparable with the mechanics of the menisci where circumferential fibres resist the lateral expansion of the tissue under uniaxial loading, it is believed that the MTLs with fibres arranged parallel to the circumferential further reinforces the structure with some fibres arranged in other orientations to resist excessive motion in all six DOFs of the mobile menisci. Furthermore, the SI axis aligned fibres found in the inferior region assist in anchoring the tissue to the tibia and resist the pulling away of the MTL itself from the plateau.

5.4 Acknowledgement

The School of Biosciences Histology Unit of Cardiff University carried out histology processing of the slides.

5.5 References

[1] H.O. Amadi, C.M. Gupte, D.T. Lie, I.D. McDermott, A.A. Amis and A.M. Bull, 'A biomechanical study of the meniscofemoral ligament and their contribution to contact pressure reduction in the knee', Knee Surgery, Sports Traumatology, Arthroscopy, 16(11): 1004-1008, 2008

[2] S.-Y. Poh, K.-S. A. Yew, P.-L. K. Wong, S.-B. J. Koh, S.-L. Chia, S. Fook-Chong and T.-S. Howe, 'Role of the anterior intermeniscal ligament in tibiofemoral contact mechanics during axial joint loading', The Knee, 2011, doi:10.1016/j.knee.2010.12.008

[3] K. Messner and J. Gao, 'The menisci of the knee joint. Anatomical and functional characteristics, and a rationale for clinical treatment', Journal of Anatomy, 193: 161-178, 1998

[4] M. Benjamin, E.J. Evans, R. Donthineni Rao, J.A. Findlay and D.J. Pemberton, 'Quantitative differences in the histology of the attachments zones of the meniscal horns in the knee joint of Man', Journal of Anatomy, 177: 127-134, 1991

[5] D. F. Villegas, J.A. Maes, S.D. Magee, T. L. Haut Donahue, 'Failure properties and strain distribution analysis of meniscal attachments', Journal of Biomechanics, 40: 2655-2662, 2007

[6] T.L. Haut Donahue, M.L. Hull, M.M. Rashid and C.R. Jacobs, 'How the stiffness of meniscal attachments and meniscal material properties affect tibio-femoral contact pressure computed using a validated finite element model of the human knee joint', Journal of Biomechanics, 36(1): 19-34, 2003

[7] J. Yao, J. Snibbe, M. Maloney and A. Lerner, 'Stresses and strains in the medial meniscus of an ACL deficient knee under anterior loading: a finite element analysis with image-based experimental validation', Journal of Biomechanical Engineering, 128: 135-141, 2006

[8] J. Yao, A.D. Salo, J. Lee and A.L. Lerner, 'Sensitivity of tibio-menisco-femoral joint contact behavior to variations in knee kinematics', Journal of Biomechanics, 41: 390-398, 2008

[9] J. Yao, P.D. Funkenbusch, J. Snibbe, M. Maloney and A.L. Lerner, 'Sensitivities of medial meniscal motion and deformation to material properties of articular cartilage, meniscus and meniscal attachments using design of experiments methods', Journal of Biomechanical Engineering, 128: 399-408, 2006

[10] J.M. Mansour, 'Chatper 5: Biomechanics of cartilage', In Kinesiology: The mechanics and pathomechanics of human movements (Oastis, C.A. ed.), Lippincott Williams and Wilkins, Philadelphia, Ch.5, 66-79, 2003

[11] D.L. Skaggs, W.H. Warden and V.C. Mow, 'Radial tie fibers influence the tensile properties of the bovine medial meniscus', Journal of Orthopaedic Research, 12: 176-185, 1994

[12] D.C. Fithian, M.A. Kelly and V.C. Mow, 'Material properties and structure-function relationship in the menisci', Clinical Orthopaedics and Related Research, 252: 19-31, 1990

[13] S. Bakbak, R. Kayacan and O. Akkus, 'Effect of collagen fibre orientation on mechanical properties of cortical bone', Journal of Biomechanics, 44(1): 11, 2011

[14] A.I. Zhurov, G. Limbert, D.P. Aeschlimann and J. Middleton, 'A constitutive model for the periodontal ligament as a compressible transversely isotropic visco-hyperelastic tissue', Computer Methods in Biomechanics and Biomedical Engineering, 10(3): 223-235, 2007

[15] J.A. Weiss and J.C. Gardiner, 'Computational modeling of ligament mechanics', Critical Reviews in Biomedical Engineering, 29(3): 303-317, 2001

[16] L.C.U. Junqueira, G. Bignolas and R. R. Bretani, 'Picrosirius staining plus polarization microscopy, a specific method for collagen detection in tissue sections', Histochemical Journal, 11: 447-455, 1979

[17] M. Wolam and F.H. Kasten, 'Polarized light microscopy in the study of the molecular structure of collagen and reticulin', Histochemistry, 85: 41-49, 1986

[18] L. Rich and P. Whittaker, 'Collagen and picrosirius red straining: a polarized light assessment of fibrillar hue and spatial distribution', Brazillian Journal of Morphological Science, 22(2): 97-104, 2005

[19] F.S. Bezerra, J.N. Alves, M.A.S. Silva, E.T.L. Trajano, T.A. Ferreira, H.A. Vasconcellos and S.S. Valença, 'Quantitative and descriptive analysis of the meniscotibial ligament in human corpses', Brazilian Journal of Morphological Sciences, 24(4): 211-213, 2007

[20] P.H. Abrahams, R.T. Hutchings and S.C. Marks Jr., 'McMinn's color atlas of human anatomy 4th edition', London: Mosby, 1998, Print

[21] R.M. Aspden, Y.E. Yarker and D.W.L. Hukins, 'Collagen orientations in the meniscus of the knee joint', Journal of Anatomy, 140(3): 371-380, 1985

Chapter 6 Finite element knee model with meniscotibial ligaments

Due to the complexity of the human knee joint, inevitable assumptions and simplifications are required in any description of the real joint behaviour used in mathematical or computational models. The significance of these assumptions and approximations must be carefully examined for validity of the model. Previous published work on full joint contact finite element knee model has examined the validity of certain assumptions and simplifications, detailed in Chapter 2 of this thesis. Using material properties (Table 6.1), contact definitions and boundary conditions from literature, a multipart contact finite element knee model has been developed for investigating the effects of different meniscotibial ligaments (MTLs) models and the MTLs stiffness on soft tissue predictions.

The development of the final full joint contact model was done progressively over three stages, which are detailed in sections 6.1-6.3. The three stages are:

i. Implementation of contact definitions according to those found in literature. A quasi-static model consisting of only the bones and AC with displacement controlled loading applied was developed.
ii. Incorporate menisci and investigate the use of a load controlled loading condition. This was done in anticipation for inclusion of patient specific knee loading data from musculoskeletal models.
iii. Examine the suitability of a. springs, b. bushing and c. membranes for the representation of MTLs in the full joint contact models. Using the model developed in stage 2, representation of the MTLs was included using three

different methods and the validity investigated. The use of a dynamic explicit solver for solving the FE knee model was explored in model iiib and iiic, for anticipation of the need to model dynamic events for validation against experimental data in the future.

Table 6.1 Summary of material properties taken from literature used for each model

<table>
<tr><th>Model</th><th>Bone</th><th>AC</th><th>Menisci</th><th>MTLs</th><th>Horns</th></tr>
<tr><td>i</td><td>E = 17.2GPa
v=0.3[3]</td><td rowspan="2">E = 5MPa
v = 0.45[14]</td><td>-</td><td>-</td><td>-</td></tr>
<tr><td>ii</td><td rowspan="4">Rigid</td><td rowspan="3">E_θ = 125MPa
$E_R = E_Z$ = 27.5MPa
$V_{R\theta} = V_{\theta Z}$ = 0.1
V_{RZ} = 0.33
$G_{R\theta} = G_{\Theta z}$ =2[7]</td><td>-</td><td>-</td></tr>
<tr><td>iiia.</td><td>k_{MTL}^{T}=20-200kN/mm</td><td rowspan="3">2kN/mm[1]</td></tr>
<tr><td>iiib.</td><td rowspan="2">E = 20MPa
v = 0.45
ρ =1[5]</td><td>1-5.5MPa</td></tr>
<tr><td>iiic.</td><td>E_1 = 600MPa
E_2 = 10MPa
E_3 = 5MPa
$v_{12} = v_{13}$ = 0.4
v_{23}=0.2
$G_{13=}G_{12}$=2</td></tr>
</table>

6.1 Contact definitions -Bone and AC quasi-static model

Every possible contact surface pair must be properly defined in a multipart contact model. In a model containing femur, tibia, femoral AC, tibial AC, lateral meniscus and medial meniscus, there are a total of 7 contact surface pairs. Each contact surface pair requires definition of the contacting surfaces on both parts and the type of interaction. Therefore, 14 surface sets needs to be defined for 7 contact surface pairs.

Interaction behaviour of the seven contact surface pairs can be categorised into two types of surface interactions. I. A fixed contact for the bone-AC interface and II. A frictionless no penetration contact between the menisci and AC.

Table 6.2 Summary of contacting surface pairs and Interaction type

Contacting surface pairs	Interaction type
Femur-Femoral AC	I
Tibia-Tibial AC	I
Femoral AC-Tibial AC	II
Femoral AC-Lateral Meniscus	II
Femoral AC-Medial Meniscus	II
Tibial AC-Lateral Meniscus	II
Tibial AC-Medial Meniscus	II

Type I: Fixed contact definition

A tie definition was used to define the interaction between contact pairs, femur-femoral AC and tibia-tibial AC, to ensure there are no relative displacements or rotations at the interface between the bone and their respective cartilage layer. This closely reflects the physiological contact behaviour of the AC and the underlying bone due to the anchoring collagen fibrils and rugged tidemark contour described in Chapter 2. The bone surface was defined as the master surface and the cartilage surface the slave surface of the interacting pair. The tie definition requires perfect conformity of the two surfaces defined and as a result the slave surface nodes within a predefined position tolerance of the master surface nodes are adjusted[2]. The value for the predefined position tolerance is arbitrary. In this model, a small value of 0.01mm was used to prevent distortion of the mesh and elements with aspect ratio outside the acceptance value.

Type II: No penetration frictionless contact definition

Cartilage-cartilage and cartilage-meniscus contact surface pairs were defined with frictionless finite sliding tangential behaviour, no penetration normal behaviour and are allowed to separate after contact. It was assumed that the low coefficient of

friction between tissues due to synovial fluid lubrication found in the knee joint, frictional effects are insignificant. Therefore, a frictionless definition is suitable.

The normal behaviour of 'no penetration' is governed by a definition relating contact pressure, P, and the amount of intersection between the two surfaces, h[5].

$$\begin{matrix} P = 0\ for\ h < 0 \\ h = 0\ for\ P > 0 \end{matrix} \qquad (6.1)$$

Correct implementations of the two types of contacts were examined first by inspection for penetration of the two meshes. Further confirmation was sought via the inspection of sensible FE predictions for nodal displacement, contact pressure, and compressive stress.

6.1.1 FE model details

The tibio-femoral quasi-static knee model without menisci had a total of 217,008 nodes, with 115,031 in the femur-femoral AC part and 101,977 in the tibia-tibial AC part. Meshed with quadratic tetrahedral elements, the model had approximately 600,000 DOFs and was solved using the ARCCA Linux cluster.

Tissue geometries and material properties

Both the bone and cartilage tissue geometries were reconstructed from patient specific MR imaging data using Simpleware Ltd. following the protocol detailed in Chapter 4 of this thesis. Bone was modelled as a deformable model, a linear elastic model with properties of E = 17.2 GPa and v=0.3[3]. For the purpose of examining validity of contact definitions, a detailed description of the anisotropic viscoelastic behaviour of AC was considered unnecessary. It was therefore modelled as a linear isotropic material with E = 5MPa, Poisson's ratio and v = 0.45[14].

Contact definitions

Type I contact definition was defined between the bone and cartilage interfaces for the femur and tibia. Type II contact definition was defined between the two contacting cartilage surfaces.

Boundary conditions

The femur-tibia kinematics were described as displacement and rotations of a free moving femur in relation to a fully constraint tibia with 0 DOFs. Displacement of all nodes in a rigid body is related to a single chosen node, called the reference node. In this model, the reference node was chosen to be at the centre of the proximal end of the femur. Loading conditions and 6 DOF definitions on these volumes were therefore, applied via the reference node. In the deformable tibia model, a total of four nodes were used to fully constrain the tibia. Three at the distal end of the tibia and one in the intercondylar region were assigned zero displacement and rotation for all DOFs.

Loading conditions

A displacement controlled uniaxial compressive loading in the SI-axis of 1.6mm was applied to the femur. Translation in the M-L axis and the A-P axis were restricted, however, the femur was allowed to rotate freely in the 3 rotational DOFs about the reference node, allowing the knee to find its natural position.

6.1.2 Results

The 3 degrees of rotation about the reference node on the femur relative to the femur translation in the SI axis has been plotted (Figure 6.5). Femur translation was corrected to be 0 at initial contact of the femoral and tibial AC.

The results show that during uniaxial compression, a small amounts of rotation of 0.1°-0.2° about the AP and SI axes, i.e. adduction-abduction and internal-external

rotation, was predicted by the model. Extension-flexion rotation predicted was negligible as expected under uniaxial compressive loading in the SI axis.

The 0.1°-0.2° rotations about the AP and SI axes under uniaxial compression loading are agreeable with previous passive knee movement studies[4] and are due to the femoral component coming into contact with the tibial component. The femoral component first comes into contact with the tibial component on the medial condyle. This initial contact causes the knee to undergo external rotation, as well as, adduction rotation, labelled stage 1 in Figure 6.1.

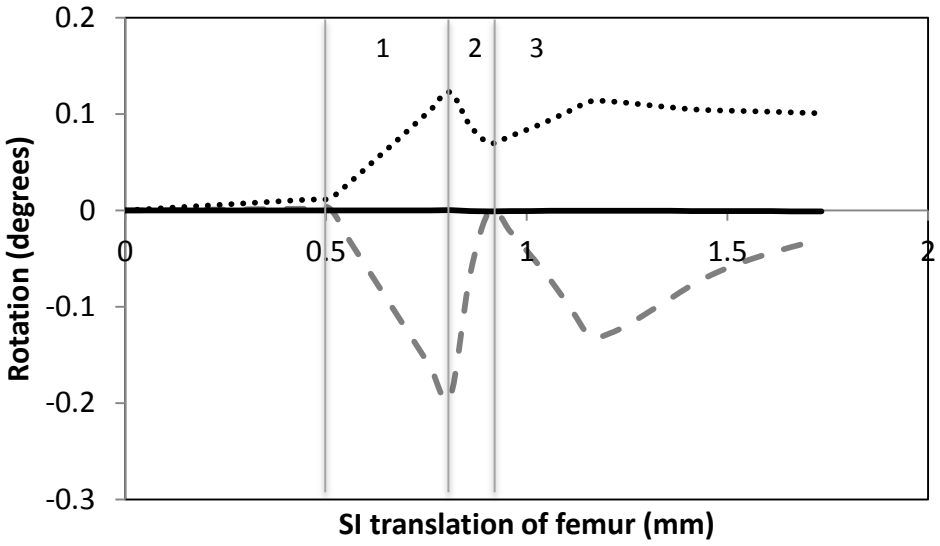

Figure 6.1 Graph of the 3 rotational DOFs plotted against SI translation for the femur. Black dotted line indicates internal (-ve) -external (+ve) rotation, grey dashed line indicates adduction (-ve) - abduction (+ve) rotation and black solid line indicates extension-flexion rotation.

The femoral component then comes into contact with the lateral condyle at stage 2, which causes the knee to rotate in the opposite direction towards its initial orientation. At the end of stage 2, the femoral AC is in full contact with the tibial AC. As the displacement increases in the SI axis, the small rotations are caused by introduction of new contact areas on the medial and lateral condyles (Figure 6.1).

In the nodal displacement contour plot, it can be seen that no movement were predicted for nodes in the tibia component. Displacement in the femur was predicted with a larger displacement of 2.38mm in the lateral condyle when compared to the medial condyle. This is due to the rotation of the femur (Figure 6.2). Zero displacement was predicted in the tibia and in areas of the tibial AC further away from the contact point, which is expected. Maximum nodal displacement of 0.55mm and 0.36mm has been predicted in the lateral and medial tibial AC respectively.

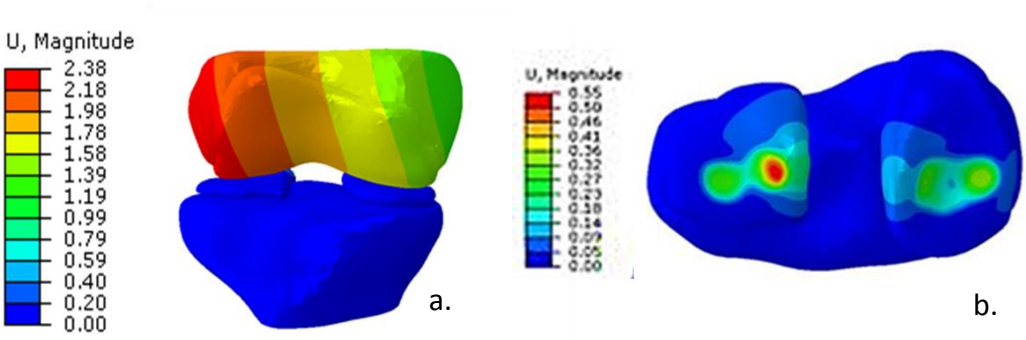

Figure 6.2 a. Contour plot of nodal displacement predicted b. in the tibial component with deformable AC and tibial.

Maximum contact pressure of 0.91MPa was predicted in the lateral femoral condyle predicted in regions corresponding to the contact areas between the femoral AC and tibial AC, during 1.6mm displacement controlled uniaxial loading. The average contact pressure predicted was approximately 0.53MPa on the medial and lateral condyles. Areas not in contact have zero contact pressure as expected (Figure 6.3).

For the femoral AC, a maximum compressive stress of 0.82MPa was predicted in the lateral condyle where maximum contact pressure was also predicted. The average compressive stress predicted in areas of contact was approximately 0.39MPa. Areas not in contact with the tibial component have negligible compressive stress as expected. In the tibial component, significant compressive

stress has been predicted in the intercondylar area where the zero translation and no rotation nodal constraint have been applied for restricting movement of the tibia. Maximum compressive stress of 0.74MPa was predicted in the lateral tibial AC and 0.56MPa as predicted in the medial tibial AC (Figure 6.4).

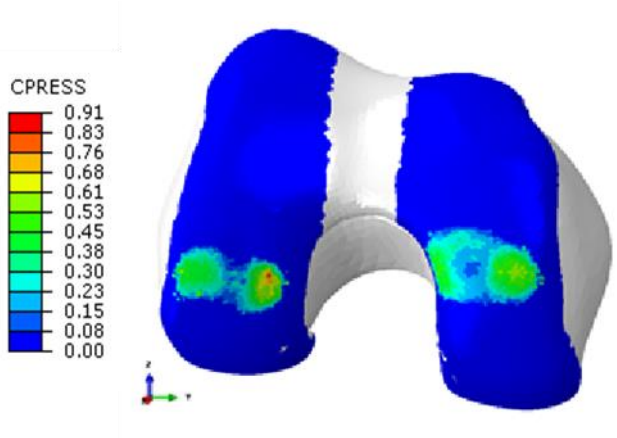

Figure 6.3 Contour plot of contact pressure predicted on the femoral AC induced by contact with tibial AC.

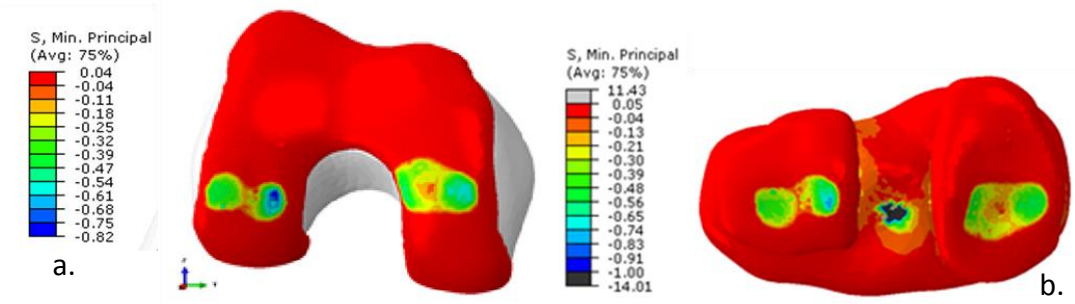

Figure 6.4 Contour plot of minimum principal stress predicted a. in femoral AC b. the tibial component

A contour plot of the minimum principal stress of a sagittal plane at contact point on the medial side shows transition of compressive stress through all the components into the tibia plateau (Figure 6.5). Maximum compressive stress was experienced in the region immediately adjacent to the contact area. With 0.37MPa predicted near the femoral and tibial AC contact and 0.1MPa predicted in the tibia

bone immediately below. The majority of the tibia bone experienced comparatively small compressive stresses in the range of 0.03MPa – 0.1MPa.

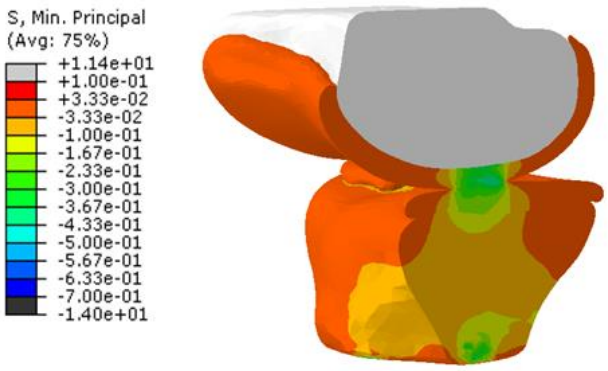

Figure 6.5 Contour plot of minimum principal stress, compressive stress, predicted in the femoral AC, tibial AC and tibia.

As detailed in the method, a very low position tolerance between the two surfaces with a 'tie' interaction property was assigned to avoid mesh distortions. However, the value of 0.01mm still caused mesh distortion issues and generated elements with unacceptable aspect ratios for the solver. It was found that method used in the mesh generation process to resolve mesh overlap and ensure mesh conformity, a position tolerance of 0mm can be used without intersection problems of the two surfaces. This eliminated the need for any adjustments of the slave surface mesh nodes and as a result, prevented distortion of the mesh and generation of poor aspect ratio elements.

6.2 Contact definitions -Bone, AC and menisci quasi-static model

Correct implementations of the additional contacts and loading conditions were examined in a similar fashion to model I, by inspection for sensible FE predictions for nodal displacement, contact pressure, and compressive stress; and ensuring no non-physiological behaviour was observed.

6.2.1 FE model details

The tibio-femoral quasi-static knee model with menisci was meshed with 168,346 quadratic tetrahedral elements with a total of 288,852 nodes. The deformable components, Femoral AC had 38,685 elements, lateral meniscus 7,215 and medial meniscus 8,634 elements. The model had approximately 100,000 DOFs

Geometries and material properties

Bone, cartilage and menisci tissue geometries were reconstructed from patient specific MR imaging data, same as that described in section 6.1.1.1. The femur and tibia were modelled as rigid bodies. AC was modelled as a linear isotropic material with E = 5 MPa and Poisson's ratio and v = 0.45. This value for young's modulus is comparable to those found in Chapter 3. However, it must be noted that in the explicit models, a higher young's modulus was used to avoid convergence problems[5].

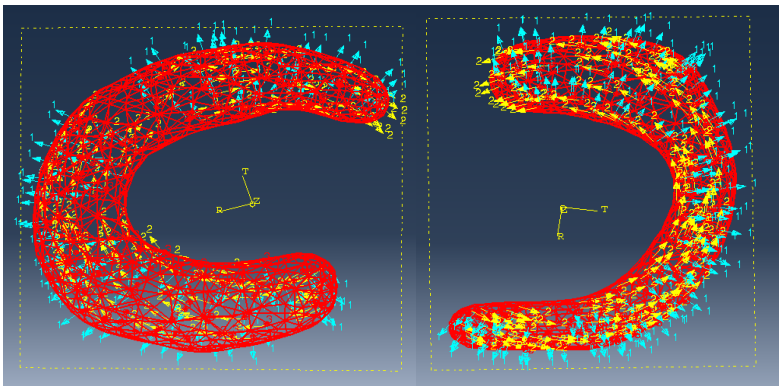

Figure 6.6 Material orientations assigned to the lateral and medial meniscus using local cylindrical coordinate systems for defining anisotropic material properties.

The menisci were modelled as anisotropic material with E_θ = 125MPa, $E_R = E_Z$ = 27.5MPa, $V_{R\theta} = V_{\theta Z}$ = 0.1, V_{RZ} = 0.33 and $G_{R\theta} = G_{\Theta z} = 2^6$ was assigned with material orientation defined using cylindrical coordinates. The origin was placed at the midpoint on the line projected in the transverse plane between the anterior and posterior horn. The R-axis and θ-axis was chosen to lie on the parallel to the

transverse plane of the mensici (Figure 6.1). The R-axis (blue arrows) was aligned in the same direction as the radial tie fibre orientation in the menisci and the θ-axis (yellow arrows) was aligned along the circumferential direction of the tissue, in the same direction as the dominant circumferential fibres found in the menisci.

Contact definitions

Type I contact definition was defined between the bone and cartilage interfaces for the femur and tibia. Type II contact definition was defined between the two contacting cartilage surfaces and between the articular cartilage and menisci.

Boundary conditions and Loading conditions

A force controlled uniaxial compressive loading of 1800N was applied at the reference node of the femur, matching loading conditions applied to a previously published model[7]. In this model, the femur was only permitted to translate freely in the superior-inferior axis. All DOFs for the tibia were restricted.

6.2.2 Results

In this model, the femur was restricted from any rotations. Nodal displacements in the femoral and tibial AC due to contact with the menisci and the opposite cartilage layer was observed (Figure 6.7). Rigid body motion of the femoral component must be subtracted from the nodal displacement to calculate the deformation due to the compressive loading. The maximum and minimum nodal displacements were 7.05mm and 6mm respectively. After correction for rigid body motion, maximum deformation in the femoral AC was calculated to be 0.7mm.

The contact area between femoral AC and tibial AC predicted in loading regime 2 were similar to those predicted in loading regime 1, where the femur was assigned free rotational DOFs. However, in the model where regime 2 was applied, larger deformation was observed in the femoral and tibial AC on the medial side compared to that of the lateral side (Figure 6.7). Maximum deformation of 0.75mm

and 0.48mm were predicted in the medial and lateral side for the tibial AC respectively. Zero nodal displacement was predicted in areas far away from the contact area. This is as expected.

At a compressive load of 800N, a maximum of 1.94 MPa was predicted in the menisci (Figure 6.8). Areas where contact pressure was predicted corresponded with areas on the femoral AC with significant deformation. As the load increased to 1800N, a compressive stress of 4-5 MPa was predicted in the femoral and tibial AC. Compared to the model without menisci, additional regions in the femoral AC and tibial AC anterior and posterior of the cartilage-cartilage contact point experienced significant compressive stress. These are the locations of the meniscal-cartilage contact (Figure 6.9).

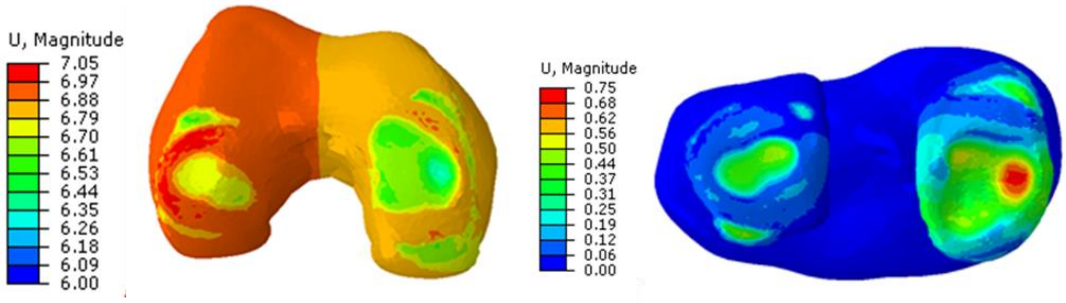

Figure 6.7 Contour plot of the nodal displacement predicted at 1200N compressive load a. in femoral AC b. in tibial AC

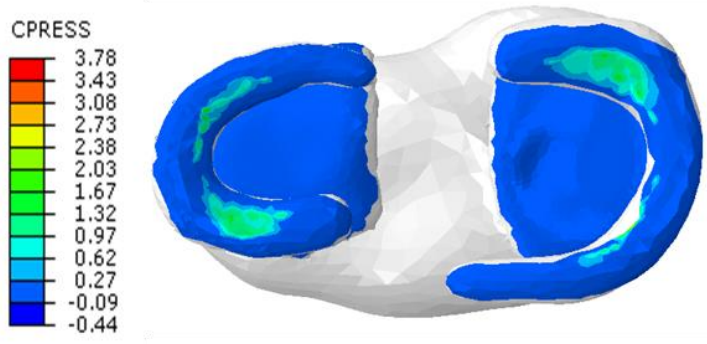

Figure 6.8 Contour plot of contact pressure predicted on the surface of the lateral and medial meniscus due to contact with the femoral condyle.

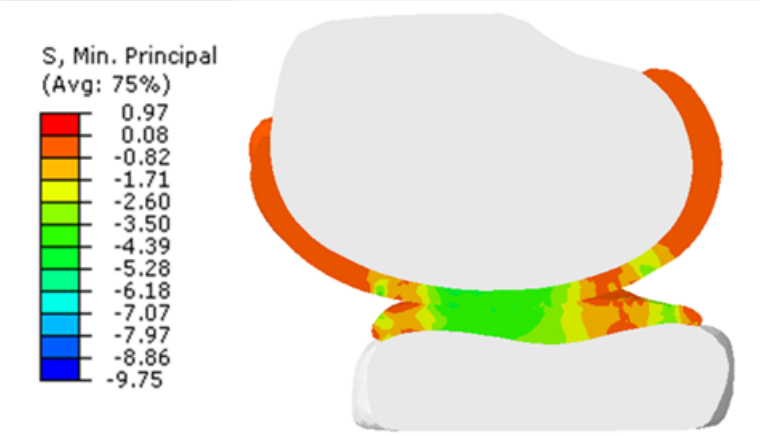

Figure 6.9 Compressive stress predicted in the femoral and tibial AC under force controlled compressive loading of 1800N.

6.3 MTL models

Method of modelling the MTLs with spring elements used in the only knee model with MTLs found in literature[6] was used for initial development of the model. Spring elements allow a force to be generated between two nodes due to their relative displacement. The relative displacement is calculated along the line projected between the two connected nodes[2].

$$\Delta u = \frac{(X_o^1 - X_o^2)(u^1 - u^2)}{\sqrt{(X_o^1 - X_o^2)(X_o^1 - X_o^2)}} \quad (6.2)$$

where u is the displacement, u^1 and u^2 are the displacement of the two nodes and X_o^1 and X_o^2 are the initial positions of the two nodes. This allows the direction of the applied force to rotate freely as the periphery of the menisci displaces in the 6 DOFs. The menisci were constrained via tensile spring elements to the tibial plateau representing the ligamentous constraints. The four meniscal horns (LA, LP, MA and MP) were modelled using 5 springs each with a total stiffness coefficient of 2kN/mm and the MTLs were modelled as 20 linear elastic spring elements spread evenly along the outer inferior edge of the menisci (Figure 6.10).

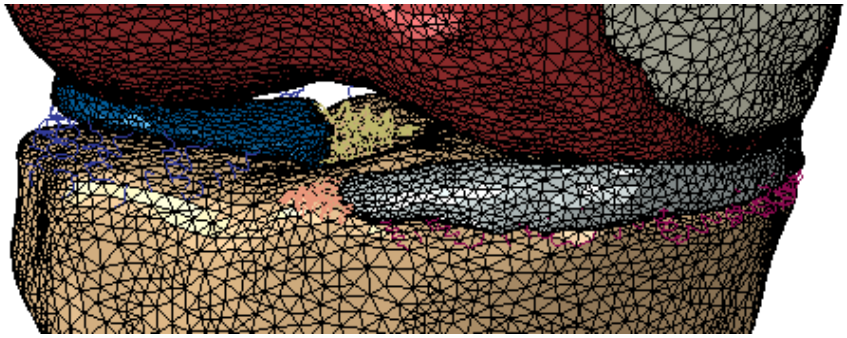

Figure 6.10 3D rendering of the full joint contact model which includes femur, femoral AC, lateral meniscus, medial meniscus and tibia reconstructed from MR image scan data. Meniscal horn attachments and MTLs are modelled using springs.

6.3.1 Sensitivity of full joint contact finite element knee models to meniscotibial ligament stiffness

Yao et al.[6] demonstrated the significance of MTL stiffness on meniscal displacements. However, no observations were made for the effects on tissue stresses.

A parametric study was carried out to investigate how the inclusion and assumptions in the mechanical properties of MTLs may affect the meniscal predictions during mechanical loading in finite element (FE) analysis. In this study, the stiffness coefficients for the MTL springs were varied from k^{i}_{MTL}=1-10kN/mm, resulting in equivalent total MTL stiffness coefficient ranging from k^{T}_{MTL}=20-200kN/mm. The range and variability in the maximum tensile stress, maximum nodal displacement in each menisci and the maximum nodal displacement at each horn was examined.

6.3.1.1 Results

Maximum principal stress, maximum nodal displacement in the lateral and medial meniscus and maximum nodal displacement in each of the four horns were compared between the models of varying MTL stiffness (Table 6.2).

Table 6.3 Parametric study results for investigating the effect of varying MTL stiffness. Meniscal stresses and nodal displacements predicted are compared for models with k_{MTL}^{T}=20-200kN/mm.

		Range		Variability (%)
Max. Principal Stress (MPa)	Medial	5.29	7.28	31.51
	Lateral	8.39	10.28	20.25
Max. nodal displacement (mm)	Medial	1.05	1.08	2.7
	Lateral	1.13	1.15	1.75
Max. nodal displacement at horn (mm)	MA	0.58	0.71	20.57
	MP	0.4	0.42	4.88
	LA	0.96	1.06	9.9
	LP	0.45	0.6	28.6

It was found that the stiffness coefficient of the MTL springs significantly affected the maximum principal stress and the horn displacements. The stress experienced in the tissue increased and the horn displacement decreased with increasing spring stiffness.

6.3.2 Meniscotibial ligaments representation using bushings –explicit model

Activities investigated for the HTO patients using motion capture and musculoskeletal modelling currently involves normal walking and stair climbing. A gait cycle is approximately 1s long and ground reaction force up to 1.5 times body weight has been measured loaded and unloaded over a period of 0.1s. Normal walking is cyclic loading of the gait cycle. Therefore, the use of the dynamic explicit method for analysing the full joint contact finite element model was explored to reduce the solving time of the model and allow future incorporation of patient specific loading conditions.

10-node quadratic tetrahedral elements were used for all parts and were assigned elements 'C3D10M' for better performance in this contact model. A quadratic tetrahedral element has 10 nodes with 4 corner nodes and 6 mid-side nodes, where each node has 3 translational DOF. The number of elements, nodes and DOF for each part of the model is given in table 6.2.

Table 6.4 Mesh details of the full joint contact finite element knee model

Tissue	Number of elements	Number of nodes	DOF
Femur (RB)	14,105	7,048	3
Femur AC	12,130	40,246	120,738
Tibia (RB/ Encastre)	11,222	3,191	0
TibiaAC	15,001	43,667	131,001
Lateral Meniscus	2,001	3,995	11,985
Medial Meniscus	1,990	4,054	12,162
Total	**56,449**	**102,201**	**275,889**

Spring elements are unstable in explicit analysis. An alternative method for modelling the MTLs using bushing was explored (Figure 6.11). The use of bushings was explored as the element allowed 6 DOF coupling, where the coupling terms could be defined dependent or independent of each other. In addition, the element allows extensions to the linear spring behaviour. Mechanical behaviours such as damping, friction and locking can be specified with reference lengths and angles, thereby allowing for more accurate descriptions of the complex mechanical behaviour of the MTLs to be implemented.

The menisci were constrained via connector elements, bushing, to the tibial plateau which represented the ligamentous constraints. The four meniscal horns (LA, LP, MA and MP) were modelled using one bushing each and the MTLs were modelled using a total of 20 bushings spread evenly along the outer inferior edge of the menisci. Stiffness in the axial and two orthogonal axes can be implemented. However, without further experimental data on the mechanical behaviour of MTLs, only stiffness along the axial axis was assigned, mimicking that of a spring element. The stiffness coefficients for the bushings were varied from 1-5.5MPa, matching values proposed by Yao et al.[6]

As with previous implementation studies, FE predictions for nodal displacement, contact pressure, and compressive stress were examined for sensible output.

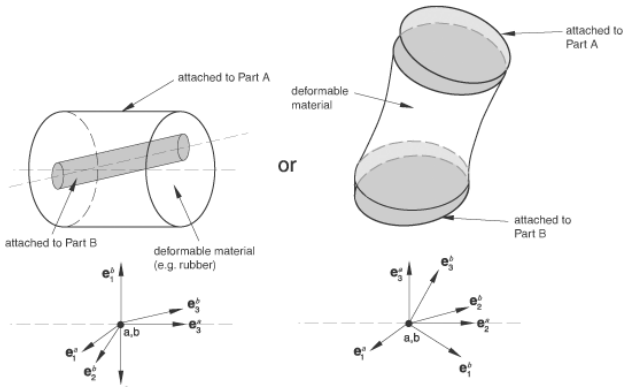

Figure 6.11 Schematic drawing of a bushing, describing the behaviour of the connector element. Used to connect two nodes, non-linear relative motion in all 6 DOFs with maximum and minimum values can be defined[5].

6.3.2.1 Results

It was found that implementation of nonlinear compressive-tensile behaviour, i.e. no compressive stiffness, was not possible in the dynamic explicit method. Collagen fibres only have structural stiffness in tension but not in compression. Under a

higher compressive load of 1800N, un-physiological displacement of the menisci was observed (Figure 6.12).

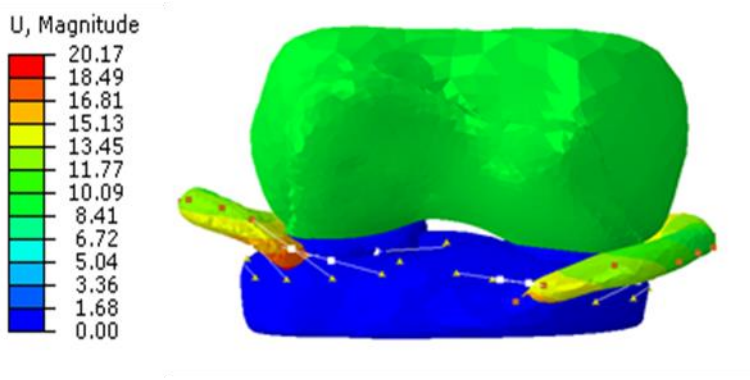

Figure 6.12 Contour plot of nodal displacement from a tibio-femoral model with menisci and MTLs modelled using bushings.

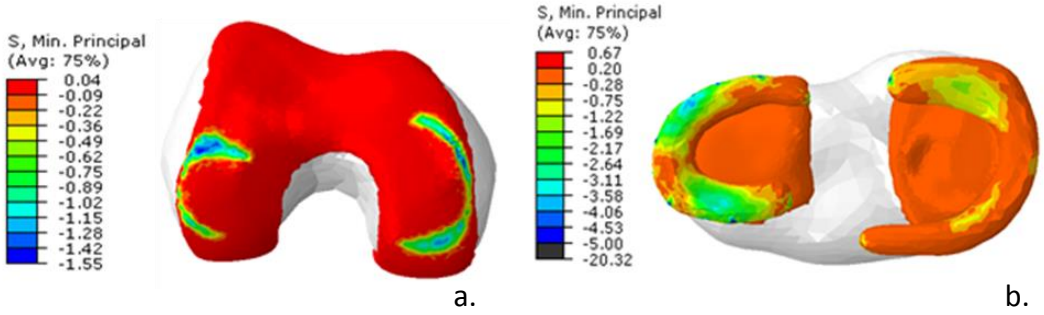

Figure 6.13 Contour plot of the minimal principal stress predicted in a tibio-femoral model with menisci a. in femoral AC b. in the menisci.

Compressive stress predicted in the lateral meniscus was higher than that in the medial meniscus (Figure 6.13). Comparable compressive stresses were predicted in the anterior and posterior part of the lateral meniscus. Whereas, it was observed that highest compressive stress in the medial meniscus was predicted in the posterior portion. For femoral AC, a compressive stress of 1.5MPa was predicted in both the lateral and medial femoral AC under an uniaxial load of 800N,. In the menisci, a maximum of 3.58MPa was predicted in the lateral menisci. The rest of the lateral meniscus experienced compressive stress of approximately 1-2MPa;

whereas, the majority of the medial meniscus experienced stresses of less than 1MPa.

6.3.3 Meniscotibial ligaments representation using a membrane

Study of the MTL microstructure revealed that the dominant orientation of collagen fibre bundles is circumferential, extending round the periphery of the menisci (Chapter 5). A method for modelling the MTLs with higher tensile stiffness in the circumferential direction is therefore required. Due to the thinness of the MTLs, it is not possible to delineate and segment the structure from medical images. With a facia like appearance, it was previously suggested that the MTLs could be modelled as a membrane[6]. Geometry and nodal conformity between the superior edge of the ligament and the menisci is essential, as well as, that between the inferior edge and the tibial plateau. To ensure conformity, the MTL geometry was generated using the femur, tibia and menisci mesh.

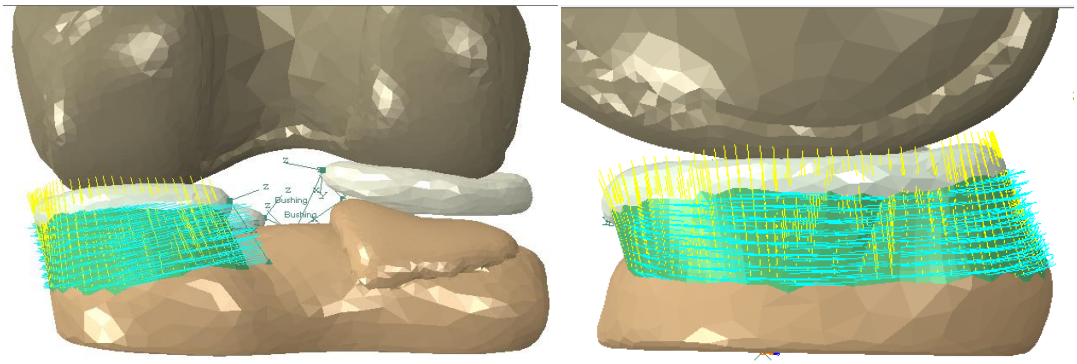

Figure 6.14 Rear and medial side view of the MTL with assigned material orientation. Yellow lines show the SI orientated axis 2, Light blue lines show the axis 1 assigned which is aligned circumferentially and conforms to the surface contour. Axis 3, orthogonal to axis 1 and 2, is assigned to aligned parallel to the surface normal of each element which is not highlighted here.

As with the menisci, the MTL was similarly assigned a material orientation using the surface geometry of the tissue with an element based method. The surface normal of each element was set to be axis 3 and axis 2 was set to align parallel to the SI surface tangent. The axis orthogonal to axis 2 and 3 is axis 1. The MTL was assigned

anisotropic material properties with E_1 = 600MPa, E_2 = 10MPa, E_3 = 5MPa, $\nu_{12} = \nu_{13}$ = 0.4, ν_{23}=0.2 and $G_{13=}G_{12}$=2 (Figure 6.14). In this model, the anisotropic membrane for MTL was only implemented on the medial side.

Type I interaction was used to define the contact between the periphery of the menisci and the superior edge of the MTL, as well as, the periphery of the tibia and the inferior edge of the menisci.

To investigate the suitability of this method for MTL representation, FE predictions for nodal displacement, contact pressure, and compressive stress were examined for sensible physiological output. The loads applied, 800N and 1800N were specifically chosen for possible comparison of model predictions against data found in literature.

6.3.3.1 Results

Under uniaxial compression loading, collapse of the MTL and its intersection with the tibia and meniscus was observed in the model without contact definition specified between the MTL and its surrounding tissues (Figure 6.15). Maximum nodal displacement in an outward lateral direction was predicted in the superior edge of the MTL where it attaches to the menisci. At the middle of the MTL shorter inward orientated tensor arrows was observed, indicating an inward collapse of the structure (Figure 6.15b).

Under uniaxial compressive loading with stress tensors showing the magnitude and direction of maximum principal stress predicted. Red indicating the maximum tensile stress predicted. Maximum principal stress predicted was noted to orientate parallel to the SI axis (Figure 6.16).

Type II interaction was defined in subsequent models between contact pairs, MTL-tibia and MTL-medial meniscus. In this model, no intersection of the MTL with surrounding tissues was observed. With the contact definition implemented,

maximum tensile stress of 16.94MPa was predicted in the anterior to middle portion of the MTL near the superior edge (Figure 6.17).

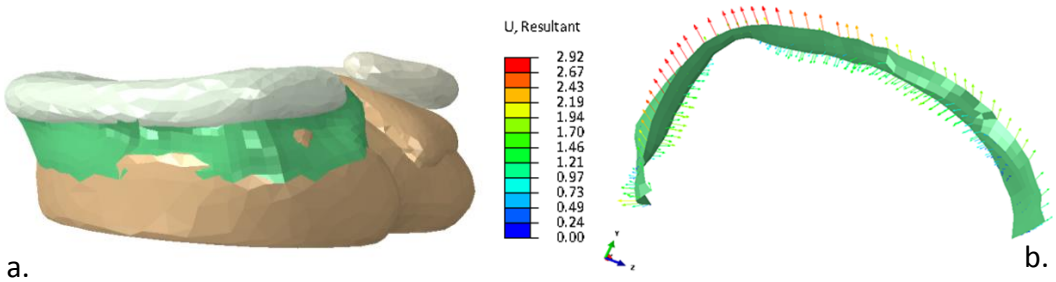

Figure 6.15 a. 3D rendering of the finite element tibio-femoral contact knee model viewed from the medial side, with menisci (white), MTL (light green), tibial AC (brown) and the tibial plateau (brown). b. Nodal displacement tensors plotted for the MTL viewed along the SI axis, i.e. in the direction of the uniaxial loading.

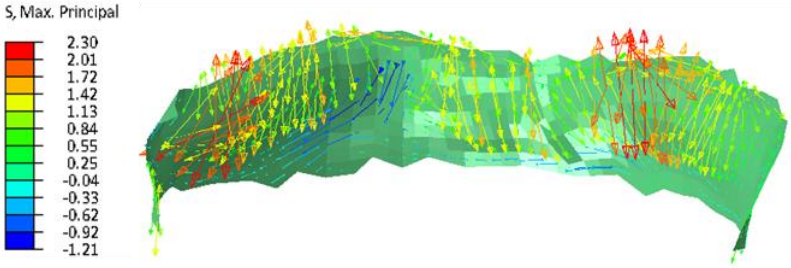

Figure 6.16 3D rendering of the MTL membrane without surface interaction between the MTL and meniscus defined.

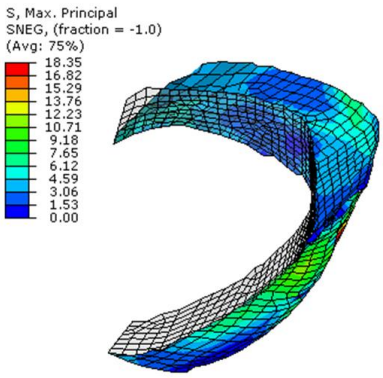

Figure 6.17 Contour plot of maximum principal stress predicted in the MTL modelled as an anisotropic membrane with contact definitions. The predicted deformed geometry of the MTL has been plotted against the original geometry, shown in the colorless mesh.

Outward nodal displacement was predicted for both menisci (Figure 6.18). Minimum displacement of 0.42mm was predicted in middle portion of the medial meniscus. It was observed that the region in the MTL with the highest predicted tensile stress corresponded with the potion of menisci with the lowest predicted nodal displacement (Figure 6.18).

Maximum principal stress was seen to align in the circumferential direction in the middle portion of the MTL and in an oblique direction in the near horn region (Figure 6.19 and 6.20). Highest tensile stress of 16.94MPa was predicted in the anterior to middle portion near the superior edge of the MTL. Tensile stress of 3.39-7.91 MPa was predicted in the near horn region.

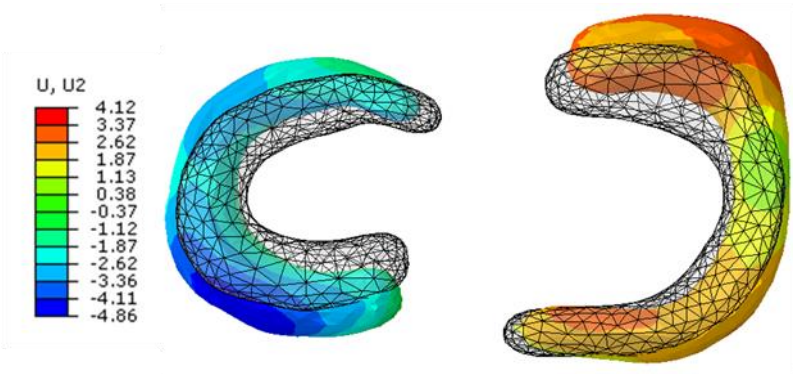

Figure 6.18 Contour plot of nodal lateral displacement for menisci in the tibio-femoral model with MTL modelled using an anisotropic membrane on the medial side.

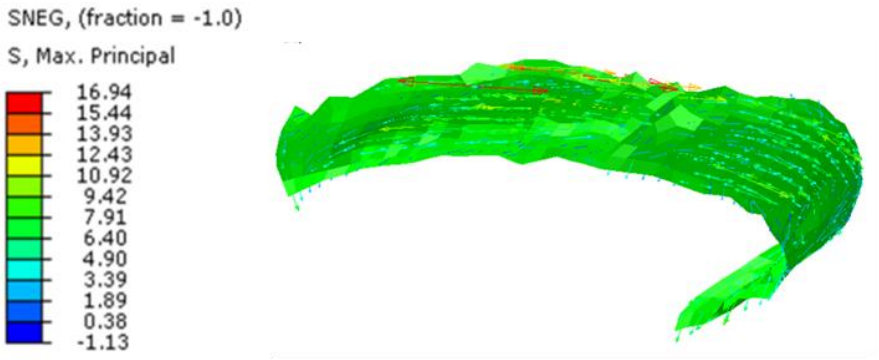

Figure 6.19 Maximum principal stress tensors plotted on the deformed MTL model. A view from an inferior anterior medial side.

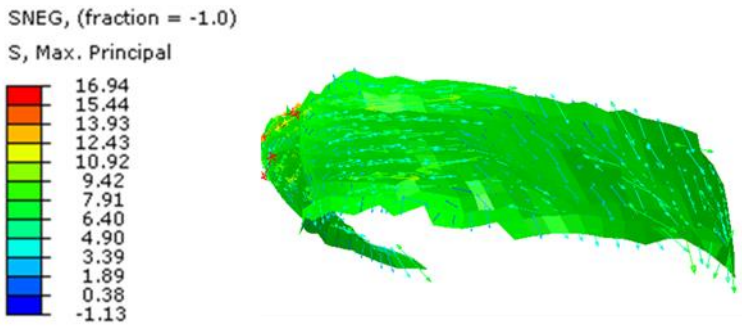

Figure 6.20 A view from the posterior of the knee showing the maximum principal stress predicted in the posterior portion of the medial MTL.

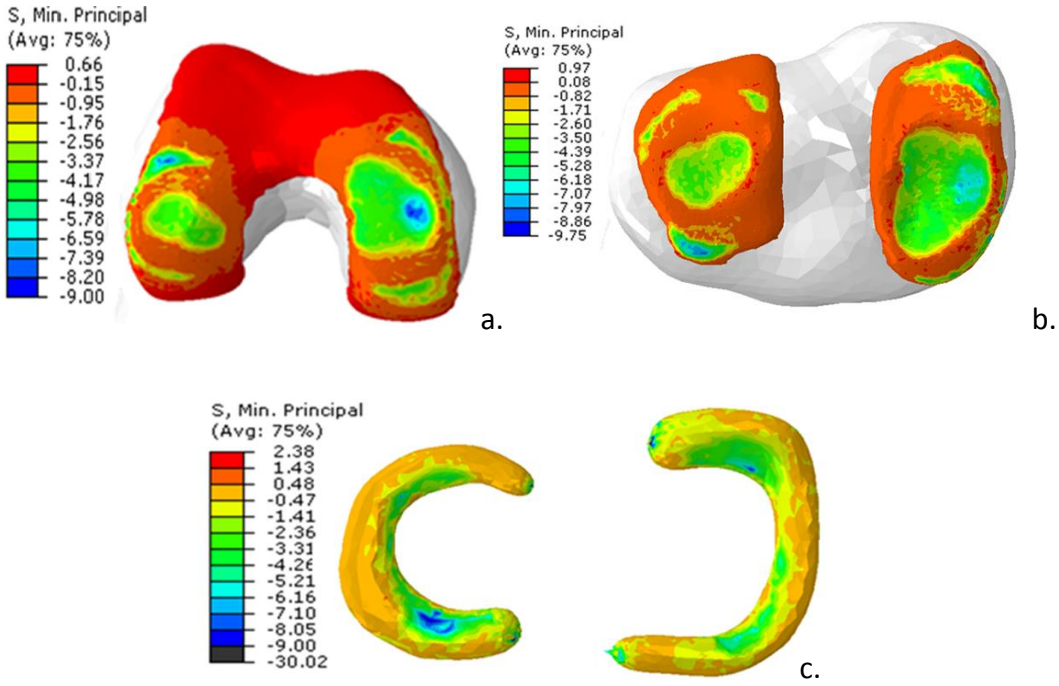

Figure 6.21 Contour plot of minimum principal stresses predicted a. in femoral AC. b. in tibial AC c. in the menisci.

In the femoral AC, a maximum of 9 MPa was predicted in the medial condyle and the anterior portion of the lateral condyle. An average of 3-4 MPa was predicted in both condyles. In the tibial AC, a maximum of 9.72MPa was predicted in the lateral condyle with an average of 3-4 MPa. For the menisci, a maximum of 9MPa was predicted and an average of 2.36-3.31 MPa in areas near contact. In the femoral AC,

tibial AC and the menisci, similar compressive stresses were predicted in both the medial and lateral compartment. In addition, maximum stresses predicted in all tissues were of similar magnitudes and were found in the same corresponding contact locations of the tissues (Figure 6.21). These locations of highest compressive stress also corresponded to the locations of highest contact pressure predicted (Figure 6.22). Maximum contact pressure of 9.2 MPa and an average contact pressure of 4-5 MPa were predicted on the lateral side of the femoral condyle. In comparison maximum contact pressure of 12.72MPa and an average of 4-6MPa was predicted in the tibial AC.

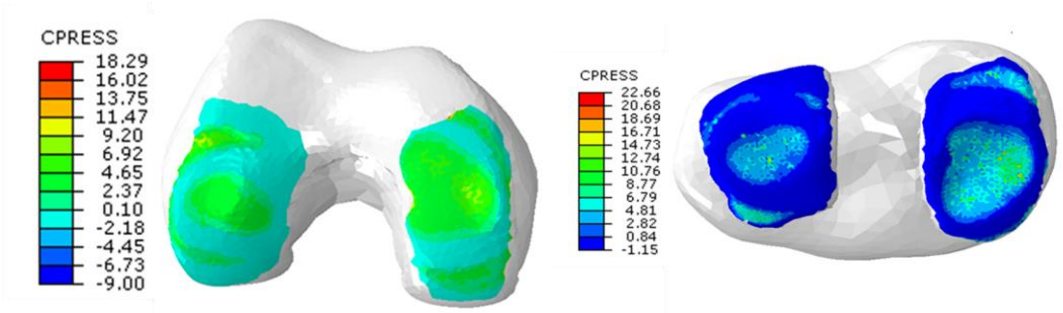

a. b.

Figure 6.22 Contour plot of contact pressure predicted. a. in the femoral AC b. in the tibial AC,

6.4 Discussion

Application of both force controlled and displacement controlled loading to the tibio-femoral knee models were explored. Due to the issues related to overlapping of tissue when directly imported from segmented MR images, the distance between the contacting surfaces becomes arbitrary. The amount of translation applied to each component in the SI axis would depend on the amount of intersection between the tissues. In the displacement controlled loading regime, iterative analysis is then required to determine the amount of displacement loading required for the tissues to establish initial contact. This initial contact reference point is determined as the point where a contact pressure is first measured and must first be determined, before displacement loading can be applied and for the correct FE results to be associated with the loading state. The same is required for

the force controlled loading regime, where a force must be applied until a contact pressure is predicted for determination of the correct initial starting position for the simulation. Although not implemented in the current models, an initial step where loading is applied to establish contact between the tissues is recommended.

Restriction of the rotational DOFs of the femur was found to significantly affect the soft tissue predictions. This includes the contact pressure, stresses and deformation of the tissue. Though predictions of contact area was observed to be less sensitive and both models predicted comparable contact areas for 0 degrees of flexion to previous studies, which was reported to be 4.7mm and 3.2 mm anterior of the midline for the medial and lateral condyle respectively[8]. In contrary to hypothesis, the model with restricted rotational DOFs more closely reflected results found in previous studies. A study using MR imaging and dual fluoroscopy observed that cartilage deformation measured in the medial compartment was higher compared to that in the lateral compartment[9]. This finding could be explained as the orientations of the tissues were segmented from a neutral resting position and therefore, the neutral position under a simple uniaxial loading condition should not be too dissimilar. As a result, it is concluded that the internal-external rotation and adduction-abduction rotation of the femur predicted in these models are extremely sensitive to surface geometry of the contacting surfaces and can lead to incorrect prediction of contact pressures, tissue stresses and deformation. Nonetheless it must also be noted that the ACL, PCL, MCL and LCL, which restrict rotational DOFs in the knee, have not been included in this model. This was due to co-ordinates incompatibility between the segmented ligaments and the current models. Incorporation of these ligaments is essential for accurate prediction of knee kinematics. Moreover, for the model to be extended for flexion-extension rotation, the inclusion of the patellofemoral ligament will be required.

Contact pressures for the medial and lateral tibiofemoral contact, measured using pressure sensitive film[10] and piezo-resistive contact pressure sensor systems[11], as

well as, values predicted by published FE models[12] [13] [14] have been summarised in Figure 6.23. However, it must be noted that despite the use of recommended quadratic tetrahedral elements, 'C3D10I' in Abaqus[15], for better contact pressure prediction performance, issues associated with the use of tetrahedral elements in contact problems persisted and therefore, further investigation is recommended for improvement of the multipart contact model.

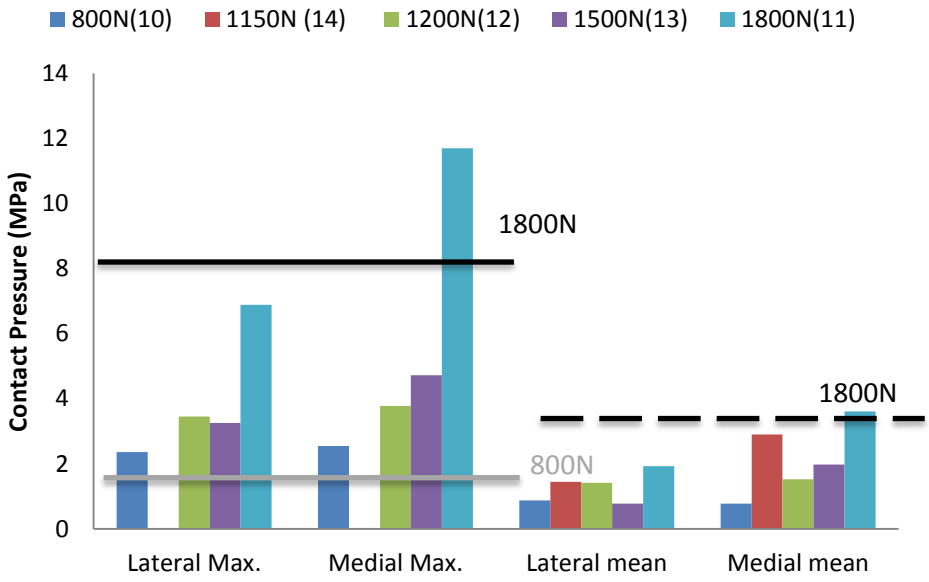

Figure 6.23 Maximum and mean contact pressures previously measured or predicted using FE for the tibiofemoral contact. For comparison, maximum and average contact pressure predicted in the explicit model with MTLs modelled as an anisotropic membrane with 1800N compressive load applied is indicated by the black solid and dashed line respectively. Maximum contact pressure predicted in the model where 800N of compressive load was applied is indicated in grey.

In the tibio-femoral model with MTL modelled using springs, a maximum compressive stress of 3.58MPa and 3.23MPa was predicted in the lateral and medial meniscus respectively. In comparison to a maximum compressive stress of around 2-3MPa predicted for a knee model under 1150N[13] and under a combination of 1150N axial and 134N of anterior tibial load[16], the maximum compressive stress predicted in this model under 800N would be expected to be

lower. However, stiffer material properties defined for the AC and menisci in this model are believed to have contributed to the higher compressive stress predicted.

Under uniaxial compression with increasing MTL stiffness, the variation in maximum principal stress and nodal displacement of the medial anterior and lateral posterior region were significantly high (i.e. >20%). This was a similar case to that found in the study of Yao et al.[3]

The use of connector elements, bushings, was explored. This was because the use of spring elements in an explicit model is unstable and can have difficulties in converging. Furthermore, bushings allow stiffness to be defined in additional DOFs and the incorporation of non-linear mechanical effect. However, it was found that no-compression stiffness could not be defined for bushings. This meant that the resistance to relative displacement of the two nodes was higher than the resistance to rotation of the element, causing excessive un-physiological lateral displacement of the menisci during compression.

In comparison, the meniscal stresses predicted in the model with MTL modelled using an anisotropic membrane were relatively more evenly distributed between the anterior and posterior portion of the medial meniscus. This suggests that the MTL found along the periphery of the menisci with fibre bundles in the circumferential direction help load distribution via a mechanism similar to that of the menisci, by restricting the lateral expansion and extrusion of the menisci. During compression loading, the menisci resist the axial force via recruitment of the circumferential fibre bundles to prevent lateral expansion of the tissue. Due to its wedge shaped cross-section, the menisci also has a tendency to extrude outwards and it is well accepted that the meniscal horns help constrain this motion. These MTLs with a ‘facia’ like structure are believed to help further reinforce the function of the meniscal horns and circumferential fiber bundles. The MTLs acts as an impeding structure, which the menisci come into contact with during lateral

expansion and extrusion. Once contact is established, the deformable structure continues to provide impedance that increases as the MTL is stretched by the meniscus. Evident in the observation that the area with lowest nodal displacement in the meniscus corresponded with the area where highest compressive stress was predicted in the MTL (Figure 6.16 and 6.17). This is further supported by comparing the stress tensors predicted in the MTLs between the model with and without contact definition specified for the meniscus-MTL contact. There was strong agreement between the maximum tensile stress tensor orientations predicted in the model with contact definition and the orientations of the fibre bundles observed in MTLs (Chapter 5).

Undoubtedly, the anterior meniscofemoral ligament (AMFL), posterior meniscofemoral ligament (PMFL), meniscofemoral ligament (MTL) and the medial meniscus attachment to the posterior portion of the superficial medial collateral ligament (sMCL) have been omitted in this model. Therefore, meniscal kinematics predicted is expected to differ from those measured in intact knee joints. However, this simplified model allowed an isolated study of the effects of MTLs on meniscal kinematics. Findings from this study have revealed the mechanism via which the MTLs contribute to meniscal constraints and knee joint stability.

A shortcoming of the study of MTLs in this project was that collecting of mechanical properties data was not possible. MTL specimens were limited and those could not be used for both mechanical testing and histology studies. It was also a concern that MTLs collected from OA patients would exhibit mechanical behaviours different to that of healthy patients. Further research into obtaining mechanical properties of the MTLs are still required.

The final aim of the patient specific FE knee model developed is for use as a clinical tool. It is therefore, important to reduce the computation time and resources required. For comparison, the bone and AC quasi-static model (model i) with

approximately 600,000 DOF solved using 16 parallel processors, required 25,387 seconds (approximately 7 hours) of CPU time and approximately 9,351 seconds of wall clock time (approximately 2.5 hours).

By removal of the deformation tibia, the DOFs were reduced to 100,000 in the bone, AC and meniscus quasi-static model (model ii). Solved on a single CPU, a total of 27,942 seconds (approximately 7.8 Hours) CPU time was required. Incorporation of the mobile deformable menisci increased the complexity of the full joint contact model was expected to require significant amount of computation power. However, comparison between model i and model ii where similar CPU time were required, showed that modelling the tibia as a rigid body can significantly reduce computational time. Appropriate use of rigid bodies where possible is therefore, recommended.

The dynamic explicit finite element model had 276,000 DOFs (Table 2.1). Though double the DOFs in model ii, this dynamic explicit model was solved in 900 seconds (approximately 15 minutes) with a single CPU. Dynamic explicit FE models are known for their ability to reduce computational time required. However, careful selection of time steps is required as this may affect the accuracy of the results predicted. No such convergence study on time step size required was carried out in this project. The convergence study may reveal that the current time step is not sufficient and that a smaller time step is required, which could increase the computational time required. It is therefore, recommended that such further investigation be carried out prior to concluding between the use of the quasi-static and the explicit formula.

6.5 References

[1] T.L. Haut Donahue, M.L. Hull, M.M. Rashid and C.R. Jacobs, 'A finite element model of the human knee joint for the study of tibio-femoral contact', Journal of Biomechanical Engineering, 124:273-280

[2] Abaqus v.6.12 Documentation, Abaqus Analysis User's Manual, SIMULIA

[3] C.M. Müller-Karger, C. González, M.H. Aliabadi and M. Cerrolaza, 'Three dimensional BEM and FEM stress analysis of the human tibia under pathological conditions', Computer Modelling in Engineering & Science, 2(1):1-13, 2001

[4] L. Blankevoort, R. Huiskes and A. de Lange, 'The envelope of passive knee join motion', Journal of Biomechanics, 21:9, 705-720, 1988

[5] P. Beillas, G. Papaioannou, S. Tashman and K.H. Yang, 'A new method to investigate in vivo knee behavior using a finite element model of the lower limb', Journal of Biomechanics, 37:1019-1030, 2004

[6] J. Yao, J. Snibbe, M. Maloney and A. Lerner, 'Stresses and strains in the medial meniscus of an ACL deficient knee under anterior loading: a finite element analysis with image-based experimental validation', Journal of Biomechanical Engineering, 128:135-141, 2006

[7] T.L. Haut Donahue, M.L. Hull, M.M. Rashid, C.R. Jacobs, 'The sensitivity of tibiofemoral contact pressure to the size and shape of the lateral and medial meniscus', Journal of Orthopaedic Research, 22:807-814, 2004

[8] L.E. DeFrate, H. Sun, T.J. Gill, H.E. Rubash and G. Li, 'In vivo tibiofemoral contact analysis using 3D MRI-based knee models', Journal of Biomechanics, 37:1499-1504, 2004

[9] J.T. Bingham, R. Papannagari, S.K. van de Velde, C. Gross, T.J. Gill, D.T. Felson and H.E. Rubash and G. Li, 'In vivo cartilage contact deformation in the healthy human tibiofemoral joint', Rheumatology, 47:1622-1627, 2008

[10] T.L. Haut Donahue, M.L. Hull, M.M. Rashid and C.R. Jacobs, 'How the stiffness of meniscal attachments and meniscal material properties affect tibio-femoral contact pressure computed using a validated finite element model of the human knee joint', Journal of Biomechanics, 36:19-34, 2003

[11] S-Y. Poh, K-S. A. Yew, P-L. K. Wong, S-B. J. Koh, S-L. Chia, S. Fook-Chong, T-S. Howe, 'Role of the anterior intermeniscal ligament in tibiofemoral contact mechanics during axial loading', The Knee, 2011, doi:10.1016/j.knee.2010.12.008

[12] C. Bratianu, P. Rinderu and L. Gruionu, 'A 3D finite element model of a knee for joint contact stress analysis during sport activities', Key Engineering Materials, 261-263:513-518, 2004

[13] G. Papaioannou, G. Nianios, C. Mitrogiannis, D. Fyhrie, S. Trashman and K.H. Yang, 'Patient-specific knee joint finite element model validation with high-accuracy kinematics from biplane dynamic Roentgen stereogrammetric analysis', Journal of Biomechanics, 41:2633-2638, 2008

[14] E. Peña, B. Calvo, M.A. Martínez, D. Palanca and M. Doblaré, 'Finite element analysis of the effect of meniscal tears and meniscectomies on human knee biomechanics', Clinical Biomechanics, 20:498-507, 2005

[15] A. Erdemir, T.M. Guess, J. Halloran, S.C. Tadepalli and T.M. Morrison, 'Considerations for reporting finite element analysis studies in biomechanics', Journal of Biomechanics, 45:625-633, 2012

[16] E. Peña, B. Calvo, M.A. Martínez and M. Doblaré, 'A three-dimensional finite element analysis of the combined behaviour of ligaments and menisci in the healthy human knee joint', Journal of Biomechanics, 39: 1686-1701, 2006

Chapter 7 Conclusions and Future Work

High Tibial Osteotomy is an alternative surgical procedure for early stage OA patients. During the procedure, the mechanical axis of the knee is re-aligned for better distribution of loads across the knee joint. The ARUKBBC has identified the HTO patient cohort as a possible human model for the study of the relationship between changes in mechanical loading and biology of AC. The aim of this project was to initiate the development of a validated patient specific finite element knee model for relating mechanical changes measured using gait analysis and biological changes quantified using gene expression studies. Issues relating to accurate surface geometry and meniscal constraints were investigated for improvement of stress and strain predictions in current full joint contact finite element knee models.

During mechanical loading of the knee, the load is shared between the various tissue structures and loading experienced by AC will depend on the kinematics of the knee and mechanical behaviour of the other tissues. Both the ECM and the interstitial fluid support load carrying in AC. Introducing further complexity to the determination of loading conditions experienced by the chondrocytes is the presence of a pericellular matrix found within the ECM which regulates the transfer of mechanical loads from the ECM to the pericellular matrix. The pericullular matrix is known to have a lower stiffness compared to the ECM. Therefore, it is believed that the pericellular matrix transfers mechanical loads to the chondrocytes in the form of strains. Depending on the mechanical stimulus experienced, such as, shear, compression, tensile or hydrostatic, catabolic or anabolic processes are triggered in the chondrocytes. It is therefore, of great interest to be able to predict accurate

stress and strain magnitudes and distributions experienced in the ECM during mechanical loading of the joint.

Inhomogeneity of stress and strains experienced in the tissue during mechanical loading is introduced due to the depth dependent microstructure. Extensive research has been carried out to develop constitutive models which captured this behaviour. However, it was hypothesised that undulations on the surface of AC would cause further inhomogeneity of stresses and strains experienced in the tissue. An in-vitro study was carried out on excised human explants to explore the effects of natural surface undulations on the stress and strain distribution predicted in AC during mechanical loading. It was found that surface curvatures have a significant effect on the distribution of stresses and strains predicted inside the tissue. Furthermore, it was observed that the magnitudes of stresses and strains experienced were different to that expected. Using DIC and an image registration technique, explant specific finite element models were generated. Comparison of a explant specific and an equivalent FE model where AC was modelled as a flat surface cylinder, demonstrated that under the same uniaxial forced controlled compression loading, platen displacement (i.e. tissue strain) and the maximum stress experienced was significantly underestimated. This is due to the larger contact area of the perfectly conforming contact surfaces in the flat surface case.

The explant specific FE model was also used in reverse, for inverse FE to determine AC stiffness by optimisation of predicted platen displacement against experimental data. Stiffness of the AC explants was calculated based on the platen displacement and force applied assuming a flat surface cylindrical geometry. The calculated stiffness was significantly lower than that determined using inverse FE on the explant specific geometries.

In the gene expression study, explants were subjected to force loading equivalent to either 10% or 15% strain, assigned randomly. Explant specific models were

generated for each implant and analysed with their respectively loading conditions applied. No correlation was found between the explants which were assigned a higher strain loading regime and those that were predicted to have experienced larger stresses. Additionally, it was found that surface undulations induced tri-axial stresses of significant magnitudes, which were not present in the flat surface cylinders.

As discussed in Chapter 3 of this thesis, cutting of the AC surface to eliminate this error is undesirable as it affects the biological and the mechanical behaviour of the tissue. Thus, findings from this study have a great impact on both mechanical and mechanobiology studies carried out on AC.

An initial aim of this study was to explore the possibility of correlating FE predictions and gene expression results. Although gene expression study results for the explants used in this study was not available, a protocol compatible with gene expression study requirements has been established for the generation of explant specific finite element model for future studies.

The second aim for investigation was the importance of AC geometry on the prediction of stresses and strains. Accuracy of the AC geometry in full joint contact FE models is highly dependent on the MR image resolution, segmentation and meshing process, as demonstrated in Chapter 4. This in-vitro study has highlighted the importance of accurate surface geometry of AC on the full joint contact FE model predictions of stresses and strains experienced inside the tissue.

Two sets of patient specific MR imaging data of the knee was examined for delineation and segmentation of the various tissue structures in the knee. It was found that an in plane resolution of 1mm x 1mm was insufficient for accurate delineation of AC which is approximated to be 2mm thick on average. A minimum in plane resolution of 0.37mm x 0.37mm should be used. MR image data produced using a FIESTA-C scan sequence, instead of the GRE scan sequence on the 3T MR

scanner manufactured by General Electric was noted to have a higher signal to noise ratio which allowed better delineation of the soft tissue boundaries for segmentation. In additional to the bones (femur, tibia, fibula and patella) and their respective AC, the higher resolution MR images also allowed the delineation and segmentation of other structures in the knee, which included the menisci, patella ligament, ACL and PCL.

The use of three different assistive tools for manual segmentation available in ScanIP, Simpleware Ltd., to reduce operator subjectivity of the segmented volumes and operator effort was examined specifically for application to MR imaging scan data of the knee. The three algorithms explored were floodfill, threshold paint and confidence region growing. Segmentation with the assistance of threshold paint and the multi-slice selector tool was found to be the most effective. The use of floodfill requires tissue boundaries to be clearly defined first by manual segmentation on every slice of the MR imagining scan data. Although useful for tissues with a large volume to surface area ratio, such as the femur and tibia, no significant reduction in operator effort was seen for the ligaments, AC and menisci. Furthermore, voxels selected for the tissue boundaries were highly subjective to the operator's opinion.

In comparison to the floodfill and threshold paint tools, the confidence region growing algorithm, if applicable, would allow the greatest reduction in both operator effort and segmented volume variability. However, as a result of inhomogeneous tissue material properties, greyscale value range for each tissue was found to be large, spanning almost half of the full 0-255 scale. Along with the large number of tissue structures in the knee, their complex arrangement and a number of tissues with similar material properties neighbour each other, application of the confidence region growing algorithm was found to be difficult.

Use of the hybrid marching cube-voxel based with improved surface mesh meshing algorithm available in ScanIP (+FE module), Simpleware Ltd. for creating meshes for tissues of the knee was explored. Due to the voxel based nature of the meshing algorithm, data resampling had to be applied to the MR image data to obtain meshes of a suitable mesh density and number of elements. Meshing of the femur and femoral AC based on the original MR image resolution of 0.37mm x 0.37mm resulted in a total of 2.5 million elements. In a previous study, mesh convergence for full joint contact FE models, was reported for meshes with average element size of 1 mm x 1 mm[1]. However, it must be noted that hexagonal elements were used and a uniform mesh size was used for all tissues. The current finite element full joint contact model was meshed using MR imaging data resampled 0.9mm x 0.9mm x 0.9mm with tetrahedral elements. Moreover, mesh refinement was specified for the contact areas to increase the mesh density and improve FE predictions.

The most significant error introduced in the geometry representation of AC and menisci was due to the data resampling process. As demonstrated in Chapter 3 of this thesis and by previous authors, small variations in AC and meniscal geometry has a substantial effect on the FE predictions[2]. Therefore, the use of meshing algorithms that do not require resampling of the data is suggested for future investigations.

The fourth aim of this thesis was first examined using an anatomy study on excised human tibial plateaus from TKR surgery. Of the five samples collected, the presence of MTLs was found in four. MTLs were observed along the anterior, middle and posterior periphery of both the medial and lateral menisci. None of the MTLs in the samples collected extended round the entire periphery of either the lateral or medial meniscus. However, it must be noted that the samples were collected from TKR patients with OA. Damage to the MTLs could have occurred before or during the surgery. It is therefore, not possible to determine whether MTLs in a healthy joint does extend the entire periphery of both menisci.

The MTL specimens collected were fixed, sliced and stained using Picrosirius red to enhance the birefringence of the collage fibres. With the use of cross polarise light microscopy, the CF organisation in MTLs was determined. The orientation of CFs was found to be arranged predominately in the circumferential direction around the menisci. This is perpendicular to the orientation of CFs previously thought. In the regions near the meniscal horns, the CFs were found to be orientated obliquely at an angle parallel to the orientation of the CFs in the meniscal horns. Examination of the microscopy images has further revealed that the fibre bundles were of an approximate width of 6-8µm, along with the highly orientated parallel arrangement of the fibres forming fibre bundles, it was concluded that collagen found in MTLs are of Type I collagen.

Using a protocol established from the study exploring the delineation, segmentation and meshing of tissues from patient specific MR imaging scan data detailed in Chapter 4 for this thesis, a quasi-static and a dynamic explicit finite element model of the knee was created. Boundary conditions and material properties applied were taken from previous full joint contact FE knee models. The MTLs were also modelled following the method found in the literature[3], using springs aligned in the SI axis. Using this finite element knee model, a study examining the effect of variation in MTL stiffness on soft tissue predictions was carried out. It was found that MTL stiffness variation significantly affected the meniscal deformation and displacement predictions in the full joint contact model, agreeing with previous research[3]. Furthermore, stresses experienced within the menisci were also found to be highly dependent on the MTL stiffness.

An alternative method for modelling the MTLs using bushings was explored. Bushings allow restriction on the relative displacement in all 6 DOFs between two nodes to be defined. It is therefore, advantageous over the use of springs which only constraint relative motion between two nodes along their line of axis. However, it was found that a no compression condition could not be implemented

for the bushings and as a result, produced non-physiological displacements of the menisci under higher uniaxial compression loading of 1800N.

Findings from the study of the MTL microstructure detailed in Chapter 5 of this thesis proved that the previous method of modelling MTLs in full joint contact finite element models is invalid. The use of an anisotropic membrane for modelling MTLs was investigated. Anisotropic material properties were defined using an element based local coordinate system. This allowed an accurate description of the three axes despite irregular membrane geometry. A higher Young's modulus was assigned for the circumferential axis reflecting the Type I collagen fibre bundles observed in Chapter 5 of this thesis.

A 'tie' interaction contact definition was assigned to model the meniscus-MTL and tibia-MTL contact representing the CFs found aligned in the SI axis in the superior and inferior region of the MTLs. Contact definitions between the meniscus and MTL are important for the correct prediction of MTL behaviour. Without the contact definition, the stress tensors predicted for the MTL were found to be orientated in the SI axis. Whilst with the contact definition implement, the MTL was observed to help constrain lateral deformation and displacement of the meniscus and stress tensors predicted were orientated in the circumferential direction, agreeing with the orientation of CFs found in the MTLs.

Meniscal stresses predicted in the model with MTL represented using an anisotropic membrane were comparatively more evenly distributed throughout the tissue, than that predicted in the model with MTL represented using springs. It is therefore believed that the functional role of MTLs in the knee is to help reinforce the function of the meniscal horns and circumferential fibres in meniscus. Thus, it is concluded that the MTLs play a significant role in knee kinematics and their inclusion in full joint contact FE models are paramount.

In conclusion, for accurate prediction of stress and strains in the ECM during mechanical loading, an accurate representation of the tissue geometries is important. It is inevitable that the use of voxel based meshing algorithms introduces errors in the segmented tissue volumes and therefore, the use of contour based meshing algorithms are suggested for future work. Mechanical properties of the MTLs also have a profound effect on FE predictions in full joint contact models and require further investigation. This work has provided an insight into the microstructure of the MTLs and proposed suitable method of inclusion in full joint contact models. The mechanical properties of MTLs can either be determined by optimisation of the full joint contact model prediction against experimental data or by direction mechanical testing, if possible.

7.1 Future Work

I. Due to the absence of the gene expression study results, the ability to correlate gene expression study results and FE predictions could not be established. Thus, a further gene expression study with explant specific FE modelling must be carried out. To improve the stress and strain predictions, biphasic, depth dependent and anisotropic constitutive models for AC are recommended. Coupling with a sub-model to simulate the ECM, pericellular and intracellular mechanical interaction could also be beneficial.

II. Significant error was introduced in the segmented volume of the menisci and AC during data resampling, as the meshing algorithms available in ScanIP (+FE module), Simpleware Ltd., are fundamentally voxel based. The use of a meshing algorithm that does not require resampling of the MR imaging data, such as a contour based meshing algorithm should be investigated.

III. Segmentation accuracy and the significance of operator variability using the protocol established is unknown. A study should be carried out on a cadaver to compare the segmented tissue volumes and the actual tissue geometries

measured using methods such as coordinate measuring machines. Further study comparing the variability in segmented tissue volumes between different operators will also confirm the robustness of the protocol established. The effect of the errors in geometry and the segmented volumes on full joint contact FE model results should also be investigated.

IV. The possibility of an automated segmentation algorithm could be explored using a combination of (1) random walks segmentation algorithm, (2) probabilistic data for the size, geometry and location of the tissue and (3) machine learning techniques, specifically those for pattern recognition.

V. Mechanical testing to determine the mechanical behaviour of the MTLs are required. Mechanical testing should preferably be done on samples collected from healthy knee joints to eliminate possibility of altered material properties due to disease.

VI. Incorporation of the patella, patella ligament, collateral and cruciate ligaments into the full joint contact finite element model are required for true prediction of knee kinematics behaviour under complex triaxial loading conditions during gait calculated from musculoskeletal modelling.

VII. Coupling of the finite element knee model with patient specific geometries with the musculoskeletal model which calculates patient specific loading conditions is required for a fully patient specific finite element model.

VIII. The issue with patient specific tissue material properties should also be addressed. Measurement of the material properties of the patients using mechanical testing is not possible. Thus, the variability of soft tissue material properties in early OA patients should first be established. A parametric study could then reveal the significance of the variation in the FE model results. If the variation in material properties causes a significant difference in FE predictions, a non-invasive method for obtaining patient specific tissue material properties will be necessary.

IX. In the future, with an established correlation between the full joint contact patient specific finite element knee model and gene expression results and an established understanding of the relationship between gene expression and tissue matrix turn over, the resulting altered mechanical properties of the tissues can perhaps be expressed mathematically and incorporated into the FE model. This will allow the inclusion of mechanobiology effects in the FE predictions.

---

[1] G. Papaioannou, G. Nianios, C. Mitrogiannis, D. Fyhrie, S. Tashman and K.H. Yang, 'Patient-specific knee joint finite element model validation with high-accuracy kinematics from biplane dynamic Roentgen stereogrammetric analysis', Journal of Biomechanics, 41:2633-2638, 2008

[2] T.L Haut Donahue, M.L. Hull, M.M. Rashid and C.R. Jacobs, 'The sensitivity of tibiofemoral contact pressure to the size and shape of the lateral and medial meniscus', Journal of Orthopaedic Research, 22: 807-814, 2004

[3] J. Yao, J. Snibbe, M. Maloney and A.L. Lerner, 'Stresses and strains in the medial meniscus of an ACL deficient knee under anterior loading: a finite element analysis with image-based experimental validation', Journal of Biomechanical Engineering, 128: 135-141, 2006